An Advanced Modeling Framework with Well-Designed Experiments to Unveil Molten Pool Dynamics and Particle Spattering Behavior

Shaocong Qin

Department of Mechanical, Manufacturing and Biomedical Engineering

Trinity College Dublin, the University of Dublin

Feb 2026

A thesis submitted to the Trinity College Dublin, the University of Dublin

in partial fullfillment of the requirements for the degree of

Doctor of Philosophy

Supervisor: Dr. Shuo Yin

Declaration

I declare that this thesis is the result of my independent work, conducted after my registration at Trinity College Dublin, the University of Dublin, for the postgraduate programme leading to the degree of Doctor of Philosophy in the Department of Mechanical, Manufacturing, and Biomechanical Engineering. I confirm that it has not been included in any prior thesis or dissertation submitted to this or any other institution for any degree, diploma, or equivalent qualification.

I agree to deposit this thesis in the University's open access institutional repository or allow the library to do so on my behalf, subject to Irish Copyright Legislation and Trinity College Library conditions of use and acknowledgement.

Shaocong Qin

Acknowledgements

As time quietly flows by, my PhD journey in Ireland is now approaching its end. The past four years have been an incredibly enriching experience—academically, personally, and culturally. I have been fortunate to witness the breathtaking landscapes of Ireland, experience its warm and genuine culture, and, most importantly, receive the care, encouragement, and support of so many mentors, colleagues, and friends. At this moment of reflection and gratitude, I would like to express my heartfelt thanks to all those who have supported and encouraged me along the way.

First and foremost, I would like to express my deepest appreciation to my supervisor, Dr. Shuo Yin, for his patient guidance and unwavering support over the past four years. His insightful advice, constructive feedback, and constant encouragement have helped me navigate the many challenges of research. He also offered me valuable opportunities to attend international conferences, which broadened my academic horizons and enriched my research experience. Also, I am equally grateful to Dr. Shenghui Lei, whose rigorous academic standards and approachable demeanor left a lasting impression on me. I sincerely appreciate his tireless efforts in reviewing my manuscripts and offering guidance in the field of convective heat transfer. The dedicated mentorship of both Dr. Yin and Dr. Lei has laid a solid foundation for my academic writing and research capabilities, and will continue to guide me on my future research path.

I would also like to thank Dr. Rocco Lupoi for his support as co-leader of the STAM research group. My sincere thanks go to Alex and the workshop staff for their technical assistance in the fabrication of my experimental setups. I am also grateful to Mina and the team at the Advanced Microscopy Laboratory (AML) for their generous support during my experiments. A special thanks to Dr. Wenyou Zhang, whose valuable advice and mentorship have greatly benefited my research. I would also like to express my gratitude to Xihang Yu and his colleagues at Yangzhou University in China for their generous support and collaboration in completing the preheating experiments for the LPBF process, which significantly enriched the technical depth of my work. I would also like to extend my appreciation to my fellow research group members for their time, collaboration, and willingness to share their experiences and perspectives. My gratitude also goes to all the staff at Trinity College Dublin who have helped me in various ways throughout this long journey.

I am sincerely thankful for the financial and academic support provided by the China Scholarship Council (CSC) - Trinity College Dublin Joint Scholarship Programme (202008440334). This generous funding made it possible for me to pursue my doctoral studies in Ireland. I am also grateful to Trinity College Dublin for offering such an inspiring academic environment and a campus of remarkable beauty. The years I spent at Trinity will remain one of the most cherished and transformative periods of my life.

Last but not least, I am deeply thankful to my family and friends for their unconditional love and constant encouragement. Their steadfast support has been the backbone of my perseverance through the many challenges of my PhD, allowing me to complete this chapter of my academic life.

As this journey comes to an end, I carry with me not only academic knowledge but also invaluable life lessons and personal growth. The experiences and resilience I have gained during my PhD will serve as a source of strength in the face of future challenges. With a heart full of gratitude, I look forward to contributing, however modestly, to the advancement of knowledge and the betterment of society.

Abstract

Laser powder bed fusion (LPBF) has emerged as a pivotal metal additive manufacturing technology, enabling near-net-shape fabrication with superior design flexibility and material efficiency. However, the process remains challenged by complex defect formation mechanisms—most notably spatter generation and melt pool instabilities—which hinder component quality, dimensional accuracy, and process repeatability. This work presents a comprehensive and multi-physics investigation that bridges powder-bed behavior, melt pool thermofluidics, and vapor-particle interactions to elucidate the underlying physics of defect evolution in LPBF.

At the powder scale, a validated Discrete Element Method (DEM) model successfully captures powder spreading uniformity and surface roughness, serving as the foundation for simulating layer quality and initial bed conditions. At the melt pool scale, a high-fidelity CFD model incorporating heat conduction, Marangoni convection, vapor recoil pressure, surface tension effects, and phase change dynamics is developed. The results reveal that the rate of interfacial heat extraction at the solid–liquid boundary and localized thermal inhomogeneities—not total energy input—are the dominant parameter governing melt pool morphology and defect initiation. At high scan speeds, increased local thermal extraction steepens temperature gradients, driving hump and balling via thermally-induced surface retraction. Conversely, at low scanning speeds, prolonged laser exposure tends to induce frequent thermal accumulation events. Although the solid–liquid interfacial area increases—leading to greater total heat dissipation—the net heat accumulation within the melt pool can sometimes become negative. Under such conditions, vapor bubbles generated within the keyhole are more likely to be trapped by the solidification front, significantly increasing the risk of porosity formation.

Furthermore, a novel heat transfer perspective redefines the origin of these defects: spatial thermal inhomogeneity along the melt pool generates localized capillary instabilities, leading to melt pool break-up. The role of preheating is also critically reassessed; while it improves thermal uniformity and suppresses surface instabilities at high scan speeds, it aggravates porosity at low speeds due to reduced Marangoni convection and enhanced vapor entrapment.

In-depth analysis of powder spattering dynamics reveals a two-stage detachment mechanism, where particles first undergo micro-scale rolling or sliding driven by shear and vapor forces, then overcome interfacial friction and adhesion to become airborne. High-speed imaging, SEM observations, and CFD modeling collectively show that vapor-induced drag and turbulence dominate particle ejection, with rearward angular shift and clustering behavior becoming pronounced at elevated scan speeds. The final fate of particles-reincorporation or escape-is strongly influenced by melt pool wettability and plume oscillations. A modified spatter prediction model incorporating melt pool capillarity and vapor-plume coupling substantially improves agreement with experimental trends.

This study offers a unified framework for understanding and predicting defect evolution in LPBF by tightly integrating powder-scale mechanics, melt pool thermodynamics, and gas-particle coupling. The insights provide a scientific basis for defect suppression strategies, real-time control, and digital twin development in next-generation metal AM platforms.

Keywords: Laser powder bed fusion (LPBF), DEM, CFD, melt pool dynamics, heat transfer, powder spattering dynamics, wettability.

List of Publication

Journal Articles

1. Yuan, W., Chen, H., Ruan, S., Lupoi, R., **Qin, S.**, Guo, E., ... & Yin, S. (2025). Oscillatory nature in melt-gas-powder interactions during laser powder bed fusion process revealed by CFD-DEM coupled modelling. ***Virtual and Physical Prototyping***, *20*(1), e2446619.
(JCR **Q1**, IF **10.2**)

Conference Presentations

1. **Shaocong Qin,** Wenyou Zhang, Shenghui Lei, Shuo Yin*. Experimental and Numerical Study of the Spattering Dynamic Mechanisms in Laser powder bed fusion. In: ***International Thermal Spray Conference*** (ITSC), 2024, Milan, Italy.

Manuscripts ready for submission

1. **Shaocong Qin.** Missing the Heat? Unveiling the Role of Dynamic Thermal Disequilibrium in LPBF Melt Pool Stability. (Ready to submit) – **Chapter 5**

2. **Shaocong Qin.** Dynamics of vapor plume evolution and spatter formation during laser powder bed fusion additive manufacturing. (Ready to submit) – **Chapter 6**

Contents

List of Figures

List of Tables

Chapter 1. Introduction

In recent years, traditional subtractive manufacturing methods have become increasingly difficult to meet the growing demands of equipment manufacturing for both geometric complexity and mechanical performance of components. With the continuous advancement of modern manufacturing technologies, additive manufacturing (AM) has emerged as a transformative approach to product design and development across various industrial sectors. AM is a technology that achieves near-net shaping of components through layer-by-layer deposition, using powders, metal wires, or liquid materials as raw materials based on discrete-stacking principles[1]. As illustrated in Fig. 1.1, AM processes differ fundamentally from conventional manufacturing (CM) processes in several aspects, most notably in generating significantly less material waste. The layer-by-layer nature of AM enables the combination of dissimilar materials, the construction of complex internal features, the integration of biomimetic topologies, and the embedding of sensors and other functional devices within components[2].

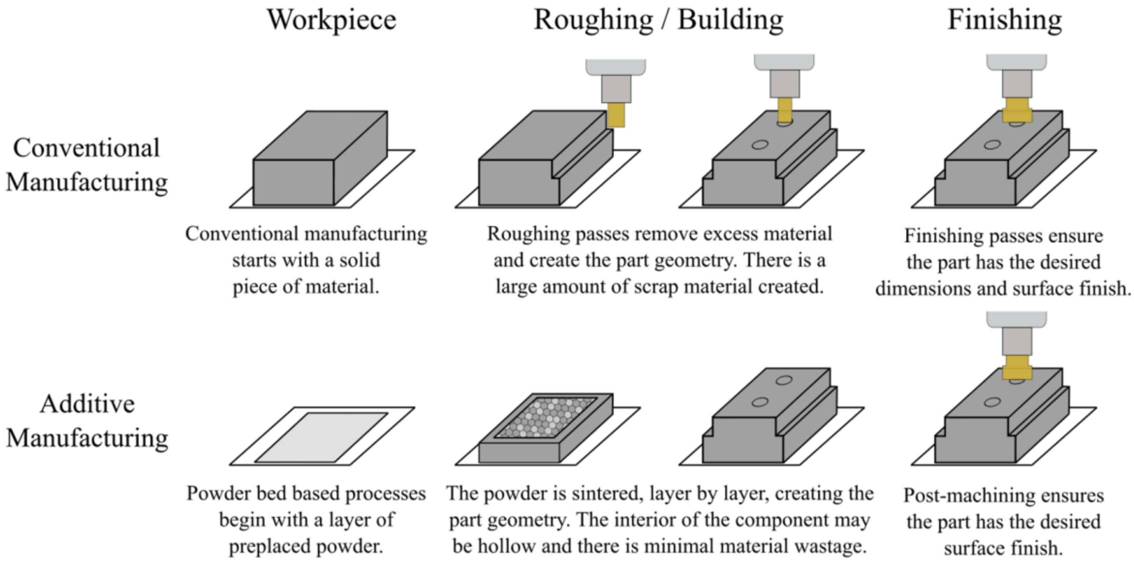

Fig. 1.1. Comparison with the conventional and additive manufacturing processes[2].

According to ASTM F2792 and F42, AM processes are commonly categorized into seven main groups as shown in Table 1.1: powder bed fusion (PBF), direct energy deposition (DED), sheet lamination (SL) (by ultrasonic), binder jetting, material jetting, material extrusion, and vat photopolymerization[2].

Table 1.1 List of AM processes[2]

Process category	AM process
Powder bed fusion (PBF)	Laser powder bed fusion (LPBF)
	Direct metal laser sintering (DMLS)
	Selective laser sintering (SLS)
	Electron beam melting (EBM)
Direct energy deposition (DED)	Laser-engineered net shaping (LENS)
	Direct metal deposition (DMD)
	Laser metal deposition (LMD)
	Laser free-form fabrication (LF3)
	Electron beam freeform fabrication (EBFFF)[a)]
	Shaped metal deposition (SMD)[a)]
	Wire and arc additive manufacturing (WAAM)[a)]
Sheet lamination (SL)	Laminated object manufacturing
	Ultrasonic additive manufacturing
Jetting	Material jetting
	Binder jetting
Arc-based AM	Gas tungsten arc
	Gas metal arc
	Plasma arc
Material extrusion	Fused deposition modeling (FDM)
Vat photopolymerization	Stereolithography (SLA)

[a)] Denotes a wire-fed DED process.

Among these, laser powder bed fusion (LPBF) has been widely recognized as one of the most promising AM technologies, as it balances high shaping precision with excellent mechanical performance. LPBF has been successfully applied in various industries, including aerospace, automotive, biomedical, and others[3]. The fundamental principle of LPBF involves a focused laser beam, guided by 3D CAD data, selectively scanning a thin layer of metal powder spread on a substrate. Upon absorbing the laser energy, the scanned powder particles melt and rapidly solidify, forming a single track. The final three-dimensional component is then built by repeating this layer-by-layer process[4]. LPBF offers several advantages over conventional manufacturing methods such as casting and milling, including greater design freedom, reduced material waste, and shorter lead times[5].

Despite these advantages, components produced by LPBF are still susceptible to various defects, including denudation zones[6], surface porosities[7], keyhole porosities[8], voids[9], and cracks[10]. These defects, which are highly dependent on complex multi-physics phenomena during processing, can compromise the mechanical integrity and reliability of the final part. Consequently, current LPBF technology still faces significant challenges before widespread industrial adoption, particularly regarding a comprehensive understanding of the underlying physical mechanisms and the precise control of process parameters.

In this context, the present study aims to systematically investigate the fundamental mechanisms governing melt pool dynamics and spattering behavior in the LPBF process, and to elucidate their correlation with defect formation. To achieve this, a combined experimental and numerical approach is adopted. The primary research objectives are: (i) to develop a multi-physics modeling framework capable of simulating powder spreading and melt pool evolution; (ii) to experimentally validate the numerical models using microstructural characterization; (iii) to analyze the influence of key process parameters, particularly laser power and scanning speed, on melt pool stability, denudation, and spattering intensity; and (iv) to provide insights into defect mitigation strategies for improved process stability and part quality.

This report is structured into seven chapters. Chapter 1 provides a brief research background and outlines the scope and objectives of this study. Chapter 2 presents a comprehensive literature review on LPBF, covering defect formation mechanisms, the influence of process parameters, and the current understanding of flow and heat transfer during processing. Chapter 3 describes the multi-physics modeling framework developed in this work, including a discrete element method (DEM)-based powder spreading model and a thermal-fluid flow model for melt pool simulation. Detailed descriptions of the geometry, governing equations, boundary conditions, initial conditions, and material properties are provided. Chapter 4 focuses on experimental methodology and numerical model validation. The experimental setup, including the LPBF system, powder characterization, high-speed camera configuration, and post-process characterization techniques, is introduced. Numerical results are systematically compared with experimental observations to validate the models. Chapter 5 investigates the mechanisms of melt pool dynamics. The relationship between melt pool dynamics and interfacial heat flux is analyzed. Combined with Marangoni circulation, the effects of thermal inhomogeneity on humping and balling defects, as well as the role of heat transfer in porosity formation, are discussed. The influence of preheating on melt pool behavior is also examined, supported by experimental results. Chapter 6 explores spattering dynamics. The mechanisms of vapor-induced powder entrainment and the effect of scanning speed on spatter spatial distribution are studied in detail. Key aspects such as the onset of particle motion, detachment dynamics of single and clustered particles, and spatter re-deposition mechanisms are analyzed. The role of melt pool wetting in determining final spatter behavior is also addressed. Finally, Chapter 7 summarizes the key findings of this study, highlighting the primary factors governing melt pool and spatter dynamics. Based on the integrated experimental and numerical results, the importance of multi-physics coupling in understanding particle mobilization and defect formation is emphasized. Future research directions, including adaptive process control, integrated melt pool–spatter simulation, and strategies for spatter mitigation, are proposed to further enhance LPBF process stability and part quality.

Chapter 2. Literature review

2.1 The principle of the LPBF technique

The history of Laser powder bed fusion (LPBF) can be traced back to 1995, when Fockele and Schwarze invented the MCP Realizer system-an early LPBF apparatus based on the principles of Selective Laser Sintering (SLS)-and were granted a German patent (DE 19649865) [11]. While LPBF and SLS share certain conceptual similarities, they differ fundamentally in whether the powder material is fully melted and whether low melting point alloys are required as binding agents. The first commercial LPBF equipment, the SLM-50, was introduced in late 2003 by Realizer, a subsidiary of the German MCP-HEK operating under the British MCP (Mining and Chemical Products Limited) Group. Since then, numerous companies have developed commercial LPBF systems capable of producing metallic components with dense microstructures, high dimensional accuracy, and favorable mechanical properties. In parallel with industrial development, extensive academic research has been carried out on the theoretical foundations, process optimization, and application potential of LPBF. Institutions actively engaged in such research include the Oskada Laboratory in Japan, KU Leuven in Belgium, the University of Leeds in the United Kingdom, and Nanyang Technological University in Singapore.

The Laser powder bed fusion (LPBF) process comprises multiple stages, starting with the generation of CAD data and concluding with the removal of the finished component from the build platform, as illustrated schematically in Fig. 2.1[12]. Given the extremely high temperatures necessary for melting, the fabrication is conducted within a controlled, low-oxygen environment using an inert shielding gas such as argon or nitrogen to prevent oxidation and other defects that could compromise the mechanical properties of the final part [13]. Initially, a detailed 3D model of the part to be printed is generated using specialized 3D modeling software. Subsequently, slicing technology converts this 3D model into a series of discrete layers of defined thickness and sequence, which are saved as files suitable for laser scanning. The building process commences by evenly spreading a thin layer of metal powder over a substrate plate inside the build chamber. A high-energy-density laser then selectively fuses the powder according to the programmed data. After the laser completes scanning a layer, the build platform is lowered by one layer thickness, a new layer of powder is deposited, and the laser proceeds to fuse the next layer. This cycle of layering and laser scanning continues iteratively until the entire component is fully formed[14].

Compared to traditional manufacturing methods, metal parts produced by Laser powder bed fusion (LPBF) technology offer the following advantages [15]-[18]:

I. The manufacturing process is straightforward, and once production is complete, only minimal post-processing steps such as sandblasting and polishing are required.

II. LPBF supports a wide range of materials, including stainless steel, titanium alloys, aluminum alloys, nickel-based superalloys, CoCr alloys, and other metals.

III. The final metal components are directly formed, eliminating the need for mold fabrication and additional processing stages, thereby significantly shortening the production cycle.

IV. The process yields a uniform and fine metallographic structure, resulting in part densities approaching 100%. Consequently, the mechanical properties are excellent, with some components exhibiting performance equal to or surpassing that of forged counterparts.

V. By employing a high-power-density laser with a small spot diameter and thin layer thickness, the manufactured parts achieve high dimensional accuracy and superior surface quality with minimal roughness.

VI. LPBF is particularly well-suited for fabricating workpieces with complex internal geometries that are difficult or impossible to produce using conventional methods.

VII. The technology allows for flexible production of small batches and customized parts tailored to specific user requirements.

In summary, LPBF technology overcomes the limitations of traditional manufacturing methods in fabricating complex structures. It enables the efficient production of metal parts with intricate geometries, drives the advancement and application of diverse metal materials across various industries, and holds broad prospects for future development.

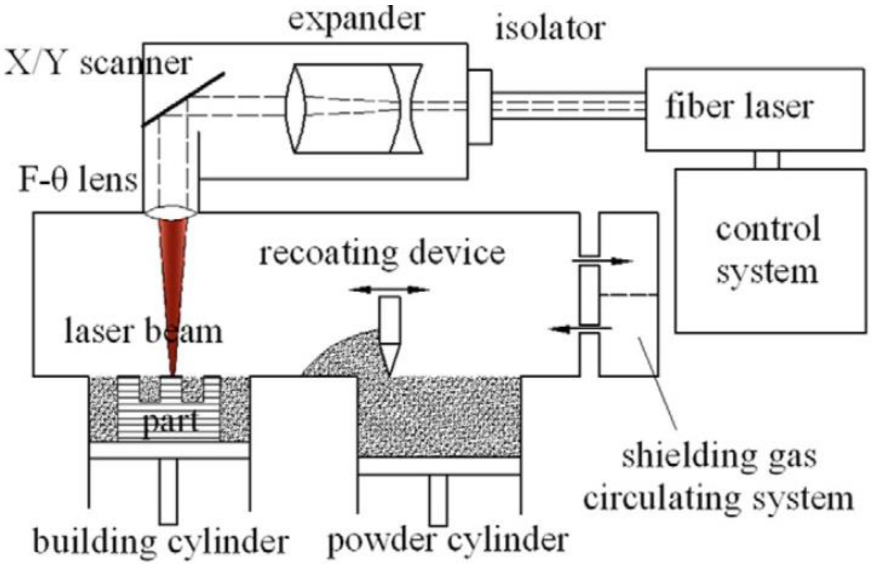

Fig. 2.1. Schematic diagram of LPBF machine[12].

2.2 Application of LPBF

The LPBF technique has been extensively applied in the production of prototypes and small-batch parts across a variety of industries, including aerospace, biomedical engineering, mold manufacturing, automotive components, jewelry, and more.

2.2.1 Biomedical application

Among all LPBF applications, the biomedical field imposes the most stringent individual requirements, making it unsuitable for mass production. However, due to the inherent characteristics of the LPBF process-such as digitization, networking, personalization, and customization-it is particularly well-suited for the direct fabrication of components used in organ repair and replacement.

Fig. 2.2. Real biological models produced by laser powder bed fusion[19].

Wehmöller et al.[19] produced the biological structures in the displayed complexity using stainless steel for the first time with LPBF technology, demonstrating LPBF's ability to fabricate patient-specific implants that precisely match individual anatomical defects, as shown in Fig. 2.2. Zhang et al.[20] obtained knee joints using Ti-24Nb-4Zr-8Sn material with LPBF technology, and the density was greater than 99%, as shown in Fig. 2.3. De Wild et al.[21] made a titanium-based bone replacement with LPBF implanted in the calvaria of New Zealand rabbits to mimic cancellous bone's mechanical and structural properties while avoiding stress shielding. The osseointegration of all generatively formed porous Ti structures into the surrounding bone was excellent. Demir et al.[22] produced cardiovascular stents with acceptable geometrical accuracy using LPBF of CoCr alloy powder, and surface quality was improved by electrochemical polishing, which suggests that LPBF may be used to shape precursors in stent fabrication instead of microtube manufacturing and laser microcutting. Limmahakhun et al. [23] presented the CoCr graded femoral stems with a porosity reduction caudally and inwardly, keeping relative micromotions within an acceptable range for bone ingrowth and achieving flexural stiffness similar to human femurs. LPBF technology also has a wide range of applications in dentistry. Vandenbroucke et al. [24] successfully built frameworks with good mechanical properties and corrosion behavior using LPBF for complex dental prostheses supporting the artificial teeth, which are screw-retained on edentulous patients' jawbone implants. In addition, LPBF molding of 316L stainless steel, titanium alloy, CoCr alloy, and other medical metal materials is widely used in cranial restorations, spinal fusion instrumentation, and other fields.

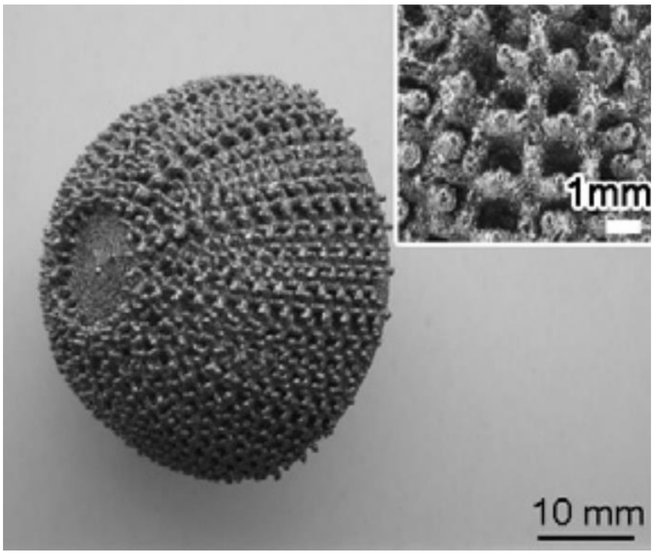

Fig. 2.3. An example of precise acetabular cup produced by LPBF[20].

2.2.2 Aerospace application

In the aerospace sector, LPBF technology is commonly employed for the fabrication of small to medium-sized components with complex geometries. NASA used GRCo-84 material by LPBF to print the first full-scale copper rocket engine part, with ten times faster manufacturing and more than 50% lower cost[25], as shown in Fig. 2.4(a). In 2015, Monash University researchers manufactured the world's first 3D-printed jet engines, a development that might alter how aircraft are built[26], as shown in Fig. 2.4(b). Also, the Russian Institute of Aeronautical Materials produced tiny gas turbine engines for drones using LPBF technology with guide vanes in Inconel 738 powder[27]. LPBF Solutions and Cellcore[28] collaborated on a rocket propulsion engine based on LPBF technology with integrated lattice internal cooling channels that provide an optimal relationship between stability and mass application of the thrust chamber, as shown in Fig. 2.4(c). Shi et al.[29] developed a heavy-loaded aerospace bracket with topology optimization and fabricated it using LPBF technology, resulting in a mass reduction of nearly 18%, as shown in Fig. 2.5. Therefore, reduced lead time and related costs and the capacity to design and produce complicated geometries that enable lightweighting, consolidation of many components, and performance enhancements are all benefits of using LPBF technology for aerospace components.

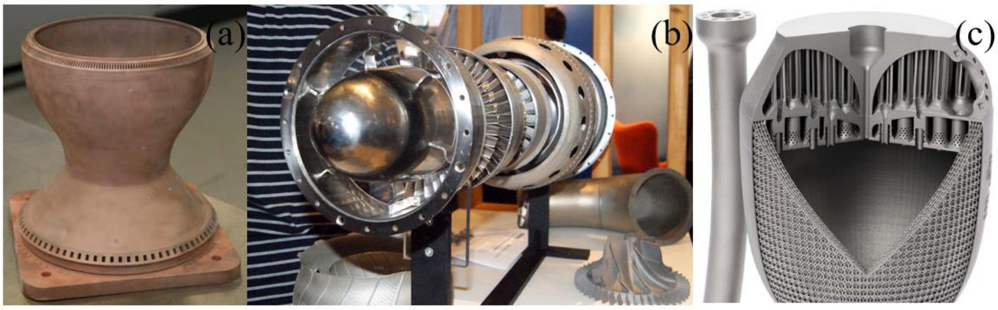

Fig. 2.4. (a) full-scale copper rocket engine part[25], (b) jet engines made by LPBF[26], and (c) Cellcore prototype rocket nozzle featuring internal cooling channels[28].

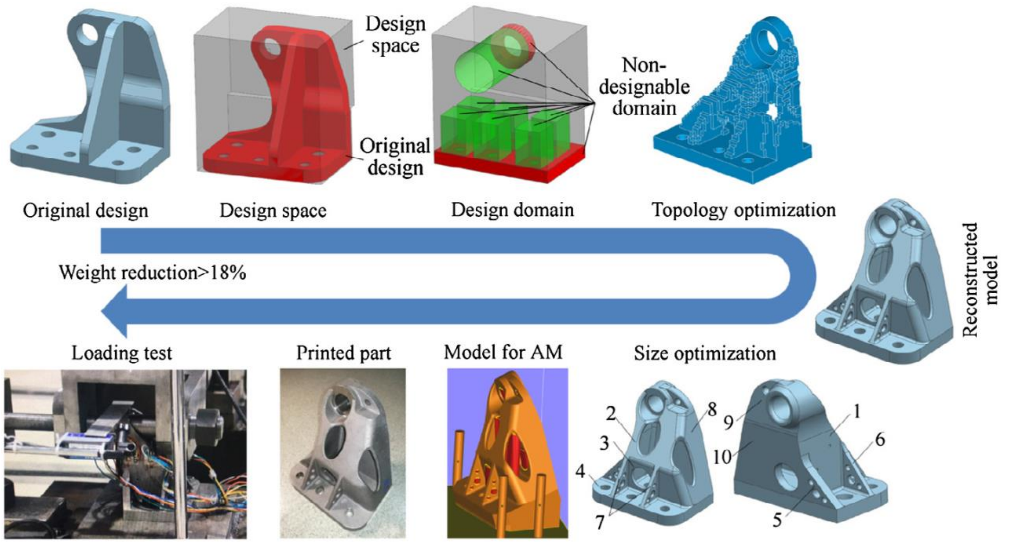

Fig. 2.5. Aerospace bracket designed by topology optimization and manufactured by LPBF[29].

2.2.3 Mold manufacturing application

Currently, LPBF technology has been widely adopted in mold production and has gained broad recognition within the industry. In 2007, Beal et al.[30] find that the 50% Cu–H13 insert produced by LPBF was better than the pure H13 insert in transporting heat away from the component. In 2011, Wang et al.[31] used LPBF to fabricate a mold with complex conformal cooling channels using 316L stainless steel powders, which shows that the LPBF-produced mold has high precision and performance, and the cooling efficiency of conformal cooling channels in the mold has substantially increased, as has the cooling uniformity. In 2013, Armillotta et al.[32] conducted a study of LPBF forming H13 steel combined with CNC technology to manufacture conformally cooled die-casting molds, demonstrating that the revised mold has been utilized for approximately 2,000 cycles without wear or damage, and the LPBF mold may be employed in short-run production applications, as shown in Fig. 2.6. In 2015, Holzweissig et al.[33] fabricated H13 tool steel using LPBF, which improves the mechanical properties of such steels without needing a subsequent heat treatment. In 2016, Sander et al.[34] successfully processed the high-strength tool steel Fe85Cr4Mo8V2C1 using LPBF, which had better attributes to the as-cast condition without postprocessing, such as an improved compression strength of 3796 ± 163 MPa and microhardness of 900 ± 12 HV 0.1, as shown in Fig. 2.7.

Fig. 2.6. Hybrid construction of the impression block by LPBF and CNC[32].

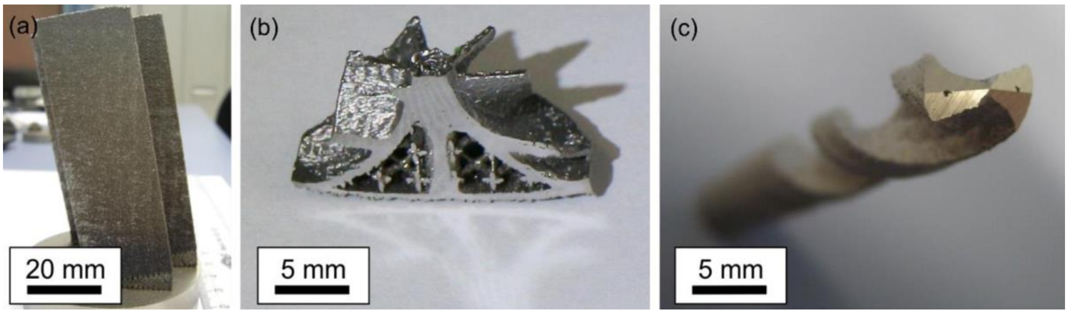

Fig. 2.7. Different components of the high-strength steel alloy FeCrMoVC produced by LPBF: (a) large dense and crack free volume parts, (b) impeller part with integrated lattice structure and (c) drill with integrated cooling channels[34].

At present, companies such as EOS, MCP, and Concept Laser have successfully utilized rapid prototyping equipment to manufacture various mold components-including punching dies, die-casting molds, and injection molds-with high surface quality and dimensional accuracy. These parts often meet the requirements for direct application without the need for further post-processing. However, the range of metal materials available for LPBF-based mold manufacturing remains relatively limited and does not yet fully meet the demands of future production and technological development.

2.2.4 Automotive application

The structure of modern automobiles is highly complex, consisting of approximately 30,000 individual components. Traditionally, each part is manufactured separately and later assembled into a complete vehicle through mechanical fastening methods such as screwing or welding. However, in theory, the larger the number of components, the lower the overall safety and reliability of the vehicle, as connecting joints are often the most failure-prone areas during regular operation.

Laser powder bed fusion (LPBF) offers a promising solution to this issue by enabling the integration of multiple traditionally separate components into a single, consolidated structure. This design freedom allows for the reduction of part counts, thereby simplifying assembly procedures and significantly enhancing production efficiency. Additionally, by minimizing the number of mechanical joints, the safety, structural integrity, and reliability of the vehicle are greatly improved. Furthermore, LPBF technology allows for the production of lightweight, high-strength parts with complex internal structures such as lattice geometries or cooling channels-features that are difficult or impossible to achieve using conventional manufacturing methods. These capabilities are particularly advantageous for applications in motorsport, electric vehicles, and high-performance automotive systems where weight reduction and performance optimization are critical. Fig. 2.8 illustrates examples of automotive components fabricated using the LPBF process by SLM Solutions, showcasing the potential of this technology in modern automotive manufacturing.

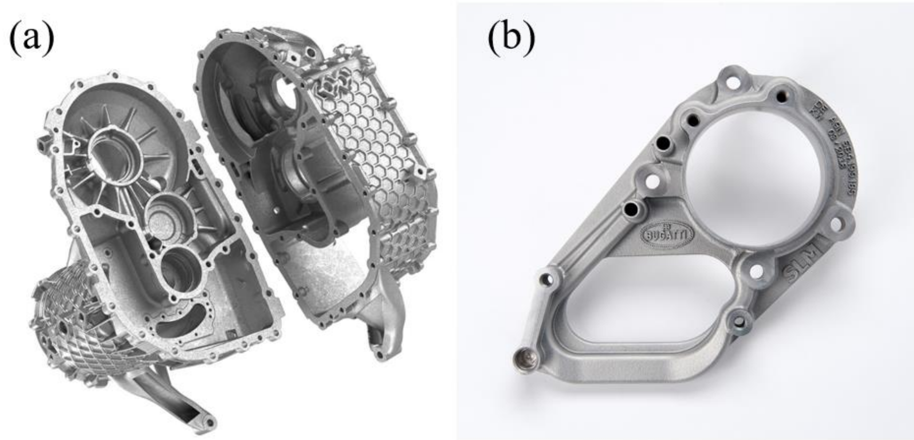

Fig. 2.8. Automotive parts manufactured by LPBF (a) The complete E-drive housing with an innovative Design (b) The active heat shield to the motor's electric pump.

2.2.5 Jewelry application

With the continuous improvement of living standards and the advancement of social aesthetics, consumer demand for personalized and customized jewelry has grown significantly. Traditional manual craftsmanship, while rich in cultural value, often faces limitations in terms of design complexity, repeatability, production speed, and material utilization.

LPBF technology introduces a new paradigm for jewelry design and manufacturing. By enabling the creation of highly intricate geometries and fine surface details, LPBF breaks through the singularity and constraints of conventional techniques, allowing designers to realize innovative forms that were previously difficult or impossible to achieve. This includes delicate lattice structures, hollow patterns, complex filigree, and integrated functional elements. Moreover, LPBF supports digital design workflows, making it highly compatible with CAD-based customization. This allows for rapid prototyping and direct fabrication of bespoke pieces tailored to individual customer preferences, significantly shortening the design-to-product cycle. It also reduces material waste compared to subtractive methods and opens up possibilities for small-batch or one-off production without the need for costly molds.

The combination of precision, flexibility, and personalization brought by LPBF has contributed to the diversification, refinement, and democratization of jewelry production, making unique designs more accessible to the broader public. An illustrative example of LPBF application in jewelry design is the "Guardian" piece[35], as shown in Fig. 2.9. The jewelry exhibits excellent surface quality and metallic texture, with no visible defects such as warping or deformation. The measured surface roughness was 11 μm, indicating that after post-processing treatments like sandblasting, polishing, and plating, the piece can be directly used as a finished product.

Fig. 2.9. Personalized “Guardian” jewelry produced by LPBF[35].

2.3 Defects formation during LPBF process

As a highly complex additive manufacturing technique, the LPBF process is governed by a multitude of interdependent parameters, including laser power, scanning speed, hatch spacing, layer thickness, powder material characteristics, and the chamber environment. Each of these parameters plays a critical role in determining the stability and efficiency of the melting process, as well as the final morphology and mechanical performance of the fabricated part. Moreover, these parameters do not operate in isolation; their interactions can amplify or mitigate the effects of one another, making process optimization particularly challenging.

Despite its many advantages, LPBF is inherently sensitive to deviations in processing conditions. Improper parameter selection or control can lead to a range of defects that compromise the quality and functionality of the final component. In the literature, these defects are commonly discussed under four main categories: spattering, porosity, cracking, and surface roughness[36][38]. Understanding the mechanisms behind the formation of these defects is essential for improving part quality, optimizing process parameters, and expanding the industrial applicability of LPBF technology.

2.3.1 Spattering

Spattering is regarded as a critical defect in the LPBF process due to its potential to interfere with the laser-material interaction and disrupt the overall stability of the melting process. During fabrication, spatter can obstruct the laser beam path, reducing the effective energy input to the melt pool. This insufficient energy delivery may result in an unstable molten pool, thereby promoting the formation of secondary defects such as porosity, lack of fusion, and inconsistent layer bonding [39].

If spattered material is redeposited within the intended build area, it may act as a source of contamination. These particles are often not fully remelted in subsequent layers, leading to inclusions, weak interfaces, or even delamination. Moreover, such irregular deposits can disturb the uniformity of powder recoating, compromising the quality of successive layers and ultimately affecting the geometric precision and mechanical properties of the final component[12].

Spattering in LPBF is typically categorized into two main forms: (1) the ejection of molten metal droplets from the melt pool, often driven by recoil pressure or Marangoni convection- a phenomenon where surface tension gradients induced by temperature variations drive fluid flow- within the pool [40]; and (2) the displacement or ejection of loosely bound powder particles surrounding the melt pool, induced by vapor plume dynamics or shockwaves[41]. These mechanisms are schematically illustrated in Fig. 2.10, highlighting the complex interplay between laser-material interaction and surrounding powder behavior.

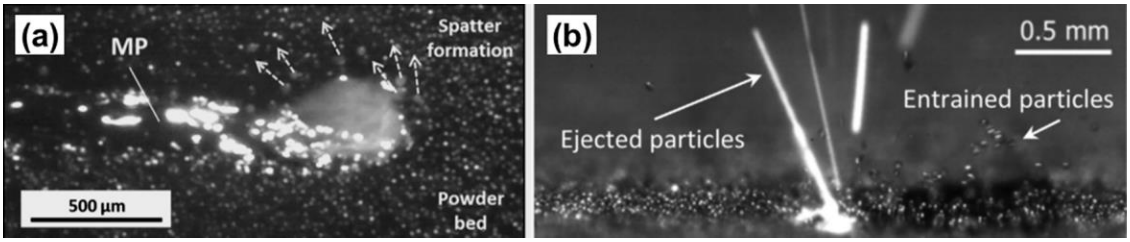

Fig. 2.10. Different types of spatters during LPBF. (a) Ejection of liquid metal from the molten pool[40]. (b) Ejection of partially melted powder particles approaching the laser plume and scattering of the moving solid powder particles beyond the molten pool[41].

I. Ejection of liquid metal droplets

During the LPBF process, the interaction between the high-energy laser beam and the metal powder generates extreme thermal gradients, resulting in rapid melting and vaporization. The intense vaporization at the molten pool surface induces a significant recoil pressure, which acts as a mechanical force opposing the surface tension of the liquid metal. When this recoil pressure exceeds the stabilizing surface tension at the melt pool boundary, liquid metal droplets may be expelled from the surface-a phenomenon commonly referred to as droplet spattering.

DebRoy et al. [42][43] and Kawahito et al. [44] established that under high laser power density, the vapor recoil force can overcome the surface tension of the molten metal, particularly at the pool edges, leading to the ejection of fine droplets from the melt pool. Similar observations were made by He et al. [45], who reported that increasing the laser power density not only amplified the recoil effect but also led to the generation of larger droplets and a broader particle size distribution. They also proposed that the formation of a pronounced depression in the center of the molten pool - caused by elevated recoil pressure - can serve as an indicator of impending droplet ejection, as illustrated in Fig. 2.11.

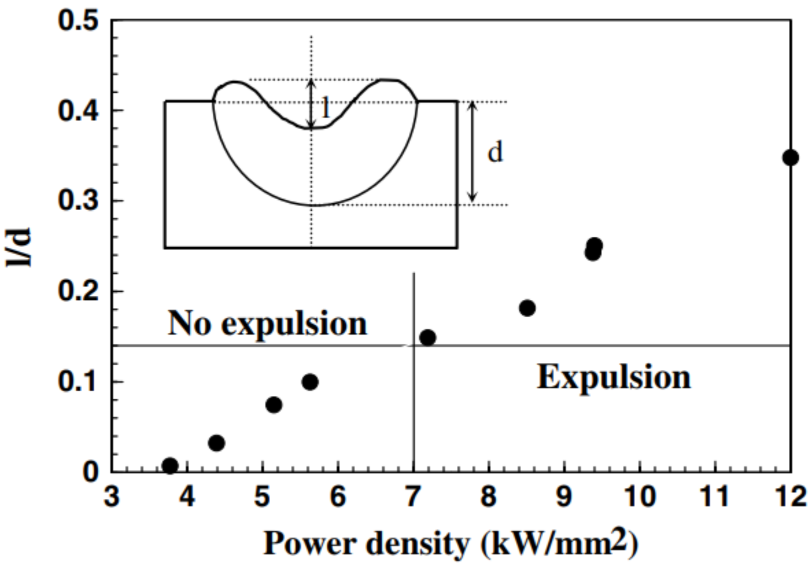

Fig. 2.11. Variation of *l/d* with the laser power density. Pulse duration: 4 ms [45].

Although vapor recoil pressure has long been considered the dominant mechanism behind droplet spattering, more recent studies suggest a more nuanced understanding. Ly et al.[46] quantified that vapor recoil-induced droplet ejection accounts for approximately 15% of total spatter formation. They attributed the majority of the spatter generation to vapor plume-induced entrainment, where fine particles are dragged out of the powder bed by turbulent gas flows in the vicinity of the melt pool. Wang et al.[47] proposed a more comprehensive mechanism, identifying three key contributors to spattering: recoil pressure, thermally induced Marangoni convection within the molten pool, and localized heat accumulation. These combined effects lead to the ejection of molten droplets with average sizes around 162 μm-substantially larger than the nominal particle size of the original powder feedstock (~32 μm), as shown in Fig. 2.12. Importantly, these spattered droplets are often redeposited on the part surface or incorporated into the bulk material, potentially leading to internal defects, surface irregularities, and degraded mechanical properties. Simonelli et al.[48] further observed that spattered droplets not only exhibit increased particle size but also develop surface oxidation layers several micrometers thick, which can compromise the chemical and structural integrity of the manufactured parts.

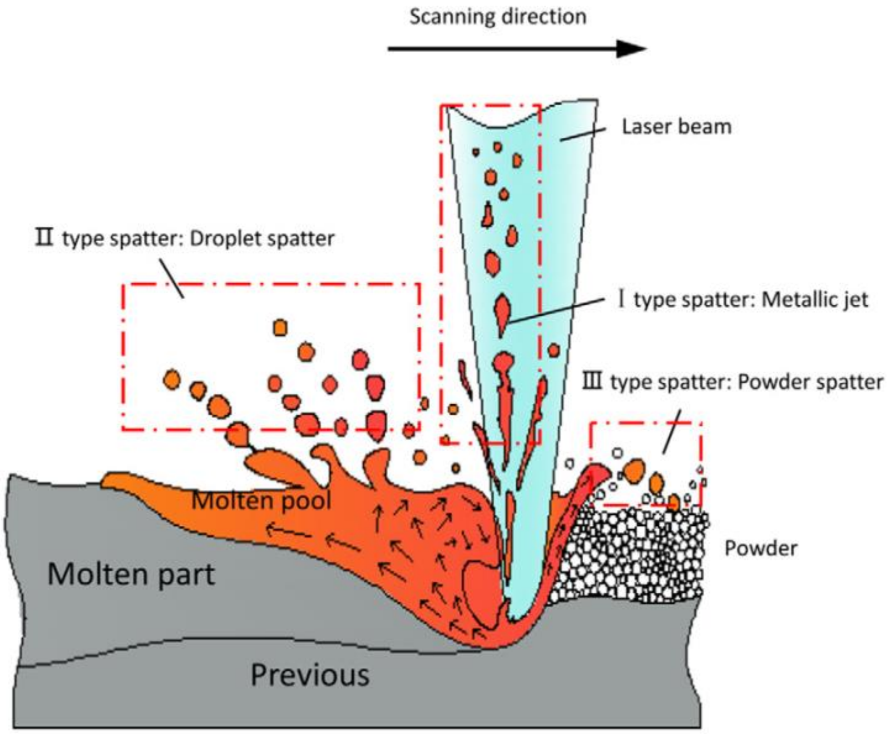

Fig. 2.12. Formation mechanisms of three different types of spatters[47].

II. Ejection of powder particles

In the LPBF process, the rapid evaporation of molten metal generates a high-velocity vapor jet, which induces a localized pressure gradient and generates a strong inward gas flow due to the Bernoulli effect—a fluid dynamics principle where an increase in fluid velocity is accompanied by a decrease in static pressure [6]. This pressure reduction draws surrounding shielding gas—and with it, nearby powder particles—toward the vapor jet. These entrained particles may then be ejected from the powder bed. Depending on whether they intersect with the laser beam during ejection, they are classified as either hot ejecta (if melted or partially melted by the beam) or cold ejecta (if they remain solid) [49].

The sequence of physical phenomena includes laser-induced melting, vapor jet generation, shielding gas flow initiation, and subsequent powder entrainment—all occurring over different timescales. Specifically, melting takes place over a few microseconds, vapor jet formation occurs within tens of microseconds, and the shielding gas (typically argon) develops a consistent flow field over hundreds of microseconds [50]. These complex interactions result in multiple spattering pathways, schematically illustrated in Fig. 2.13 [46].

According to Ly et al. [46], the entrained powder particles follow three primary trajectories. First, some particles are drawn into the molten pool and become fully incorporated into the deposited track. Second, particles that are entrained but do not intersect with the laser beam escape as *cold* ejections. Third, particles that are partially irradiated by the laser beam become *hot* ejections-these are typically semi-molten and exhibit higher kinetic energy. In a typical parameter range with laser powers of 200-300 W and scanning speeds of 1.5-2.0 m/s, hot ejections account for approximately 60% of total spatter, cold ejections for 25%, and recoil pressure-induced droplet ejections for the remaining 15%.

Vapor jet-driven powder ejection occurs predominantly near the laser interaction zone, while the shielding gas contributes to particle movement both ahead of and behind the scanning path. Notably, the velocity and momentum of vapor-driven particles are an order of magnitude greater than those propelled by the shielding gas flow [50], due to the significantly higher acceleration generated by vapor recoil.

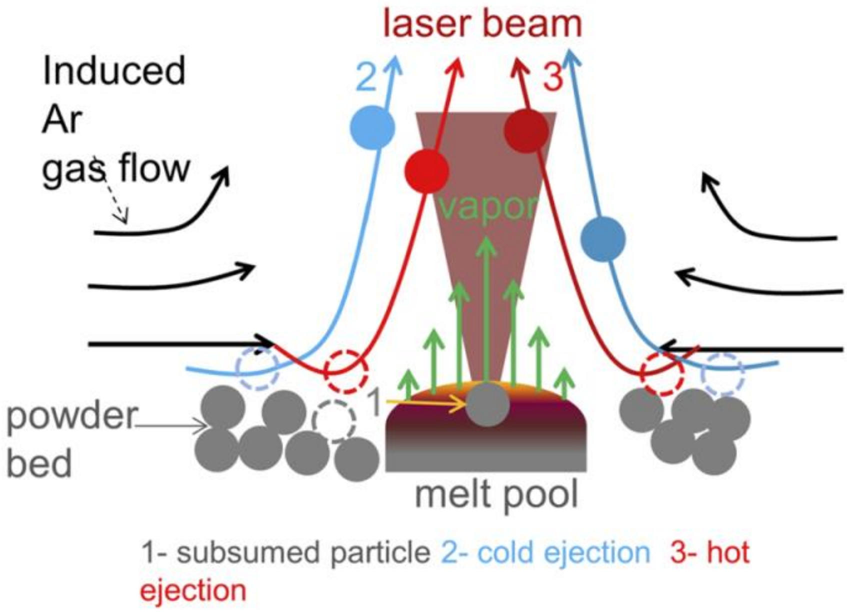

Fig. 2.13. Schematic depicting particle entrainment of the powder bed by an induced argon gas flow for a stationary laser beam[46].

During laser exposure, localized heating can elevate powder particles to near-boiling temperatures within a few microseconds [6], which is considerably shorter than the characteristic time for thermal conduction through a particle (typically tens of microseconds). Consequently, only specific regions of a particle are heated, resulting in steep internal temperature gradients. This asymmetric heating produces localized recoil forces on the particle surface, leading to the ejection of partially molten particles as high-energy hot spatters [46].

Moreover, ejected hot particles in flight may undergo secondary interactions, including collisions with other particles. These interactions can lead to energy transfer and velocity redistribution, occasionally resulting in the formation of weakly sintered agglomerates or strongly bonded clusters. If redeposited, such clusters may become embedded within the build, potentially introducing defects such as porosity or lack of fusion in subsequent layers [47][49].

2.3.2 Porosity

Pore formation is one of the most typical defects in LPBF parts, including lack of fusion among neighboring tracks, unstable keyhole collapse, and gas-induced pores.

I. Lack of fusion

Due to the lack of energy input, the metal powder is not entirely melted with insufficient overlap between adjacent deposit tracks resulting in a lack of fusion (LOF) defects. There are two kinds of LOF defects: (1) inadequate bonding flaws caused by the lack of molten metal during the solidification process, as shown in Fig. 2.14(a), and (2) un-melted metal powders defects, as shown in Fig. 2.14(b) [51].

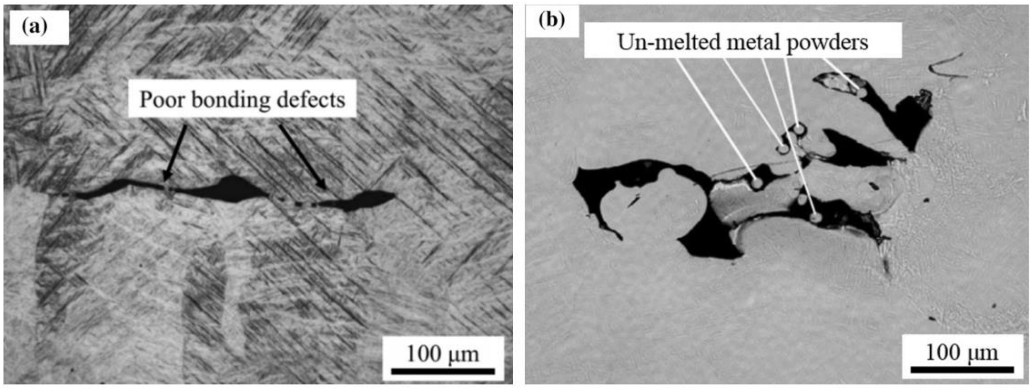

Fig. 2.14. Optical images of LOF defects in LPBF fabricated parts: (a) poor bonding defects; (b) LOF defects with un-melted metal powders[51].

In the LPBF process, the entire part is printed by the laser, selectively melting metal powder point by point, row by row, layer by layer. When the laser energy input is insufficient, the small width of the molten pool leads to inadequate overlap of adjacent scan tracks, leaving unmelted powder between the scan tracks. In depositing a new layer process, these powders are difficult to fully re-melt with incomplete fusion pores formed in part and remaining. In addition, if the laser energy input is insufficient to achieve sufficient molten pool penetration depth, LOF faults may result from weak interlayer bonding [7][51][52]. As a result, LOF defects are commonly seen in both the scan tracks and the deposited layers. Two instances of lack of fusion caused by too high hatch spacing and layer thicknesses are shown in Fig. 2.15 [53][54]. Defects that lack fusion may have extended, irregular forms with sharp edges. The surface will also become rough at the defect location, resulting in poor flow of molten metal and the formation of interlayer defects. During successive depositions, interlayer defects will gradually extend and propagate upward, accumulating into larger multilayer defects. [54].

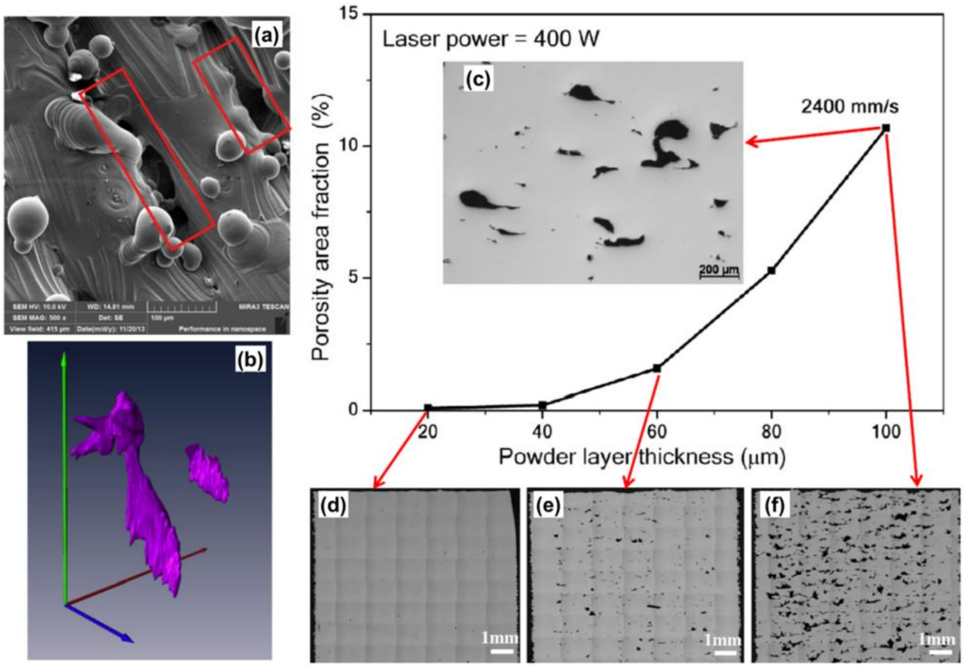

Fig. 2.15. Lack of fusion defects (a) Observed in SEM image, and (b) 3D reconstructed synchrotron radiation micro-CT images[54]. (c)-(f) Dependence of area fraction of porosity on powder layer thickness[53], LPBF of Ti-6Al-4V, 400 W laser power, and 2400 mm/s scanning speed.

Another situation is that in the LPBF process, an oxide film is usually formed on the surface of easily oxidizable alloy materials such as aluminum and AlSi10Mg, which reduces the wettability and hinders the flow of molten metal, resulting in poor interlayer bonding and incomplete fusion defects [55][56].

II. Keyhole-induced pores

Since the power and speed of the LPBF are high, and in many cases, the laser beam will form a keyhole resulting in a high aspect ratio of the fusion region, where the instability of the small hole will lead to the large pore formation with a portion of the underlying layer often melted by the high depth of the fusion zone[58][59]. The fusion zone may interact with a preexisting pore in the overlying layer, causing the void to propagate above its initial location. Also, Gong et al. [7] found that certain low-melting components in the alloy vaporize at high laser energy, creating gas bubbles that may appear far below the surface at the bottom of the molten pool. The solidification speed of the molten pool is so fast that the bubbles are trapped in the molten pool to form regular spherical hole defect inclusions with little time to rise and escape from the surface. Fig. 2.16 shows keyhole pore formation processes under the laser power of 382 W and various scan speeds [60]. As the scan speed increases, the keyhole-induced pores become less. As shown in Fig. 2.17, an interesting phenomenon is that the results of the powder-scale model show that the thickness of the deposited layer tends to be much smaller than the keyhole depth so that the keyhole in the subsequent melting process may reach the pore location before and release some of the pores present in the previously deposited layer [4].

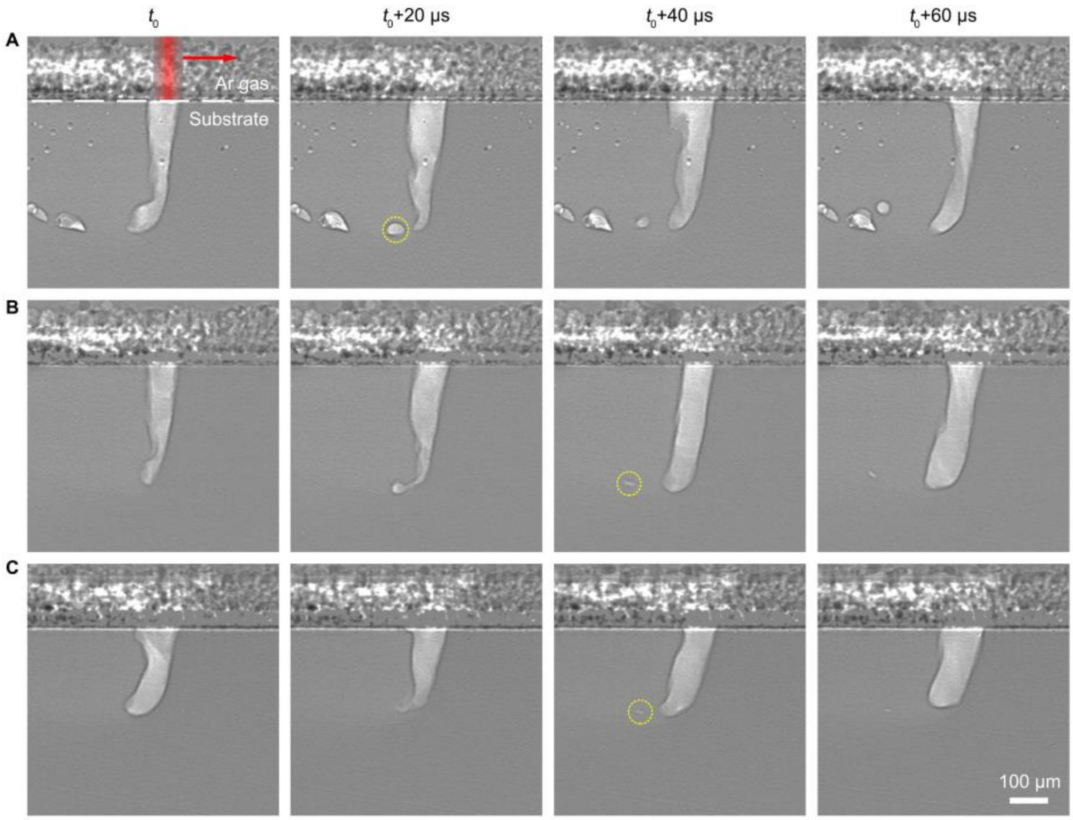

Fig. 2.16. Keyhole pore formation processes under the laser power of 382 W and at the various scan speed of (A) 500 mm/s, (B) 525 mm/s, and(C) 550 mm/s [60].

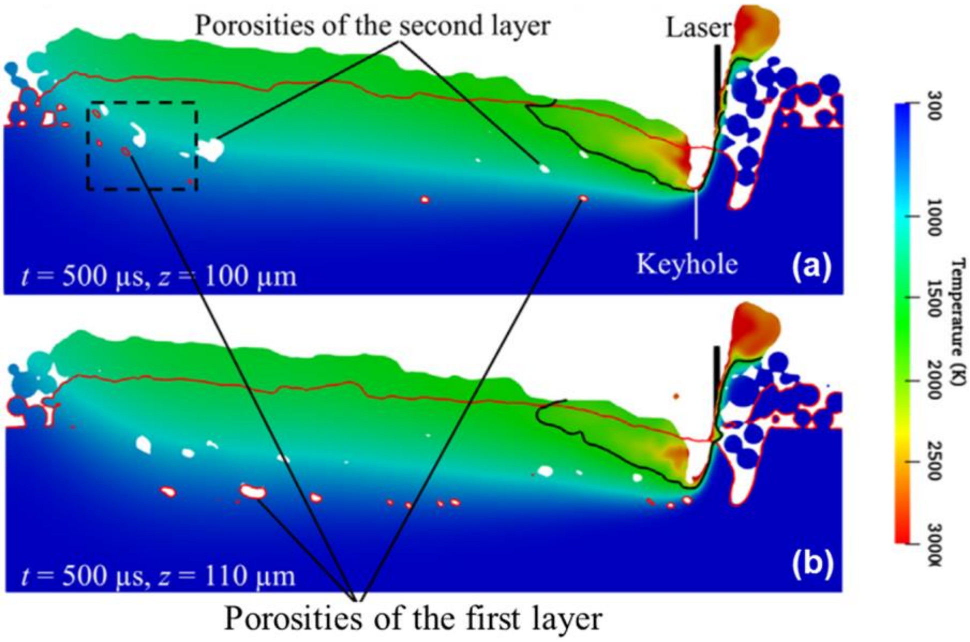

Fig. 2.17. Melt pool during deposition of the second layer with pored generated from the first layer [4].

III. Gas-induced pores

The gas-induced pores observed in LPBF fabricated parts are quite different from the lack of fusion pores and large spherical keyhole-induced pores, which are much smaller and spherical. Fig. 2.18(a) illustrates an example of the numerous small pores formed by LPBF in the deposit [9][61]. Residual pores in virgin powder particles[62], gases dissolved in liquid melt and released upon solidification, and pores previously containing entrapped metal vapors are all possible sources of these pores [63]. Fig. 2.18(b) shows tiny entrapped pores in virgin powder particles generated during the atomization process of powder particles [9][61]. The small gas bubbles get bigger during the LPBF process as they expand and merge [64]. The past aluminum alloy solidification models show that the formation of pores caused by hydrogen diffusion is related to the finite rate of hydrogen diffusion in the melt. Furthermore, the growth of pores caused by hydrogen diffusion is inhibited with an increasing cooling rate [65][66].

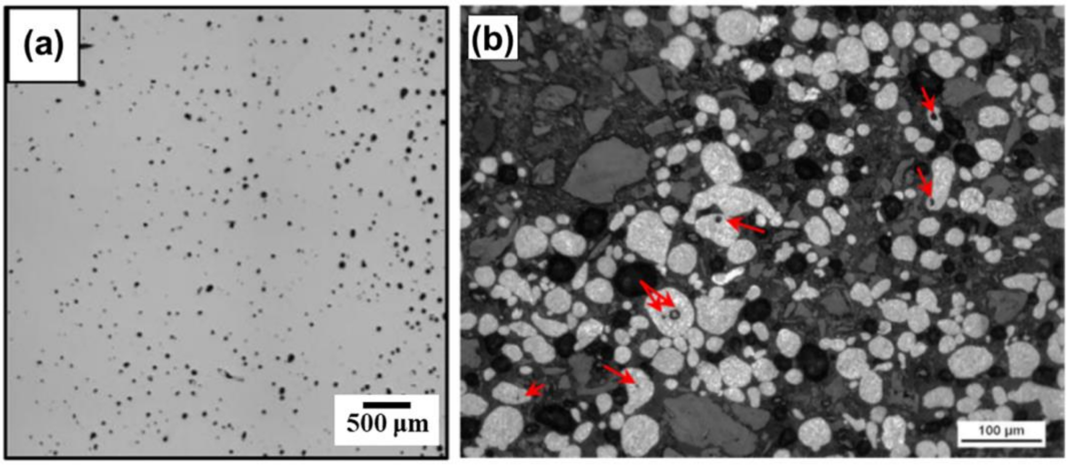

Fig. 2.18. (a) Metallurgical pores observed in the deposit [9]. Residual pores in the feedstock materials: (b) AlSi10Mg for LPBF [9].

2.3.3 Cracking

As one of the most serious defects during the LPBF process, cracking can limit the use of various promising technical materials, especially metals and alloys with poor weldability susceptible to similar cracking[67][68]. Three main types of cracking are generated in the LPBF components: solidification cracking, liquation cracking, and ductility dip cracking[68][69]. It is significant to prevent cracking formation by understanding its mechanisms.

I. Solidification cracking

Solidification cracking, also known as hot cracking, is common in LPBF parts manufactured from aluminum alloys, titanium alloys, steel, and nickel-based alloys [70], as shown in Fig. 2.19. And tensile stresses are applied to the solidifying metal because its contraction rate is much greater than that of the surrounding solid metal [73]. When tensile stresses surpass the room temperature yield strength, solidification cracking occurs, decided by and the morphology of the solidification structure and the relationship of the solid phase fraction with temperature.

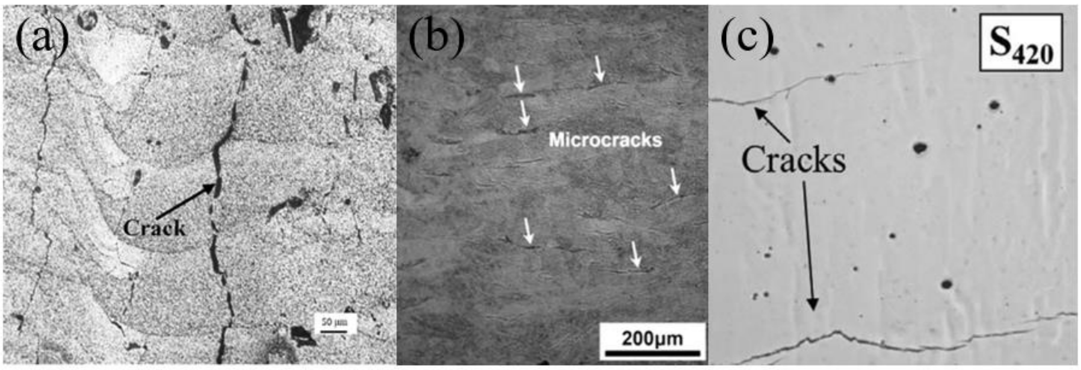

Fig. 2.19. Solidification cracking observed in the LPBF parts: (a) Al 6061[70], (b) Ti-6Al-4V[71], and (c) A high-silicon steel (6.9%wt.Si)[72].

II. Liquation cracking

Liquation cracking in laser powder bed fusion (LPBF) is commonly observed in nickel-based alloys, aluminum alloys, and austenitic stainless steels. It is primarily associated with the formation of thin liquid films along grain boundaries, which originate from the local melting of solute-enriched regions with relatively low melting points during rapid thermal cycling. During the LPBF process, the material is subjected to steep thermal gradients and repeated heating–cooling cycles. Under such conditions, grain boundary regions enriched with alloying elements may undergo partial melting, resulting in the formation of continuous or semi-continuous liquid films. These liquid films possess significantly reduced mechanical strength and are unable to accommodate the thermal and tensile stresses generated during subsequent cooling and solidification [74].

As solidification proceeds, the surrounding solid matrix contracts, imposing additional tensile strain on the weakened grain boundary regions. When the accumulated stress exceeds the load-bearing capacity of the liquid films, intergranular separation occurs, leading to the initiation of liquation cracks. These cracks typically propagate along grain boundaries, following the path of least resistance. A schematic illustration of this mechanism is shown in Fig. 2.20 [75].

In LPBF, liquation cracking is most likely to initiate in the heat-affected zone (HAZ) near the fusion boundary of previously deposited layers. It can subsequently extend into the partially melted zone and propagate along interdendritic regions, where residual liquid phases are more likely to exist. The repeated deposition of subsequent layers may further influence crack evolution and propagation behavior [76].

Although the extremely high cooling rates in LPBF tend to suppress the formation and growth of low-melting-point phases—thereby reducing the susceptibility to liquation cracking—the phenomenon cannot be completely eliminated. Under unfavorable conditions, such as pronounced elemental segregation or inappropriate process parameters, liquation cracking may still occur.

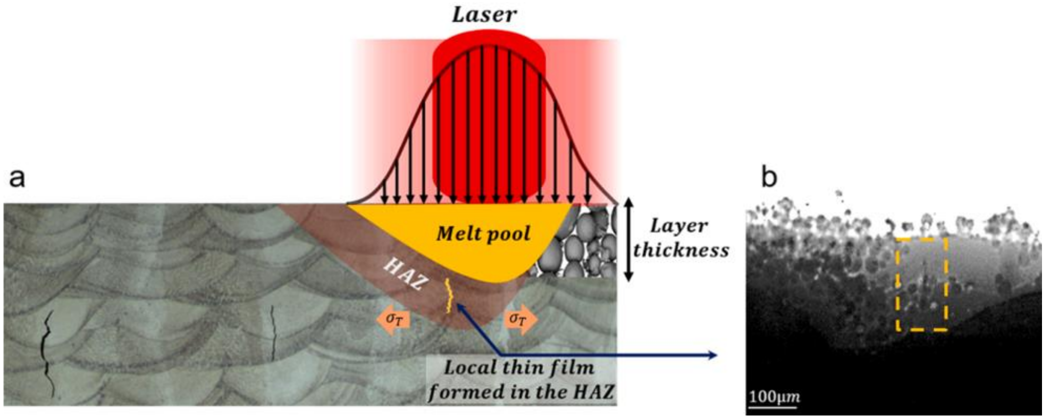

Fig. 2.20. Schematic view of the liquation cracking mechanism[75]: (a) liquation cracking in the heat-affected zone of the melt pool, and b) liquation cracking during the operando experiment.

III. Ductility dip cracking

Unlike solidification and liquidation cracking, ductility dip cracking (DDC) occurs in the absence of any liquid metal[77][78], at a temperature ranging from half the absolute melting temperature to the recrystallization or solidus temperature, followed by ductility loss of the local structure[79].

DDC is formed due to both solidification stresses and macroscopic thermal gradients generated during vigorous heating and cooling operations, as well as local stresses generated along grain boundaries. Fig. 2.21 displays a sample of the nickel-based alloy CM247LC with cracks dispersed throughout the LPBF-produced components [68]. DDC occurs when the applied strain during high-temperature processing depletes the available ductility of these alloys in this temperature range [77]. Liquation cracking and

DDC can coexist in the same part and can be differentiated via fractographic analysis. Liquation cracking is frequently identified by liquid films along the fracture path, whereas DDC does not exhibit any signs of liquation [80].

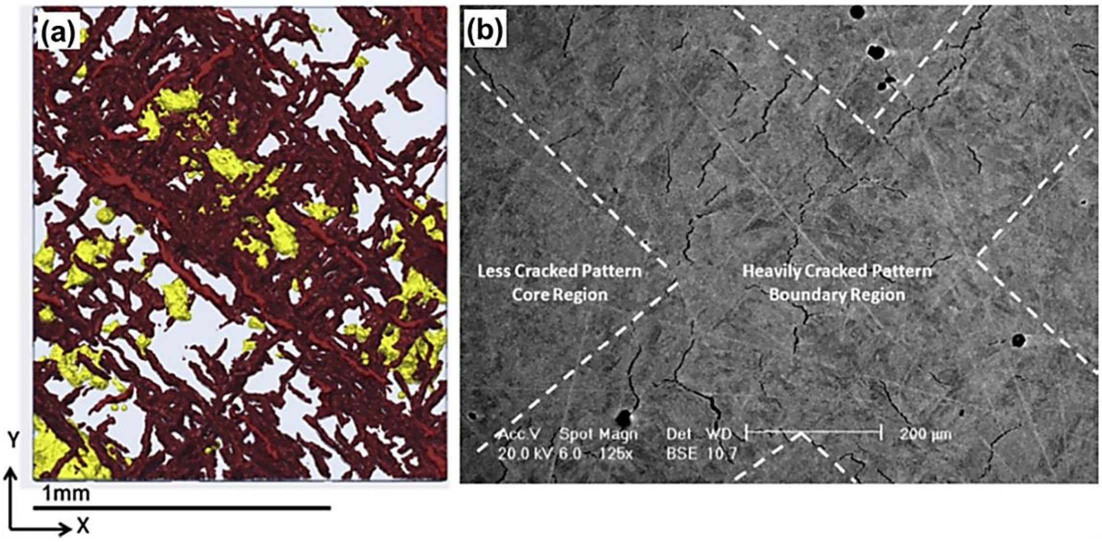

Fig. 2.21. A nickel-based alloy CM247LC: (a) MicroCT data showing the cracks in red and voids in yellow, (b) SEM micrograph showing the heavy and less cracked regions due to a repeated scanning pattern[68].

2.3.4 Surface roughness

The surface roughness of LPBF components is critical since it might impact the product's dimensions and geometrical tolerances. Fig. 2.22 illustrates the influence of the five causative factors on surface roughness, which are as follows: (1) spatters dropping on the deposit [53], (2) voids and cavities generated near the surface [81], (3) stair case effect owing to irregular transitions between nearby tracks and layers [54], (4) molten pool instabilities [82], and (5) partially melted powder particles adhered to the surface and periphery of the molten pool [83].

As illustrated in Fig. 2.22(a) and (b), spatters and pores can affect surface roughness. During the LPBF process, the metal powder denudation phenomenon near the scanning track can easily lead to irregularities on the surface of the part [6]. The sharp peaks and valleys between adjacent scanning tracks are mainly caused by inappropriate hatch spacing, layer thickness, and build angle, as shown in Fig. 2.22(c)[84]. The large spacing between two consecutive tracks often causes fluctuations in horizontal surfaces [85], while the stair case effect may affect vertical surfaces and slopes [85][86].

Also, under inappropriate conditions, dynamic instabilities such as humping and balling of the molten pool may occur due to insufficient feedstock melting [86][87]. As shown in Fig. 2.22(d), the melted particles will not spread onto the unmelted substrate but tend to aggregate, minimizing the surface area and surface energy [82]. And Fig. 2.22(e) shows that at the periphery of the molten pool, the partially melted powder particles are adhered as satellites leading to the roughness in the order of the diameters of the particles due to the nature of the powder feedstock and cannot be inevitable[83]. Therefore, when the powder particles are smaller, the average roughness of the deposit edges decreases.

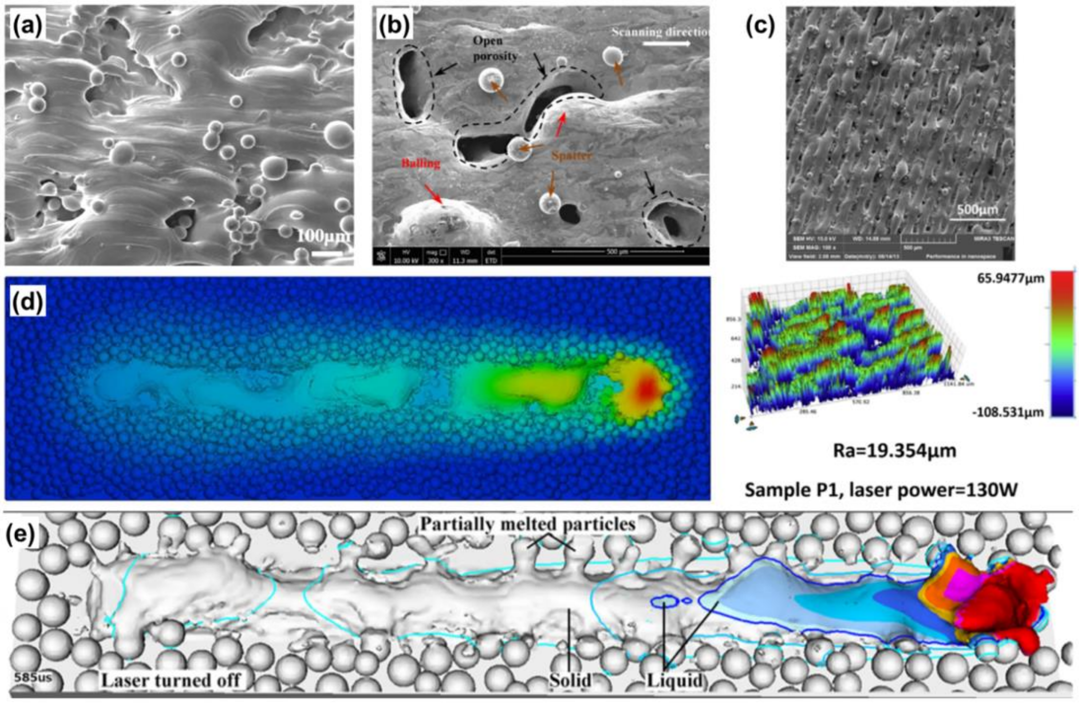

Fig. 2.22. Surface roughness due to various factors: (a) Spatters landing on the deposit surface [53], (b) Cavities and voids near the surface [81],(c) Unsmooth transitions between neighboring tracks [54], (d) Fluctuation of the molten pool [82], (e) Partially melted powder particles attached to the edges of the molten pool [83].

2.4 Effect of process factors on defect formation

Despite the numerous advantages of LPBF, including high design flexibility, near-net-shape capability, and suitability for complex geometries, the process remains susceptible to various defects. These defects-such as porosity, cracking, lack of fusion, and surface roughness-not only deteriorate the mechanical performance and dimensional accuracy of fabricated components but also hinder the widespread adoption of LPBF in critical engineering applications such as aerospace, biomedical, and tooling industries.

Understanding the underlying mechanisms of defect formation is therefore essential for enhancing part quality and ensuring process stability. Among the numerous process parameters that influence the LPBF process, two of the most critical are the laser energy input (typically characterized by laser power, scanning speed, hatch spacing, and layer thickness) and the scanning strategy (including scanning path, direction, rotation angle, and overlap rate). These parameters govern the thermal distribution within the melt pool, solidification dynamics, and powder-laser interaction-all of which play a pivotal role in defect initiation and evolution.

Comprehensive investigation of these factors provides valuable insight into optimizing process windows, improving part integrity, and tailoring material properties to specific application needs. In the following sections, the effects of laser energy input and scan strategy on defect formation will be systematically discussed.

2.4.1 Effect of laser energy input

The melting behavior of metallic powders and the dynamics of the resulting molten pool during the LPBF process are directly governed by the laser energy input. This parameter significantly influences the type, morphology, and severity of process-induced defects. The energy input is a function of several interrelated process parameters, including laser power, scanning speed, hatch spacing, and layer thickness.

When the scanning speed is relatively low, increased laser energy input leads to elevated melt pool temperatures, resulting in the excessive melting of powders and the formation of gas-induced porosity. These pores may arise due to gas entrapment from the atmosphere or from the release of gases originally present within the feedstock powder. Additionally, in aluminum and magnesium-containing alloys, low boiling point elements may evaporate under high temperatures, forming gas bubbles. Due to the rapid solidification characteristic of LPBF, these bubbles may become trapped within the molten pool, ultimately forming spherical pores that deteriorate the part's integrity [7]. Moreover, a higher energy input intensifies localized evaporation, generating a vapor plume that induces a gas flow capable of entraining and removing powder particles from regions adjacent to the scan track—a phenomenon known as denudation. This powder depletion reduces the availability of powder to bridge neighboring tracks, thereby increasing the risk of large inter-track porosity [88].

High energy input in conjunction with low scan speeds also introduces substantial thermal gradients, leading to severe thermal contraction and the accumulation of residual stresses during rapid solidification [71][89]. Such stress concentrations may contribute to cracking or delamination, especially in materials with poor ductility or large thermal expansion coefficients. Conversely, insufficient energy input—typically a result of low laser power or excessive scan speed—may lead to incomplete melting of powder particles, thereby creating lack of fusion (LOF) defects. These defects manifest as discontinuities between adjacent tracks or layers, stemming from inadequate overlap or penetration into previous layers [7][52][89][90].

To quantify laser energy input, the concept of volumetric energy density (E, J/mm^3) is widely adopted in LPBF studies. It is mathematically defined as:

$$E = \frac{P}{v \times h \times t} \tag{2-1}$$

where P is laser power (W); v is scan speed (mm/s); h is hatch spacing (mm); and t is layer thickness (mm). This equation enables the estimation of the average energy delivered per unit volume of material and is extensively used to optimize processing windows[7][88][91].

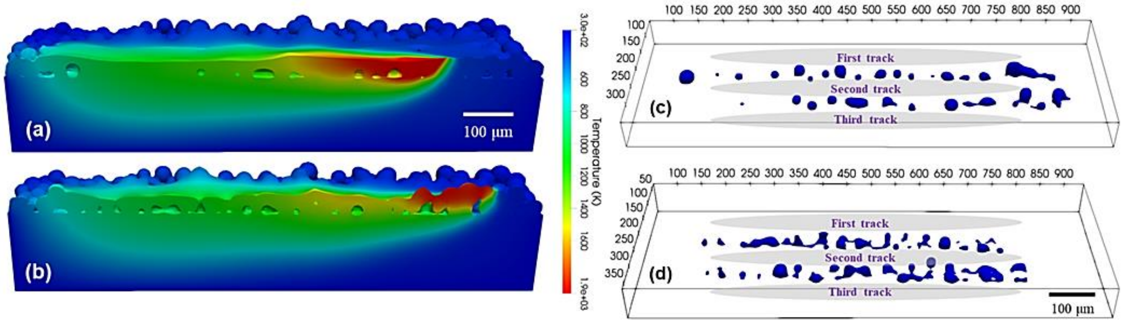

Fig. 2.23. Calculated variations of inter-track porosities during PBF-L of Ti-6Al-4V using different hatch spacings. (a) and (c) hatch spacing of 80 µm, (b) and (d) hatch spacing of 100 µm[92].

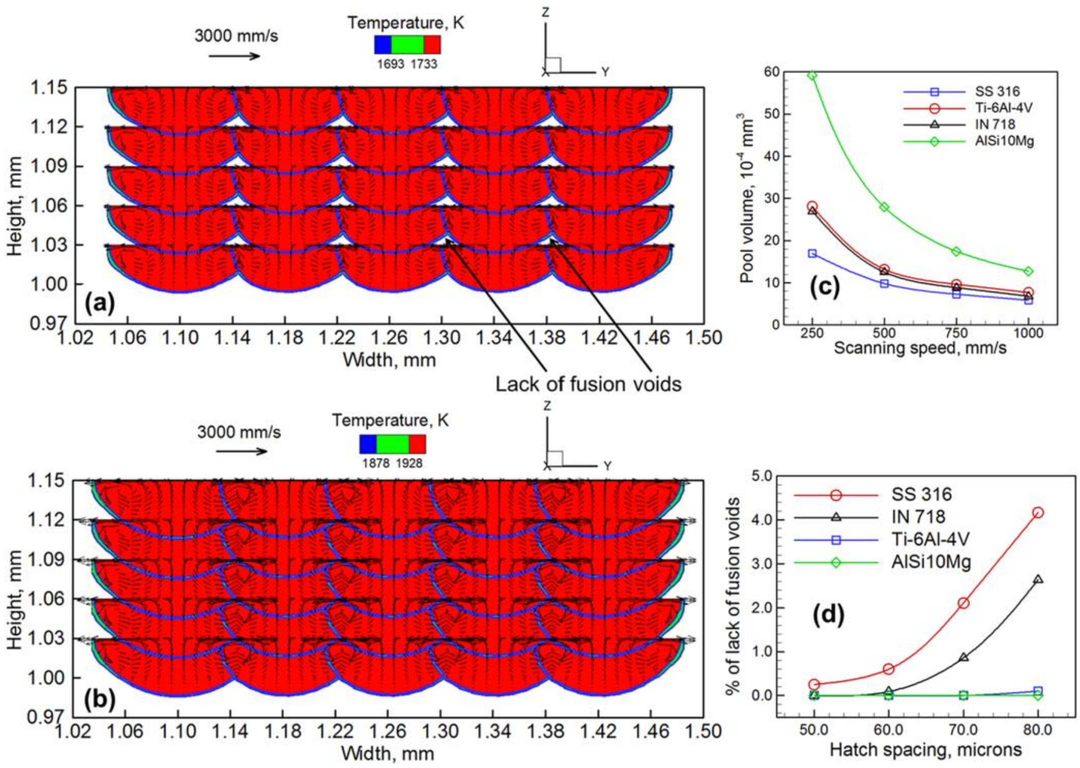

Fig. 2.24. Transverse sectional view of the molten pools for 5 layers 5 hatches build of (a) SS316, and (b) Ti-6Al-4V build using 1000 mm/s scanning speed and 80 µm hatch spacing. (c) Variation of lack of fusion ratio with hatch spacing for 5 layers 5 hatches build of four alloys using 1000 mm/s scanning speed. (d) Variation of volume percent of porosity with non-dimensional heat input[93].

Fig. 2.23 illustrates how varying hatch spacing influences inter-track porosity during the LPBF of Ti-6Al-4V [92]. Excessively large hatch spacings (e.g., 100 µm) can lead to insufficient overlap, resulting in inadequate heat input and incomplete fusion in the overlap zones. The instability of the melt pool under such conditions causes variability in the track width and penetration depth, thereby exacerbating porosity and fusion issues. Fig. 2.24 demonstrates how such lack of fusion defects correlate with reduced melt pool dimensions. Advanced computational models incorporating thermal, mass, and momentum transport have shown that the optimal hatch spacing and layer thickness are material-dependent, driven by differences in thermophysical properties that affect fusion zone geometry [93]. Fig. 2.25 further demonstrates how porosity varies across a range of energy densities:

- At low energy densities (Fig. 2.25a), lack of fusion voids dominate due to incomplete melting;
- At optimal energy densities (Fig. 2.25b), defect-free tracks are produced;
- At excessive energy densities (Fig. 2.25c), keyhole-induced porosity emerges due to deep vapor cavities formed by intense laser-material interaction.

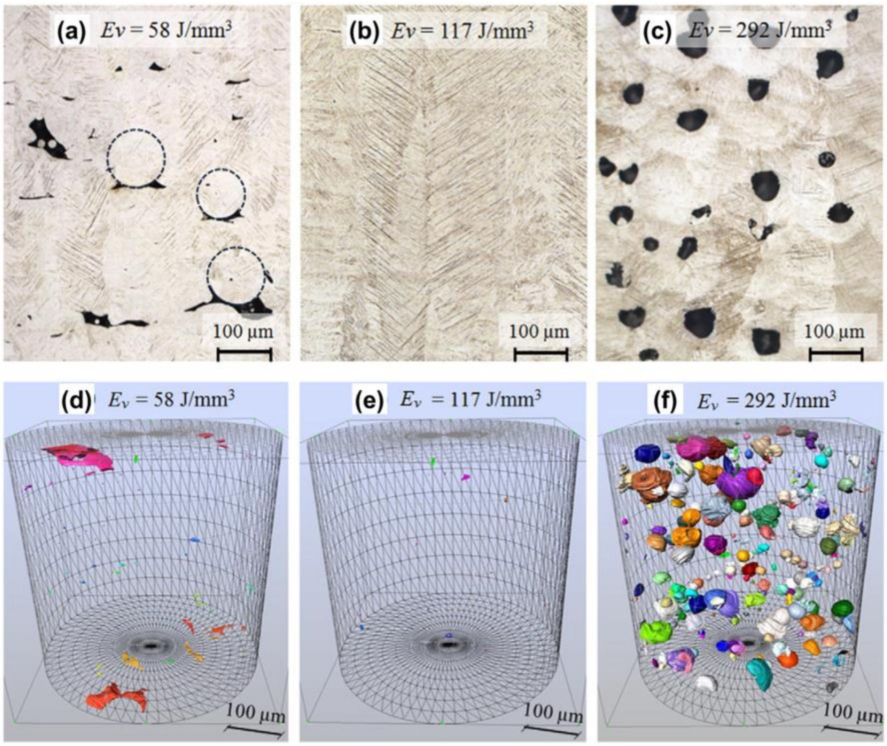

Fig. 2.25. Porosity as a function of energy density for PBF-L of Ti-6Al-4V: (a)–(c) Characterized by light optical microscopy, (d)–(f) Characterized by synchrotron tomography[63].

This behavior is corroborated in Fig. 2.26(a) and (b), where porosity volume fraction varies significantly with laser power and scan speed [63]. To mitigate pore formation at scan path turning points, Martin et al. [94] introduced a dynamic process control strategy to maintain a near-constant energy density, thereby improving melt track consistency and reducing defect generation, as shown in Fig. 2.27. Additionally, a study on LPBF-fabricated 8620 low-alloy steel [95] demonstrated that optimizing laser energy input to 88.89 J/mm³ achieved a maximum relative density of 99.67% and ultimate tensile strength of 1.18 GPa. These results further highlight the importance of precise energy input control to improve densification and mechanical performance.

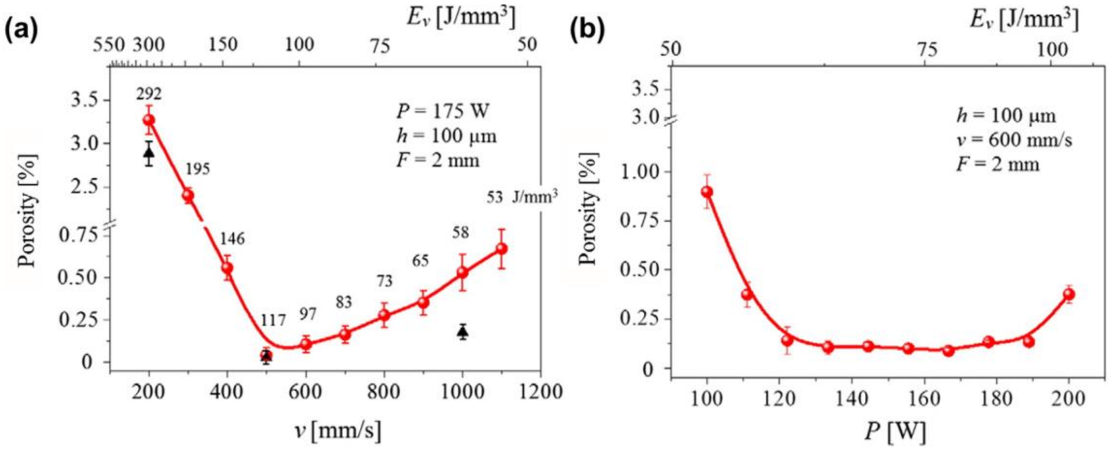

Fig. 2.26. Variation of porosity during LPBF of Ti-6Al-4V as functions (a) of scanning speed, (b) laser power[63].

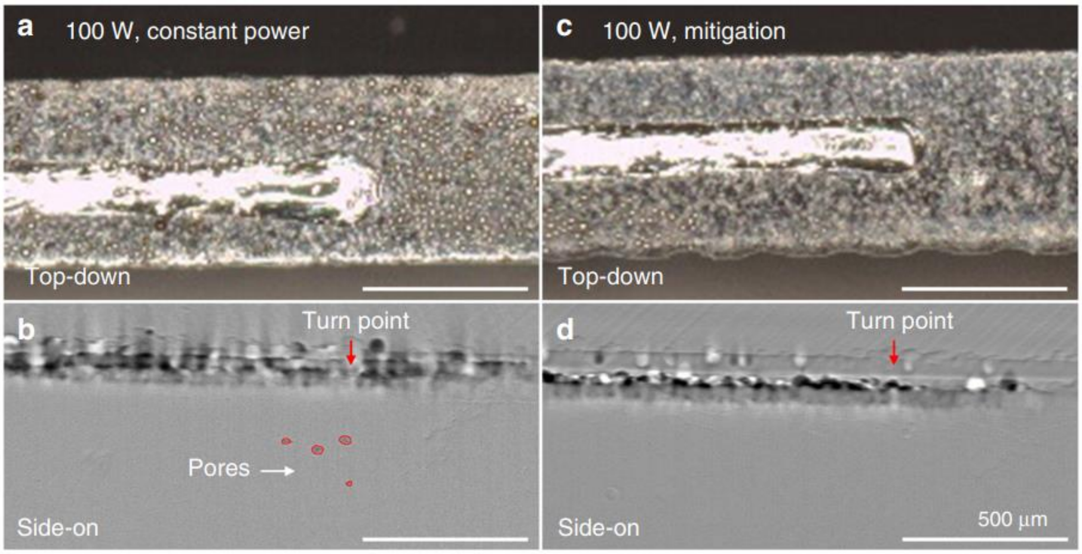

Fig. 2.27. Quality of LPBF-AM tracks in Ti-6Al-4V[94].

In summary, laser energy density serves as a comprehensive metric reflecting the interplay among critical process parameters. It provides a valuable basis for optimizing laser power, scanning speed, hatch spacing, and layer thickness to minimize defect formation and enhance the structural performance and manufacturing efficiency of

LPBF-fabricated components.

2.4.2 Effect of scan strategy

The scan strategy plays a crucial role in determining the thermal history and molten pool dynamics during the LPBF process. It directly influences heat transfer behavior, fluid flow patterns, and solidification conditions, thereby affecting the formation, location, and distribution of defects such as porosity, lack of fusion, residual stress, and distortion. Different scan patterns lead to variations in the thermal gradients and cooling rates, which in turn govern microstructure evolution and defect accumulation. Therefore, the selection and optimization of scan strategy are essential for achieving uniform energy distribution, enhancing interlayer bonding, and minimizing defects in additively manufactured components.

In general, three main scan strategies are commonly used in LPBF: zigzag, unidirectional, and cross-hatching, as illustrated in Fig. 2.28 [88]. In zigzag and unidirectional strategies, the laser power is often unstable at the beginning and end of each scan track, and scan speed may fluctuate, leading to uneven energy input and promoting defect formation [96][97]. Impurities in the powder may also accumulate at the track ends during densification, increasing defect density. Partial fusion defects are particularly common between adjacent tracks and layers due to inadequate remelting and poor overlap [98][99]. In contrast, the cross-hatching strategy, which rotates scan vectors between successive layers, distributes the energy input more evenly and helps mitigate defect accumulation across the build.

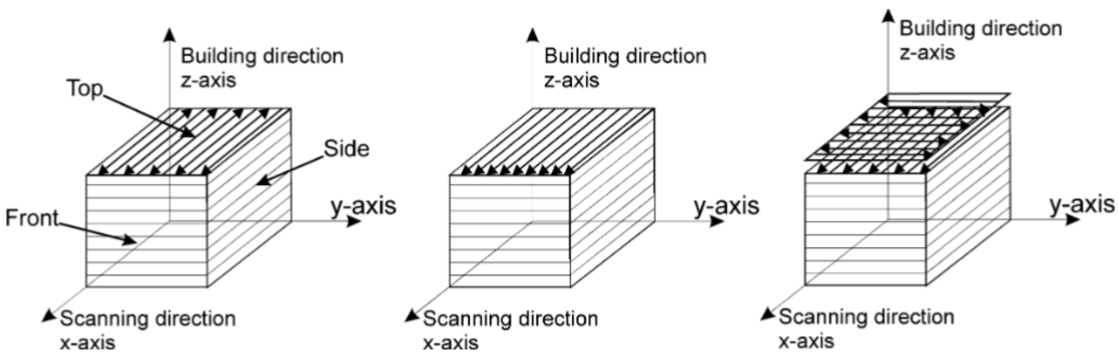

Fig. 2.28. Three different scan strategies: “unidirectional” (left), “zigzag” (center), and “cross-hatching” (right)[88].

Another widely used method is the island scan strategy, as shown in Fig. 2.29 [56]. In this approach, each layer is divided into smaller regions (islands), scanned in a randomized sequence, and shifted in subsequent layers to avoid thermal accumulation in the same location. This helps to balance residual thermal stresses and suppress crack formation. However, defects may still occur near the edges of islands due to inconsistent energy input and variable scan directions.

To reduce defect formation in the overlapping zones, interlayer staggering and orthogonal scan strategies have been proposed. Yang et al. [100][101] demonstrated that remelting overlap regions using orthogonal scanning improves fusion quality and reduces porosity. Parry et al. [10] employed a thermo-mechanical model to investigate stress development under different scan strategies and found that residual stress aligned with the scan direction dominates, resulting in anisotropic stress fields.

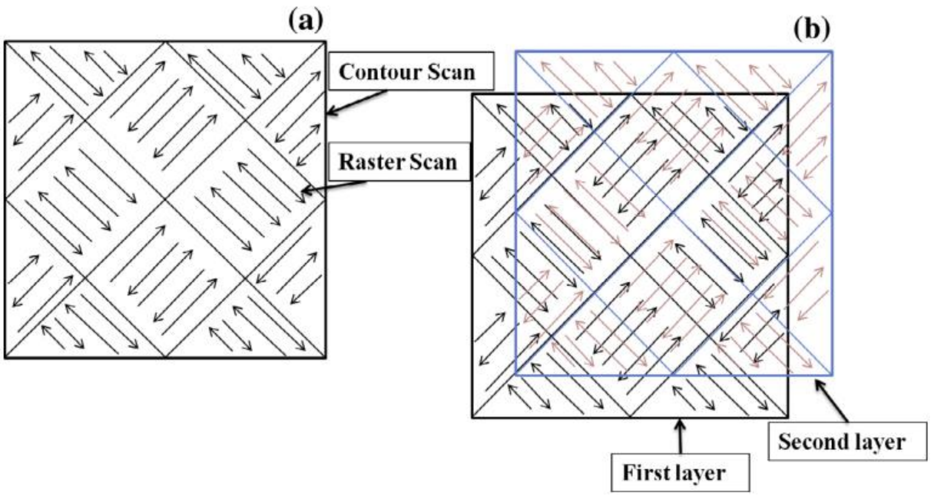

Fig. 2.29.Schematic illustration of the island scan strategy, (a) each layer is divided into islands and raster scanned; (b) the successive layers are displaced in 1 mm[56].

Recent studies on aluminum-lithium alloys further highlight the importance of scan path design, as shown in Fig. 2.30. In particular, processing of 2195 Al-Li alloy under various scan strategies revealed that a linear scan pattern minimized gas pore and crack densities, achieving a high densification rate of 98.6%. It also produced smaller grains (average 19.7 μm), a lower fraction of high-angle grain boundaries (57.4%), and a higher texture index. The linear strategy's concise thermal history and rapid cooling contributed to superior tensile properties (315.03 MPa strength and 5.03% elongation) [102]. These findings underscore the crucial role of scan strategy optimization in tailoring microstructure and mechanical performance in LPBF-processed lightweight alloys.

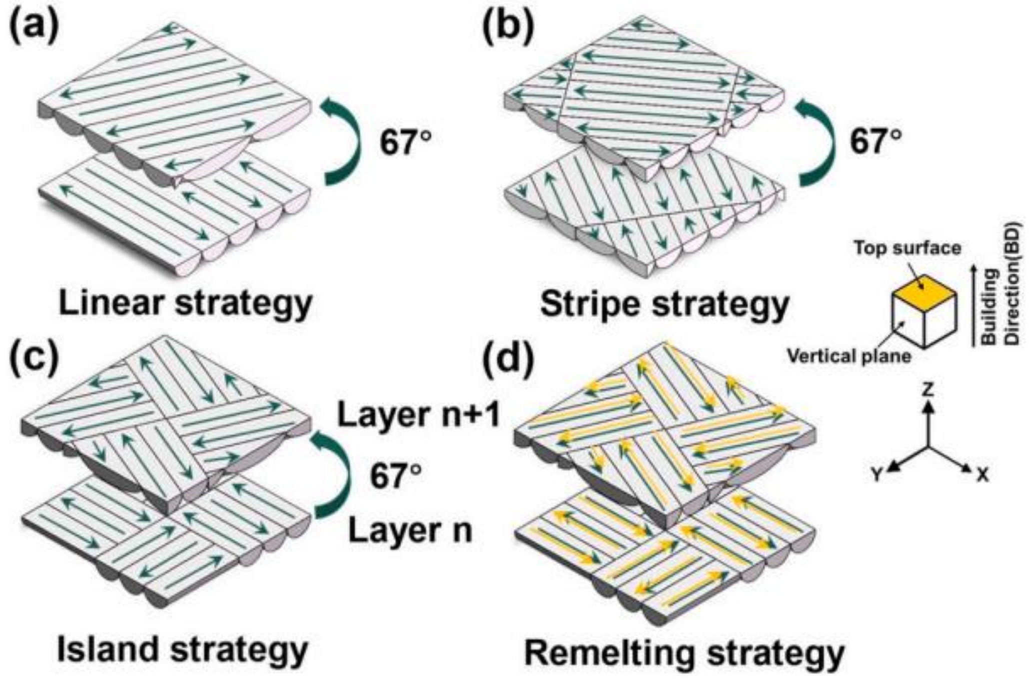

Fig. 2.30 Schematic diagram of different scanning strategies [102].

2.5 Flow and heat transfer mechanism during LPBF process

In the LPBF process, a high-energy laser beam rapidly and selectively melts metal powders along a predefined scanning path. The laser scan speed is extremely high-typically on the order of several hundred millimeters per second [103], and in some cases, it can reach up to 4.5 m/s [104]. As illustrated in Fig. 2.31, the resulting energy transfer and phase transition processes are both rapid and highly complex [105]. These include intense thermal convection within the molten pool, heat conduction between adjacent powder particles, material melting and solidification, vaporization effects, microstructural evolution, and even oxidation reactions in certain conditions. A comprehensive understanding of these coupled flow and heat transfer phenomena is critical for establishing more reliable control over the process. This knowledge forms the foundation for optimizing process parameters, reducing defect formation, and improving the mechanical performance and consistency of fabricated components.

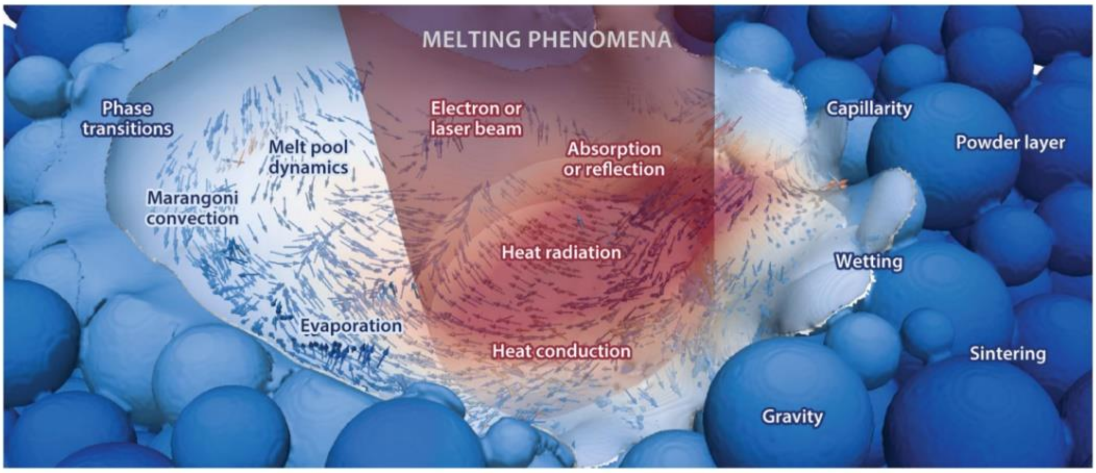

Fig. 2.31. Main physical processes in melt pool region during LPBF [105].

2.5.1 Temperature fields

During the LPBF process, the metal powder in the powder bed is rapidly heated by the laser beam, initiating melting once the local temperature exceeds the material's melting point. As the laser moves along its scanning path, the previously melted region is no longer exposed to direct energy input, leading to a rapid temperature drop driven by heat conduction, convection, radiation, and latent heat release during solidification. When the temperature falls below the melting point, the molten material resolidifies. Accurately capturing the temperature field—including both the spatial distribution and temporal evolution of temperature—is essential for understanding the thermal history of the process. This thermal history plays a critical role in determining microstructure evolution, residual stress formation, and the development of internal defects. Therefore, precise knowledge of the temperature fields is fundamental for controlling part quality, optimizing process parameters, and ultimately enabling defect mitigation and tailored microstructural control.

The LPBF temperature field has the characteristics of significant heating and cooling rate, large temperature gradient, and high peak temperature. These characteristics bring many challenges to temperature measurement. Due to the fast heating and cooling speed, the signal acquisition rate of the temperature measuring element needs to be high enough to measure the temperature change during the entire heating and cooling process; since the local temperature of the molten pool will reach a high temperature of more than 2000K, even higher than the boiling point of the metal, the traditional method is adopted. The thermocouple method cannot measure the molten pool temperature. Therefore, the measurement of LPBF process temperature mainly adopts non-contact temperature measurement methods such as infrared thermometers and uses simulation methods as auxiliary methods. Zhinov et al. [106] established a finite element model of the LPBF temperature field based on titanium alloys and measured the molten pool using an infrared thermometer, as shown in Fig. 2.32. However, because it is difficult to obtain accurate surface emissivity, the measurement results are only represented by the signal strength of the infrared thermometer, and the precise temperature cannot be measured. Dunbar et al. [107] placed the data acquisition device in a metal iron box designed by themselves at the lower part of the substrate and measured the substrate temperature during LPBF processing of different materials using a K-type thermocouple spot welded on the substrate outside the molding area, as shown in Fig. 2.33. Roberts et al. [108]studied the evolution of the temperature field during the LPBF forming process, which shows that the peak temperature of the molten pool increases with the increase of the number of layers. Gusarov et al. [109][110][111] simulated the temperature field distribution of 316L stainless steel during LPBF processing, and the results showed that the scanning speed, powder layer thickness, and thermal properties of the material have essential effects on the LPBF temperature field. Hooper [112]developed a high-speed, coaxial two-wavelength imaging method to measure melt pool surface temperatures in LPBF with high spatial (20 μm) and temporal (100 kHz) resolution. Their approach provides detailed insights into thermal gradients and cooling rates, enabling better optimization of scan strategies and parameters to control defect formation and microstructure evolution by managing the temperature field.

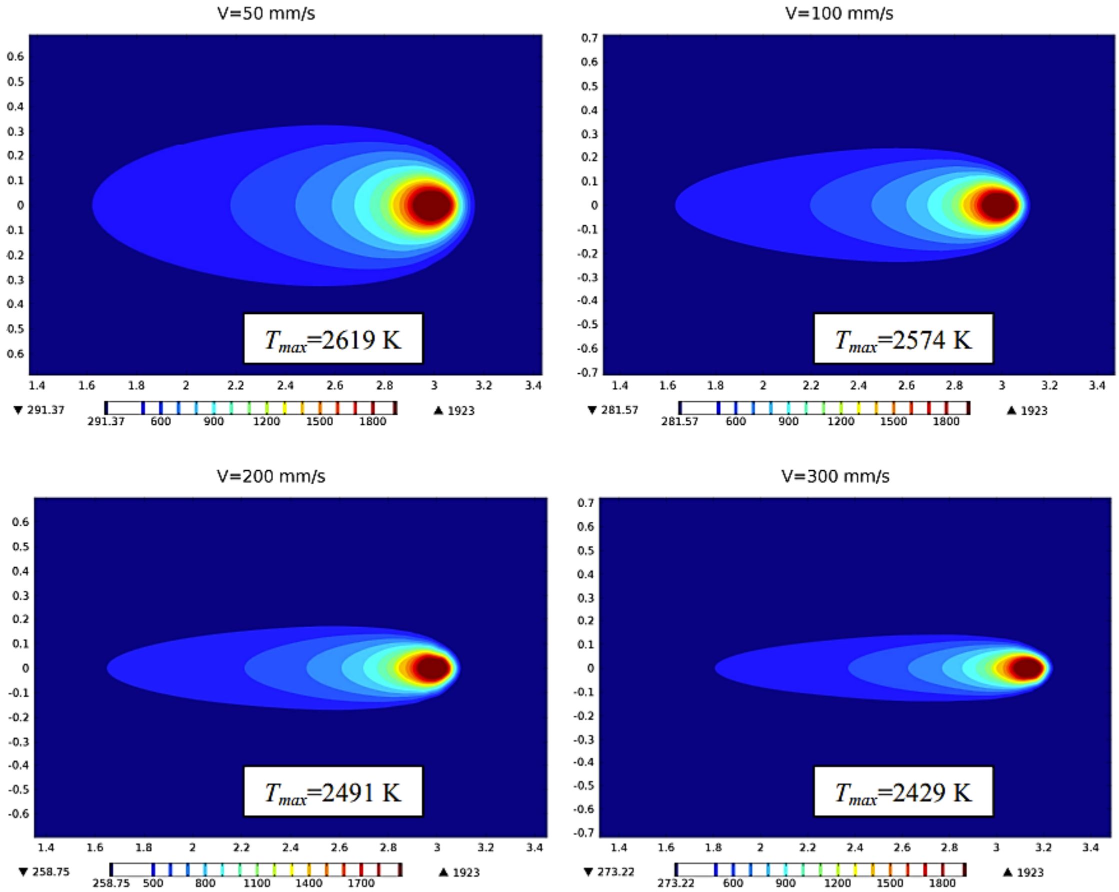

Fig. 2.32. Numerical simulation of temperature fields under 90W laser power during laser scanning of Ti6Al4V substrate[105].

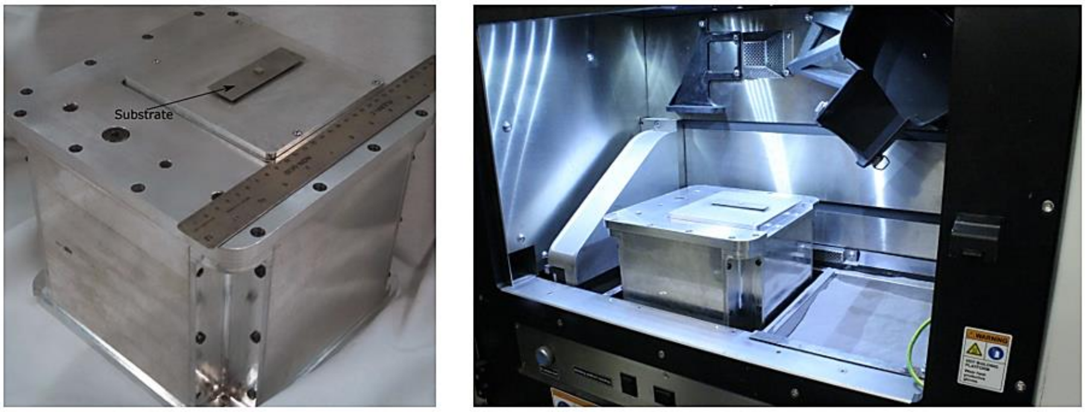

Fig. 2.33. The vault experimental enclosure designed for measurements in LPBF machines[106].

Parts manufactured by LPBF usually have high residual stress, which is greatly affected by the temperature field. Roberts et al. [108] used the finite element method to calculate the temperature field distribution near the laser spot during the LPBF process and pointed out that the excessively high-temperature gradient of the metal near the laser spot would adversely affect the thermal stress distribution and residual stress states. Dai et al. [113] constructed temperature field and stress field models by finite element analysis method, studied the influence of different scanning strategies on residual thermal stress and deformation and found that transient thermal stress is essential for deformation. Parry et al. [10] used the finite element simulation software marc to build an LPBF-forming thermodynamic coupling model, as shown in Fig. 2.34. By performing finite element simulations on single-channel scanning and serpentine scanning, they found that temperature gradient was the main factor in generating residual stress and analyzed the stress distribution and variation of the two scanning methods. And it is found that the workpiece has the most significant stress parallel to the scanning direction.

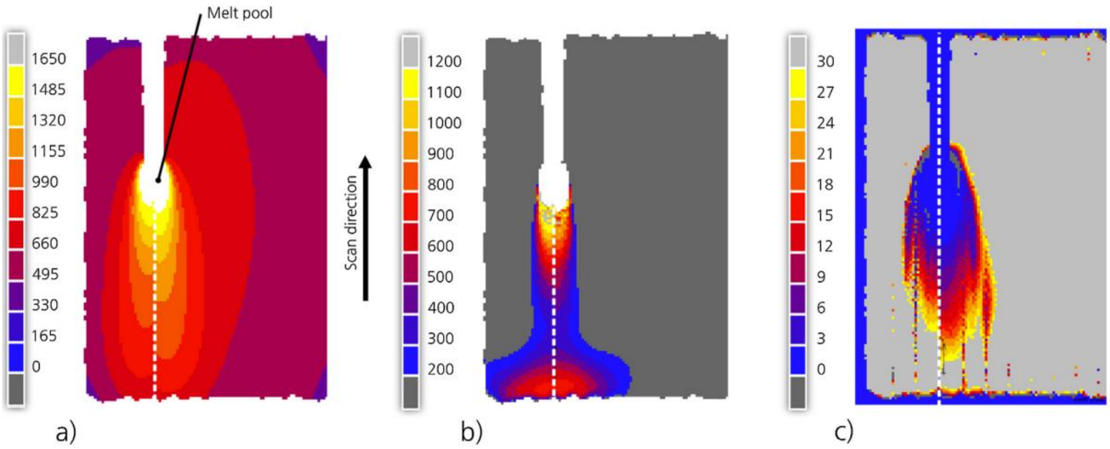

Fig. 2.34. Mirrored profile views of (a) the temperature, (b) the temperature gradient in the Y direction, and (c) σ_{yy} taken at t = 0.0320 s (left half) and at t = 0.156s (right half) [10].

Some researchers control and eliminate defects by controlling the temperature field. Devesse et al. [114] used a hyperspectral camera online to detect the temperature distribution of the molten pool by the laser and adjusted the laser power in real-time through the linear state feedback and PI control of the molten pool temperature to keep the temperature and width of the molten pool stable. Craeghs et al. [115] used a high-speed near-infrared CMOS camera and a photodiode sensor to detect the size of the molten pool in LPBF online and feedback to adjust the laser power to maintain the stability of the molten pool temperature and improve the forming quality of the part. Miyagi et al. [116] used three photodiodes to detect the thermal radiation signal of the molten pool online. They developed an adaptive shape control system to establish the corresponding relationship between the intensity of the thermal radiation signal and the width of the molten pool and use this to adjust the laser power and maintain stability for the size of the molten pool. Recently, Li et al. [117] proposed a multi-view melt pool temperature monitoring method based on a light field camera. By calibrating spectral responses and applying dual-wavelength theory, they achieved high-accuracy temperature measurements with maximum errors below 3%, providing an effective real-time thermal monitoring solution for laser direct energy deposition (LDED) and the LPBF processes. This approach offers great potential for future control and elimination of defects by precisely managing the temperature field during manufacturing.

2.5.2 Fluid dynamics during molten pool process

When a high-energy laser irradiates the powder bed in the LPBF process, localized melting occurs, forming a transient molten pool. Within this molten region, complex fluid dynamics arise, primarily driven by thermal convection induced by surface tension gradients (Marangoni effect) and temperature gradients. As the local temperature exceeds the evaporation threshold, intense vaporization of the molten metal generates a recoil pressure on the melt surface, resulting in high-speed downward flow and significant melt pool perturbation. This recoil pressure also induces turbulent gas flow in the surrounding atmosphere, leading to powder spattering and denudation effects. Upon cessation of laser irradiation, the molten pool undergoes rapid cooling and solidification, often accompanied by the formation of defects such as porosity, keyholes, and lack-of-fusion zones. Therefore, a comprehensive understanding of the fluid flow behavior within the molten pool is essential for stabilizing melt dynamics, minimizing defect formation, and optimizing process parameters to achieve consistent part quality in LPBF.

Since the actual melt pool process occurs at the micron scale and experimental observation methods are limited, many researchers use a combination of experiments and simulations to study the fluid dynamics of the molten pool. Cunningham et al. [57] observed the keyhole phenomena in the molten pool using ultrahigh-speed synchrotron x-ray imaging and discovered a crucial value that changed from conduction mode to keyhole when the power density changed. In addition, the tangent of the front keyhole wall angle and keyhole depth have a linear connection. Martin et al. [94] used in situ X-ray imaging and multi-physics simulations to investigate pore formation and liquid-solid interface dynamics throughout the LPBF process. Pores emerge when the laser scan velocity changes because deep keyhole depressions in the surface form quickly and subsequently collapse, trapping inert shielding gas in the solidifying metal. Huang et al. [118] revealed quasi-stable, transition, and unstable keyhole regimes under different laser scan velocities, where the rear keyhole wall (RKW) collapses in the transition regime and keyhole bottom collapse in the unstable regime can cause the pore formation, as shown in Fig. 2.35. Zhao et al. [60] employed high-speed x-ray imaging to investigate pore formation in Ti-6Al-4V produced by a critical instability at the keyhole tip, demonstrating that the critical keyhole instability generates acoustic waves in the melt pool, which drives the pores near the keyhole tip to travel away from the keyhole and get trapped as defects., as shown in Fig. 2.36. To simulate the keyhole pore formation process, Wang et al. [119] used a multiphysics thermal fluid flow model including heat transfer, liquid flow, metal evaporation, the Marangoni effect, and Darcy's law, and the findings were confirmed using experimental results. The simulation of the keyhole pore formation in the molten pool from 0 μs to 10 μs in Fig. 2.37 corresponds to the process from 0 μs to 7.36 μs experimentally observed in Fig. 2.36. With the help of simulation, they analyzed the velocity field in the molten pool using simulation to explain the keyhole pore formation process and discovered that keyhole instability and motion of the instant bubble pinning on the solidification front cause instant bubble formation. Leung et al. [120] used in situ and operando X-ray imaging to explore the impact of powder oxidation on molten pool dynamics and defect formation. The result shows that entrained powder oxide will change the Marangoni convection from an inward centrifugal to an outward centripetal flow, promoting pore nucleation, stability, and growth. Also, during laser re-melting, pores near the track surface might burst, resulting in droplet spatter and an open pore or pore healing via Marangoni flow. Hojjatzadeh et al. [121] proposed that the pore movement behavior is driven by competition between the temperature gradient produced thermocapillary force and the melt flow-induced drag force by combining in situ high-speed, high-resolution synchrotron x-ray imaging measurements with multi-physics modeling. Furthermore, the significant thermocapillary force caused by the high-temperature gradient in the laser contact zone can quickly remove pores from the melt pool. To stabilize the melt pool dynamics and minimize defects, Khairallah et al. [39] they derived criteria and adopted a proportional-integral-derivative (PID) controller in the simulation to vary the power dynamically, helping improve build reliability. Fan et al. [122] investigated the underlying mechanisms of keyhole instability in laser powder bed fusion (LPBF) and laser welding processes using high-speed synchrotron X-ray imaging. Their study revealed that the formation of protrusions on the rear wall of the keyhole, driven by internal melt pool vortices, plays a critical role in initiating keyhole collapse and subsequent porosity. To suppress this instability, a transverse magnetic field was introduced, which induced a secondary thermoelectric magnetohydrodynamic (TEMHD) flow. This flow effectively modified the primary vortex structure, reducing keyhole oscillations and stabilizing the melt pool. The effectiveness of this magnetic stabilization was shown to depend strongly on the relative orientation between the scanning direction and the magnetic field, due to the directional nature of the Seebeck effect–induced Lorentz forces. For high-silicon aluminum alloys such as AlSi10Mg, the application of a 0.5 T magnetic field during right-to-left scanning resulted in an 81% reduction in porosity. A dimensionless force analysis indicated that while conventional electromagnetic damping is insufficient at LPBF scales and low field strengths, the thermoelectric effect becomes dominant in alloys with high Seebeck coefficients. This work provides a mechanistic framework for magnetic field–assisted stabilization of the melt pool, offering guidance for broader application in advanced materials and additive manufacturing processes.

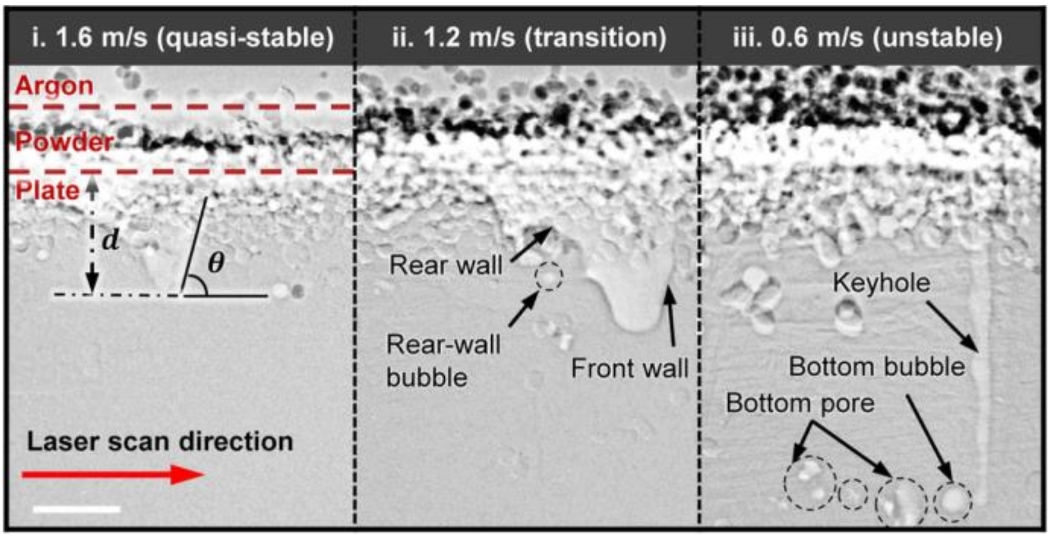

Fig. 2.35. Keyhole collapse mechanism and related keyhole melting regime transitions[116].

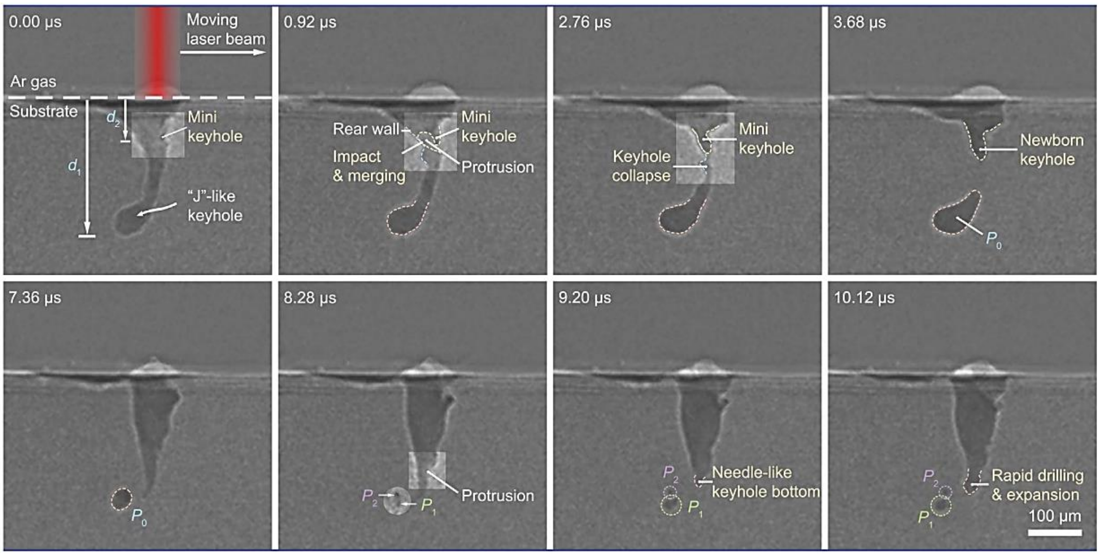

Fig. 2.36. The keyhole pore formation and motion driven by acoustic waves from keyhole instability [60].

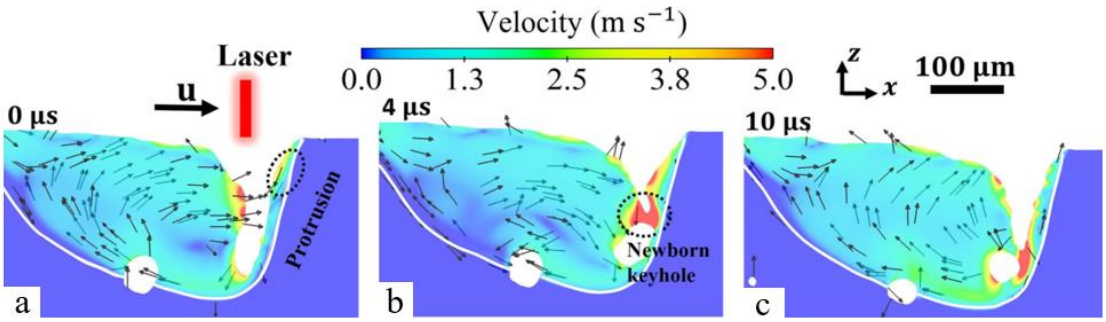

Fig. 2.37. Instant bubble formation due to the keyhole instability[119].

Also, several researchers have studied fluid dynamics around the molten pool induced by the high-velocity recoil metal vapor under the vaporization of molten pool liquid. Bidare et al. [41] utilized the technique of high speed schlieren imaging to visualize the laser plume and the heated atmosphere with refractive index gradients above the molten pool during LPBF, as shown in Fig. 2.38. The convection fronts that start from the molten pool's surface spread through the atmosphere above the deposit, transferring heat and momentum from the vapor jet to the atmosphere. The pressure and velocity of the induced gas flow, the local locations and traveling directions of the powder particles and surrounding geometric limits on the powder particles are the major determinants of entrained particle movement. By linking the DEM and FVM, Chen et al. [123] built a multiphase flow model that accounts for momentum and heat transfer between the gas phase and powder particles. The result shows that the spattering phenomenon is a combination action of the jetting vapor and its produced vortex flow of ambient gas, in which some of the particles entrained by the ambient gas flow are then expelled by the vapor jet. Also, the vortex flow of the ambient gas causes denudation because particles near the vapor jet are entrained inward. Matthews et al. [6] proposed the Knudsen number (Kn) as the criterion for the competition between metal vapor jet and induced argon gas flow under different ambient gas pressure, as shown in Fig. 2.39. They found that drag force on the particles due to the shear flow slows down with decreasing gas density and, at some pressure, the particle motion reverses, making the denudation zone's width minimum. Guo et al. [50] suggested that the powder spattering behavior influenced by the ambient pressure controls the divergence angle of the vapor jet and the argon gas flow, as shown in Fig. 2.40. With the increase of ambient pressure, the total amount of spattering (both cold and hot) decreases, dominated by the divergence angle, while the amount of thermal spattering increases, dominated by the entrainment caused by the argon gas flow. Also, the acceleration and driving force of vapor-driven particles are roughly one order of magnitude more than argon gas flow-driven particles, and their moving speed is three times that of argon gas flow-driven particles. In addition, powder spattering mitigation is proposed, such as pre-sintering the powder bed, adjusting layer thickness, and adjusting environment pressure. Li et al. [124] established the first fully coupled 3D multiphysics model for LPBF, enabling quantitative simulation of melt pool dynamics, depression zone formation, gas flow characteristics, and powder motion under various ambient pressures. The study revealed that although the overall gas flow structure remains similar, key flow parameters-such as temperature, velocity, Reynolds number, and Knudsen number-vary significantly with pressure. They further defined four powder-gas interaction modes (recoil, entrainment, elevation, and expulsion), whose combined effects govern powder behavior and offer insights for mitigating powder spattering. Yuan et al. [125] developed a coupled CFD-DEM multiphase model to investigate the complex melt-gas-powder interactions in LPBF under varying laser scan speeds. The study revealed a two-phase evolution of metal vapor behavior and established a correlation between scan speed and vapor flow angle. Notably, three types of oscillatory phenomena were identified-localized pressure fluctuations on keyhole walls, counter-rotating argon vortices, and unsteady drag forces on powder particles-all contributing to different spatter mechanisms. These insights enhance the understanding of dynamic instabilities and provide guidance for process optimization and control. Zhang et al. [126] developed a high-fidelity multi-physics simulation framework by coupling CFD, DEM, and CALPHAD models to simultaneously capture the gas flow, melt pool behavior, and particle dynamics in both single- and multi-material LPBF processes. Validated by experiments, the model reveals that defect formation is closely linked to powder spattering and entrainment. Specifically, the coalescence of hot spatters leads to large agglomerations, which can cause lack-of-fusion and porosity defects through collapse of the depression zone. In multi-material systems, unmelted entrained particles-due to insufficient melt temperature-can result in particle inclusion defects. Moreover, the momentum of entrained particles at the melt pool tail can disturb the flow symmetry, potentially altering local element distribution. Based on these findings, the authors propose a defect generation criterion that offers guidance for in-situ defect detection and process control, aiming to enhance the consistency and reliability of LPBF-manufactured parts.

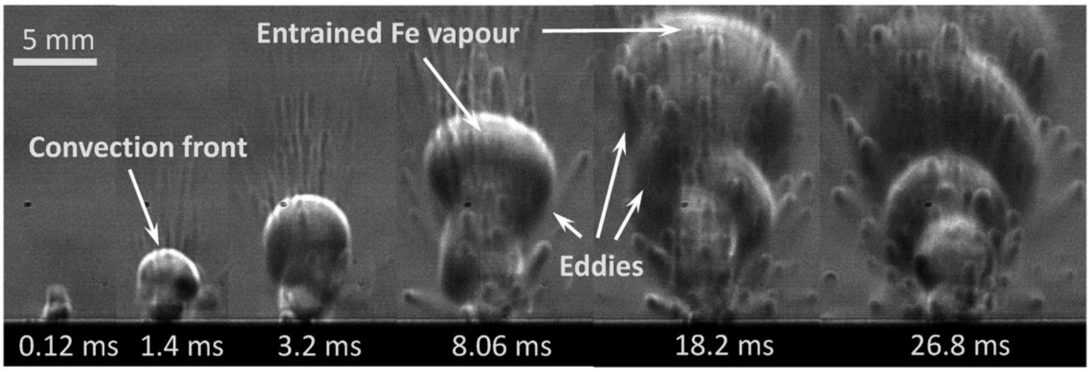

Fig. 2.38. Composite image of the heated gas rising due to convection at the times indicated for laser power 100 W and scan speed 0.5 m/s towards the viewing direction. Radial momentum is imparted to the atmosphere by eddies trailing the convection fronts[41].

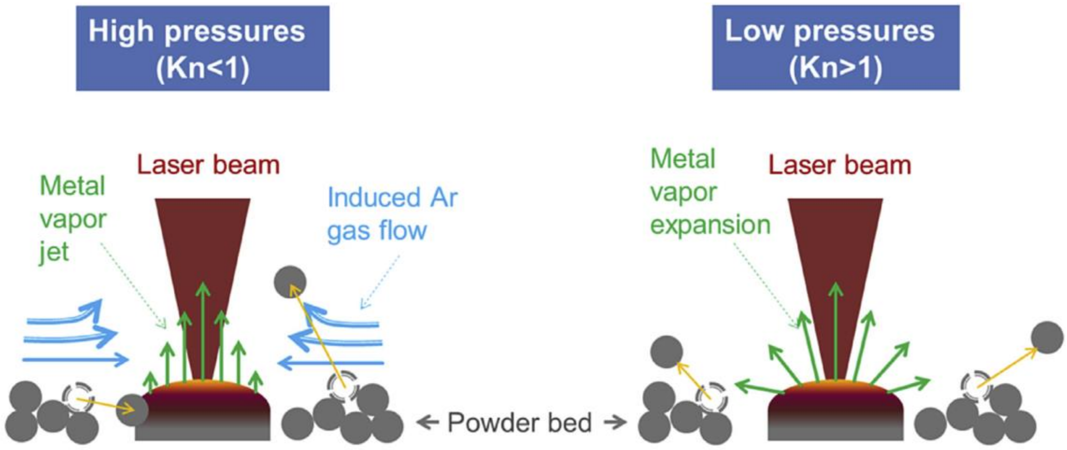

Fig. 2.39. Schematic depicting the action of evaporated metal flux on the flow pattern of the surrounding Ar gas and displacement of particles in the powder bed[6].

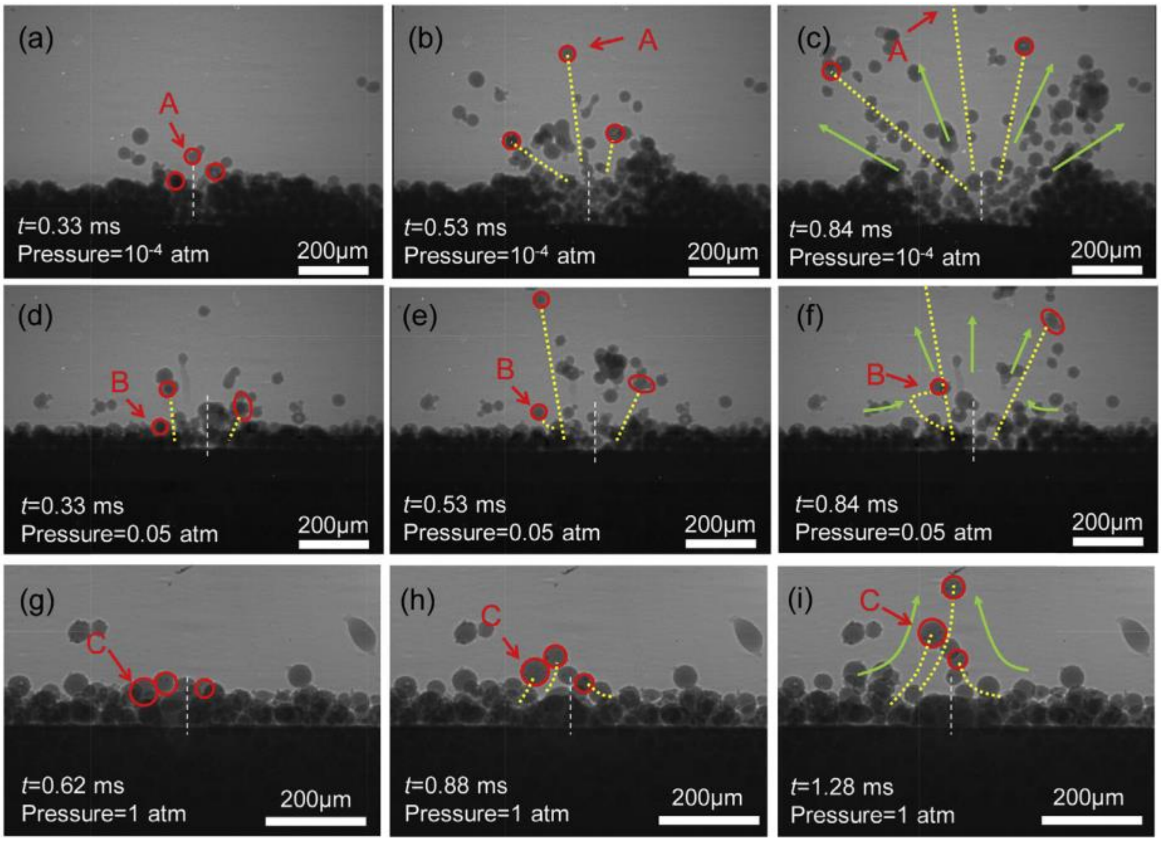

Fig. 2.40. Dynamic x-ray images showing powder motion at different moments and under different environment pressures[50].

2.6 Research objectives

During the LPBF process, the evolution of melt pool morphology plays a fundamental role in determining thermal-fluid behavior and directly governs the formation and development of various defects. Dynamic thermal imbalance within the melt pool may cause severe vaporization, which leads to melt pool instability and facilitates the formation of defects such as pores, lack of fusion, and cracks. Among these, spattering is particularly critical, as it not only reflects melt pool instability but also acts as a trigger for a chain of detrimental effects. For instance, spattered particles may block the laser beam and disrupt energy input, re-enter the melt pool and introduce turbulence that generates porosity [39][127], or interfere with powder spreading, resulting in lack of fusion or gas-induced porosity in subsequent layers [7][12][47][54]. In addition, solidification cracks can form due to poor bonding around voids caused by spatter re-deposition [128]. However, current research presents two key limitations:
(1) Most studies treat the melt pool temperature field as a singular indicator of thermal behavior, without fully characterizing the comprehensive heat transfer mechanisms between the melt pool and solid substrate. Additionally, many investigations focus solely on fluid dynamics, neglecting the interdependence between heat transfer and flow, which together drive defect formation.
(2) Studies on spattering mechanisms largely remain qualitative and descriptive, lacking a rigorous quantitative understanding of how specific process parameters govern spattering behaviors.

In response, this research aims to address the above gaps through a combined experimental and numerical approach. The primary research objectives are:

1. **To establish a high-fidelity numerical model coupled with experimental validation.**

- Investigate the Laser powder bed fusion of 316L stainless steel powder under varying laser power and scanning speed using single-layer, multi-track experiments.

- Analyze and characterize melt track morphology under different process parameters.
- Develop a multiphysics model to study heat transfer and melt flow dynamics in the melt pool and validate it against experimental results.

2. **To explore the defect formation mechanisms within the melt pool and the effect of process parameters.**

- Clarify how process parameters affect melt pool morphology and defect generation.
- Reveal the coupling between thermal and fluid dynamic mechanisms that drive defect formation.
- Optimize process parameters to suppress defects and achieve high-quality part formation.

3. **To investigate the spattering mechanism and the influence of process parameters.**

- Examine the effect of process parameters on spattering behavior, including spatter quantity, size, and velocity.
- Analyze the particle dynamics under vapor and gas flow forces.
- Establish the relationship between particle dynamics and spatter generation, enabling the prediction of spattering outcomes and providing guidance for process optimization.

Chapter 3. Multi-physics modeling of LPBF

3.1 Introduction

LPBF is an advanced additive manufacturing technique that utilizes a high-energy laser beam to selectively melt metal powders layer by layer, enabling the fabrication of complex geometries with high precision. The LPBF process involves a series of intricate physical and chemical phenomena that collectively govern the evolution of microstructure and mechanical properties in the final components. Upon laser irradiation, thermal energy rapidly propagates via conduction, causing a significant localized temperature rise. Within the melt pool, the presence of substantial temperature and surface tension gradients induces thermocapillary convection, commonly known as the Marangoni effect, which plays a crucial role in shaping the melt pool morphology and governing its dynamic behavior. Under high-energy input, metal powders transition into a transient liquid state, which subsequently solidifies upon rapid cooling, ultimately determining the microstructural characteristics and mechanical performance of the fabricated part. When the local temperature exceeds the material's vaporization threshold, evaporation occurs, generating metal vapor and potentially triggering plasma formation. Additionally, the LPBF process may involve material oxidation[129]-[132], high-temperature decomposition of alloying elements[133], spattering of molten metal and powder particles, and the formation of porosity, all of which can significantly impact the build quality and structural integrity of the manufactured component[134].

However, due to the extremely short timescale and the complex multi-physics interactions governing the process, conventional experimental approaches alone are insufficient for real-time observation and in-depth analysis of these transient phenomena. Consequently, numerical simulation has emerged as an essential tool for investigating key aspects such as the interaction between powder particles and the recoating blade during powder spreading, the heat and fluid flow dynamics within the melt pool, and the multiphase interactions between powder particles and the metal vapor plume[135]. These computational approaches are critical for optimizing process parameters and improving part quality. This chapter systematically outlines the modeling methodologies employed for simulating the powder spreading process, the thermal-fluid behavior of the melt pool, and the multiphase dynamics between powder particles and vapor plume, providing a comprehensive framework for numerical analysis in LPBF.

3.2 Discrete Element Method (DEM)-Based Laying Powder Model

In the LPBF additive manufacturing process, powder bed formation serves as a critical step that directly influences the metallurgical quality of the final components[136]. This process involves the uniform spreading of micro-scale metal powders onto a substrate or previously solidified layers using a metallic recoater blade, followed by selective laser scanning to achieve metallurgical bonding and interlayer remelting. Studies have shown that the packing density distribution and geometric homogeneity of the powder bed significantly affect the thermodynamic behavior of the melt pool and the evolution of microstructures[137][138]. These factors are fundamental in determining the final part's densification and mechanical properties.

The quality of powder bed formation is governed by the multiphysics interactions among the kinematic parameters of the recoater (velocity field distribution), the geometric characteristics of the blade (cutting-edge curvature radius, surface roughness), and the process parameters (layer thickness settings). Due to the microscale effects inherent in the powder system and the discrete nature of the medium, conventional finite element analysis (FEM) and computational fluid dynamics (CFD) methods—based on continuum mechanics assumptions—struggle to accurately capture the mechanical behavior at the powder-recoater interface and the interparticle interactions[136].

In recent years, the Discrete Element Method (DEM), rooted in discontinuous media mechanics, has emerged as a powerful numerical approach for simulating the dynamic response of particulate systems. The Discrete Element Method (DEM) was first introduced by Cundall [139] in the 1970s as a computational approach to solving complex dynamic problems, particularly in the study of rock particle motion. By 1974, the DEM framework had matured, incorporating interactive graphical output capabilities, which significantly expanded its applicability in various engineering domains. With advancements in computational power and numerical simulation techniques, DEM has been widely adopted across multiple scientific disciplines. More recently, it has been extended to the mesoscale numerical simulation of the LPBF process, offering a novel computational paradigm for investigating powder bed formation mechanisms and melt pool dynamics [140]-[142].

The discrete element method (DEM) is primarily employed for analyzing the dynamics of particulate systems involving multi-body interactions [143]. Within the DEM framework, a discontinuous powder bed is discretized into independent particle units, each representing an individual powder grain. The system's mechanical behavior is then resolved by computing interparticle contact forces, collision dynamics, and boundary interactions.

Unlike continuum-based approaches such as the Finite Element Method (FEM) and the Finite Volume Method (FVM), DEM explicitly treats materials as assemblies of discrete particles rather than continuous media. This enables a more realistic representation of powder morphology, particle size distribution, and porosity evolution during the spreading process.

In addition, DEM applies Newtonian mechanics to resolve interparticle interactions, allowing accurate characterization of particle trajectories, velocities, orientations, and accelerations. Owing to its capability to capture the inherently discontinuous nature of granular materials, DEM has become an indispensable numerical tool for investigating powder dynamics and powder bed spreading mechanisms in laser powder bed fusion (LPBF), providing valuable insights and reliable computational support for process optimization [144][145].

3.2.1 Geometry description

LPBF employs two primary techniques for distributing powder layers: scraping and counter-rolling [146]. Among these, scraping is widely adopted in commercial LPBF systems, including those developed by EOS, SLM Solutions, and Renishaw, due to its straightforward implementation. This approach utilizes a blade mechanism to evenly spread the powder, making it a prevalent choice in industrial applications [147]. Given its simplicity and broad usage, this study focuses on the scraping method as the selected powder deposition technique. In this study, the initial powder bed is generated using a poured packing approach, wherein approximately 166541 spherical particles are produced based on the particle size distribution illustrated in Fig. 3.1(a). The powder spreading process is modeled as shown in Fig. 3.1(b), where the powder is deposited on a rigid substrate by a flat blade moving at a constant velocity. The computational domain has a length L = 21 mm and a width W = 3 mm, as shown in Fig. 3.1(c), representing a representative section of the actual powder bed used in the LPBF process.

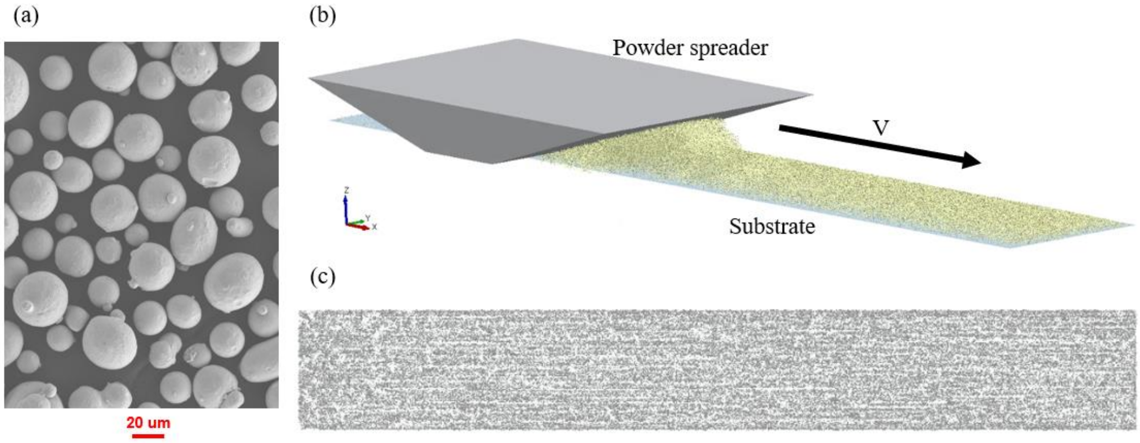

Fig. 3.1. Discrete element modeling of the powder spreading process. (a) SEM image of 316L stainless steel powders showing particle size distribution. (b) Schematic of powder spreading by a moving blade in the DEM simulation. (c) Top view of the deposited powder bed after spreading.

In a powder system composed of non-spherical particles, the overall behavior differs significantly from that of a system consisting of spherical particles. This discrepancy arises because the irregular shape of non-spherical particles limits their relative movement to some extent [148]. However, the majority of metal powders utilized in LPBF are predominantly spherical, though minor deviations from perfect sphericity may exist [81][149][150]. This characteristic is also observed in the 316L stainless steel powder used in our powder-layering experiments, as illustrated in Fig. 3.1(a). Given that the powder particles in this study are primarily spherical, the influence of particle shape on powder flow dynamics was not explicitly considered. Instead, a spherical representation was adopted for the powder particles in DEM simulations. Furthermore, the geometric boundaries, including the blade and the built part, are modeled as special particles with infinitely large mass [136]. Consequently, their motion remains unaffected by the interactions with powder particles.

3.2.2 Governing equations

In contrast to other computational approaches, the molecular dynamics-based DEM offers distinct advantages in capturing the interactions among individual particles or powders at the particulate scale. Due to its capability to accurately model particle-level dynamics, this method is applied in this numerical study, and each particle undergoes two fundamental types of motion within the framework of DEM modeling: translational and rotational. These motions are governed by the fundamental principles of Newton's second law of motion, which dictate the dynamic evolution of particles based on the forces and torques acting upon them. The governing equations for these motions are formulated as follows [151]-[153]:

$$m_i \frac{dv_i}{dt} = \sum_{j=1}^{p} \left(F_{ij,n} + F_{ij,s}\right) + m_i g \tag{3-1}$$

$$I_i \frac{dw_i}{dt} = \sum_{j=1}^{p} \left(T_{ij,s} + T_{ij,r}\right) \tag{3-2}$$

Where m_i, v_i, w_i and I_i denote the mass, translational velocity, angular velocity, and moment of inertial of particle i, respectively. The contact force exerted between two interacting powder particles, i and j, consists of a normal force $F_{ij,n}$ and a tangential force $F_{ij,s}$. Additionally, the tangential force generates a torque ($T_{ij,s}$), while rolling friction contributes to the torque ($T_{ij,r}$), influencing the rotational dynamics of the particles.

In the present simulation, the Hertz-Mindlin contact model was employed to characterize the elastic contact forces between particles. To account for Van der Waals interactions, the JKR (Johnson-Kendall-Roberts) theory was incorporated by modifying the Hertz-Mindlin framework. This modification involved introducing additional cohesive forces into the normal contact force, effectively capturing the adhesive interactions between particles [136][153][154]:

$$F_{c,ij}^{n} = \frac{4E^*}{3R^*} r_c^3 - 4\sqrt{\pi r_c^3 \gamma E^*} \tag{3-3}$$

$$\alpha = \frac{r_c^2}{R^*} - \sqrt{\frac{2\pi\gamma r_c}{E^*}} \tag{3-4}$$

where γ represents the surface energy, while E^* and R^* denote the equivalent Young's modulus and equivalent radius, respectively. The contact radius r_c is determined based on the normal overlap α. And a comprehensive summary of all forces and torques governing the translational and rotational motion equations for particle i is presented in Table 3.1[136][153]. The DEM formulation adopted in this study is based on several commonly accepted assumptions. Specifically, particles are assumed to be spherical and interact through pairwise contact forces governed by a soft-sphere contact model. The contact behavior follows Hertz–Mindlin theory, including elastic normal forces, tangential forces with Coulomb friction, and viscous damping. Additionally, particles are treated as rigid bodies, and effects such as particle deformation beyond contact overlap, cohesion, and thermal–mechanical coupling are neglected.

Table 3.1 Governing equations of the DEM model based on Hertz–Mindlin contact theory.

Forces and torques		Symbols	Equations
Normal direction	Interaction force	$F_{ij,n}$	$F_{ij,n} = F^n_{c,ij} + F^n_{d,ij}$
	Contact force	$F^n_{c,ij}$	$F^n_{c,ij} = \frac{4E^*}{3R^*} r_c^3 - 4\sqrt{\pi r_c^3 \gamma E^*}$
	Damping force	$F^n_{d,ij}$	$F^n_{d,ij} = -\sqrt{\frac{20}{3}}\beta[E^* m^*(R^*\alpha^n)^{0.5}]^{0.5} u^n_{ij}$
Tangential direction	Interaction force	$F_{ij,s}$	$F_{ij,s} = F^s_{c,ij} + F^s_{d,ij}$
	Contact force	$F^s_{c,ij}$	$F^s_{c,ij} = -\min\{F_f, \lvert 8G^*\sqrt{R^*\alpha^n}\alpha^s \rvert\}$
	Damping force	$F^s_{d,ij}$	$F^s_{d,ij} = \sqrt{\frac{80}{3}}\beta[G^* m^*(R^*\alpha^n)^{0.5}]^{0.5} u^s_{ij}$
Friction force		F_f	$F_f = \mu_s \lvert F^n_{c,ij} \rvert$
Friction torque		$T_{f,ij}$	$T_{f,ij} = R_i \times F^s_{c,ij}$
Rolling torque		$T_{r,ij}$	$T_{r,ij} = -\mu_r R_i F^n_{c,ij} \widehat{w}_i$
(where)		R^*	$R^* = R_i R_j/(R_i + R_j)$
		m^*	$m^* = m_i m_j/(m_i + m_j)$
		E^*	$E^* = E_i E_j/(E_i(1-\sigma_j^2) + E_j(1-\sigma_i^2))$
		G^*	$G^* = G_i G_j/[G_i(1-\sigma_j) + G_j(1-\sigma_i)]$
Unit angular velocity		$\widehat{w}_i$	$\widehat{w}_i = w_i/\lvert w_i \rvert$

3.2.3 Calculation time step

In DEM simulations, the selection of an appropriate time step Δt is crucial for accurately computing the incremental contact forces and displacements of particles. To ensure numerical stability and minimize computational errors, the chosen time step must be smaller than a characteristic time scale. A commonly used criterion for this purpose is the Rayleigh critical time step [155], which serves as a representative characteristic time for the system, and the formula is as follows:

$$\Delta t_{Ray} = \frac{\pi R_p}{0.8766 + 0.163\sigma}\sqrt{\frac{\rho_p}{G}} \tag{3-5}$$

where R_p is the particle radius, σ is the Poisson's ratio, $G = E/2(1+\sigma)$ is the shear modulus and E is the Young's modulus, and ρ_p is the particle density.

Determining an optimal time step in DEM simulations involves balancing computational efficiency, numerical accuracy, and the stability of the integration scheme. As reported by O'Sullivan and Bray [158], an appropriate time step for modeling the motion of dense granular materials typically ranges between 20% and 80% of the Rayleigh critical time step. In this study, to achieve a reasonable compromise between computational cost and solution accuracy, a time step Δt corresponding to 50% of the Rayleigh critical time step Δt_{Ray} was adopted for solving the governing equations of the model [136].

3.3 Multiphysics thermal-fluid flow model

The laser-powder interaction in LPBF is characterized by extremely short durations, microscale molten regions, and rapid cooling and solidification rates. These features, combined with the inherent complexity of the physical processes involved and the limitations of experimental observation techniques, make it challenging to fully capture melt pool dynamics through experiments alone. In recent years, numerical simulation has therefore emerged as a valuable tool for investigating the dynamic behavior of the melt pool at the particle scale.

This study employs Ansys Fluent software to numerically simulate the complex microscale physical phenomena occurring during the LPBF process, including heat conduction, fluid motion, and mass transfer. LPBF is a transient, non-steady-state manufacturing process involving rapid changes in multiple physical mechanisms. These include the absorption of laser energy by metal powders, molten metal flow, surface-tension-driven Marangoni convection within the melt pool, radiative and convective heat exchange between the powder bed and the surrounding environment, and phase transitions among solid, liquid, and gaseous states. Incorporating all these factors in full detail would result in an exceedingly complex mathematical model. Therefore, to maintain computational efficiency while preserving accuracy and focusing on the dominant physical phenomena, the following assumptions are adopted in this study [4][6][159]:

- The melt pool fluid flow is modeled as Newtonian and laminar.
- The thermophysical properties of SS316L are assumed to be temperature-dependent only.
- The plasma formation effects during the LPBF process are ignored.

3.3.1 Geometry description

This section presents the development of the physical model, using a single-track scanning case with a layer thickness of 50 μm as an example. The geometric dimensions of the model are 800 μm × 260 μm × 340 μm, and the substrate height is 200μm. Since the model is a regular rectangular cuboid, the mesh generation process does not require additional considerations for complex geometric features. Under identical volume and mesh resolution, the total number of hexahedral elements is significantly lower than that of tetrahedral elements, leading to a substantial reduction in computational cost and the number of nodes. Furthermore, compared to tetrahedral elements, hexahedral meshes exhibit superior computational accuracy and convergence properties. Therefore, hexahedral elements were selected for mesh discretization in this study.

As the powder region is directly subjected to laser irradiation, the associated fluid flow and heat transfer phenomena are highly intricate. Consequently, a finer mesh resolution is required in this region to ensure computational accuracy. When determining an appropriate mesh size, it is essential to consider that reducing the element size to 1/n of its original value results in an increase in the total number of elements by a factor of n^3. Additionally, a smaller mesh size necessitates a reduction in time step, leading to a significant increase in the number of computational steps and overall simulation time. Therefore, a balance between computational accuracy and efficiency must be achieved. Based on extensive testing, a mesh size of 4 μm was ultimately selected for the computational domain [82], resulting in approximately 1105000 total elements. The three-dimensional computational domain for simulating the single-track formation is illustrated in Fig. 3.2.

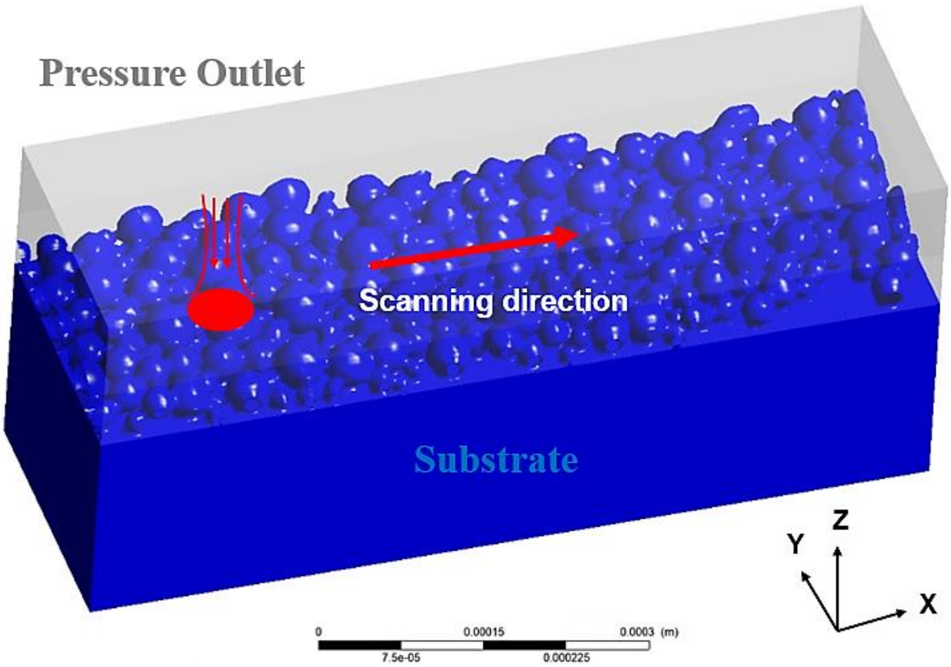

Fig. 3.2 Three-dimensional computational domain for simulating the single-track formation. The powder bed used

in this simulation has a thickness of 50 μm and consists of 316L stainless steel particles with a particle size distribution characterized by D10 = 15 μm, D50 = 30 μm, and D90 = 45 μm. Detailed powder characteristics, including packing density and morphology, are provided in Section 4.2.

3.3.2 Governing equations

This study focuses on the multiphysics coupling modeling of the molten pool, with an emphasis on developing physical and mathematical models that describe the fluid flow and heat transfer processes within the metal melt. For the numerical solution methodology, the Finite Volume Method (FVM), known for its strict conservation properties, is employed to discretize the governing equations. Specifically, the numerical solution of the system of partial differential equations-comprising the mass conservation equation, the momentum conservation Navier-Stokes equations, and the energy conservation equation-is achieved through the following steps: Firstly, based on the control volume integration principle, the nonlinear partial differential equations are integrated over spatial discrete elements. Secondly, the Gauss divergence theorem is applied to the surface integral terms to discretize the fluxes, thereby transforming the differential equations into algebraic equations at discrete nodes. Finally, the assembled field elements form a large, sparse system of linear algebraic equations. This numerical approach rigorously ensures local conservation while effectively addressing multiphysics coupling problems under complex geometric boundary conditions, thus providing a robust computational foundation for the precise simulation of the molten pool's dynamic behavior. The subsequent sections primarily address the three fundamental governing equations of Computational Fluid Dynamics (CFD) and the development of additional models:

(1) Mass conservation equation

The mass conservation equation, also known as the continuity equation, is a fundamental principle that must be satisfied in any fluid flow problem. This law can be stated as follows: the increase in mass within a fluid element over a unit of time is equal to the net mass flux entering the element during the same time interval. The specific mathematical form of the mass conservation law is expressed as follows:

$$\nabla \cdot (\rho \vec{v}) = 0 \tag{3-6}$$

where ρ is the volume-averaged density, t is the time, $\vec{v}$ is the fluid velocity.

(2) Momentum conservation equation

The momentum equation is intrinsically based on Newton's Second Law, which states that the temporal rate of change of momentum within a differential fluid element is equal to the sum of all external forces acting upon it. The precise mathematical representation of the momentum conservation law is as follows:

$$\frac{\partial}{\partial t}(\rho \vec{v}) + \nabla \cdot (\rho \vec{v}\vec{v}) = -\nabla p + \rho \vec{g} + \nabla \cdot \bar{\bar{\tau}} + \vec{F} + \overrightarrow{f_{damp}} \tag{3-7}$$

where p is the pressure, $\vec{g}$ is the gravity acceleration, $\vec{F}$ is the main driving force including contributions from surface tension, Marangoni force, and recoil pressure, $\overrightarrow{f_{damp}}$ is the damping force term in the solidification and melting model, which will be introduced in subsequent sections, and τ is the stress tensor (described below),

$$\bar{\bar{\tau}} = \mu\left[(\nabla \vec{v} + \nabla \vec{v}^T) - \frac{2}{3}\nabla \cdot \vec{v} I\right] \tag{3-8}$$

(3) Energy conservation equation

The Laser powder bed fusion (LPBF) process involves highly frequent thermal exchanges, necessitating strict adherence to the law of energy conservation. This principle can be interpreted as follows: the rate of energy increase within an infinitesimal control volume is equal to the net heat flux entering the volume, combined with the work done on it by body forces and surface forces. Fundamentally, the law of energy conservation is a manifestation of the First Law of Thermodynamics and can be formulated in the form of an energy conservation equation:

$$\frac{\partial}{\partial t}(\rho H) + \nabla \cdot (\rho \vec{v} H) = \nabla \cdot (k \nabla T) + q \tag{3-9}$$

where H is the enthalpy, k is the thermal conductivity.

(4) Solidification and melting equation

The melting-solidification model developed in this study incorporates two key physical mechanisms. First, the thermodynamic effects of latent heat release and absorption during the metal melting/solidification phase transition are explicitly addressed in the energy conservation equation using the effective heat capacity method. Second, the momentum transport process is modeled by analogy to porous media flow, employing the enthalpy-porosity method. The specific mathematical modeling is constructed as follows:

For the treatment of latent heat during phase transitions, the energy conservation equation is modified by introducing an effective heat capacity term to account for phase change effects.

$$H = h_{ref} + \int_{T_{ref}}^{T} C_p dT + f_l L_m \tag{3-10}$$

where h_{ref} is the reference enthalpy at the reference temperature T_{ref} (298.15 K), C_p is the specific heat capacity, L_m is the latent heat of melting, f_l is the liquid fraction and calculated by the function of temperature.

$$f_l = \begin{cases} 0 & T < T_s \\ \dfrac{T - T_s}{T_l - T_s} & T_s < T < T_l \\ 1 & T > T_s \end{cases} \tag{3-11}$$

Where T_s and T_l are the solidus and liquidus temperature, respectively.

For the momentum transport modeling in the solid-liquid coexistence region, the Enthalpy-Porosity method is employed, treating the mushy zone as an anisotropic porous medium. A coupling relationship is established between the liquid fraction f_l and the momentum dissipation source term, and the damping force term $\overrightarrow{f_{damp}}$ is described as

$$\overrightarrow{f_{damp}} = -A_{mush} \frac{(1 - f_l)^2}{\left(f_l{}^3 + C_K\right)} \vec{v} \tag{3-12}$$

Here, A_{mush} represents the damping coefficient of the mushy zone, which physically characterizes the momentum dissipation effects induced by dendritic structures at the phase transition interface on the molten flow. When f_l = 1, the source term automatically degenerates and decouples, ensuring that the pure liquid region satisfies the standard Navier-Stokes equations. Numerical stability of the model is ensured by introducing a regularization parameter C_K (typically set to 1×10^{-6}). Additionally, a continuous phase change function is employed to describe the temperature dependence of f_l(T), effectively achieving a continuous medium representation of the solid-liquid interface.

(5) VOF equation

In the past, significant advancements have been made in the computational modeling and simulation of moving interfaces, particularly through the development of methods for solving the Volume of Fluid (VOF) equations. These methods have demonstrated high numerical accuracy and robustness in practical applications, leading to the widespread adoption of the VOF approach in the analysis of flow fields involving free surfaces. The primary advantage of the VOF model lies in its ability to simulate two or more immiscible fluids by solving a single set of momentum equations while tracking the volume fraction of each fluid within the computational domain. This capability is the main reason for adopting the VOF model in this study. The method is based on the assumption that the fluids (or phases) involved are immiscible and do not interpenetrate. For each additional phase incorporated into the VOF model, a scalar variable representing the volume fraction of that phase in each computational cell is introduced. The sum of the volume fractions of all phases within any control volume satisfies the following conservation constraint:

$$\sum_{q=1}^{N} \alpha_q = 1 \tag{3-13}$$

where α_q denotes the volume fraction of phase q, and N represents the total number of phases.

Once the volume fractions are known at all locations, the physical properties and variables within multiphase regions are computed using volume-weighted averages. Consequently, the properties in any control volume may represent either a single phase or a mixture of phases, depending on the local volume fraction. Specifically, for phase q with volume fraction α_q, three scenarios are possible:

1. $\alpha_q = 0$: The control volume contains no fluid of phase q.

2. $\alpha_q = 1$: The control volume is entirely occupied by phase q.

3. $0 < \alpha_q < 1$: The control volume contains both phase q and other phases, representing an interfacial cell.

This framework allows the VOF method to effectively capture complex interfacial dynamics while ensuring strict mass conservation, making it a robust tool for multiphase flow simulations. In this work, gas phase is regarded as the primary phase, and the volume fraction of metal phase is solved by the following equation:

$$\frac{\partial}{\partial t}(\alpha_m \rho_m) + \nabla \cdot (\alpha_m \rho_m \vec{v}) = -\dot{m}_{lv} \tag{3-14}$$

$$\dot{m}_{lv} = 0.82 \sqrt{\frac{M}{2\pi RT}} P_{atm} exp\left[\frac{ML_v}{RT_v}\left(1 - \frac{T_v}{T}\right)\right] |\nabla \alpha_m| \tag{3-15}$$

where α_m is the volume fraction of metal phase, and ρ_m is the metal density. Since the volume fraction equation will not be solved for the primary phase, the gas-phase volume fraction will be computed based on the following constraint:

$$\alpha_g = 1 - \alpha_m \tag{3-16}$$

(6) Momentum source terms

During metal melting, the formation of a liquid melt pool is primarily driven by surface tension, which acts as the dominant force promoting the contraction of the melt pool surface. Surface tension inherently strives to minimize the surface area of the liquid, leading to a smoother and more stable melt pool morphology. Surface tension is incorporated as a volumetric force via the Continuum Surface Force (CSF) model:

$$\overrightarrow{f_{st}} = \sigma \kappa \vec{n} |\nabla \alpha_m| \frac{2\rho}{\rho_m + \rho_g} \tag{3-17}$$

where σ is the surface tension coefficient, ρ_m is the metal density, ρ_g is the gas density, α_m is the volume fraction of metal phase. The $|\nabla \alpha_m|$ function is adopted to transform an interfacial force per unit area into a volumetric surface force. κ is the curvature of metal-gas interface, $\vec{n}$ is the unit normal vector at metal-gas interface, which can be expressed as

$$\vec{n} = \frac{\nabla \alpha_l}{|\nabla \alpha_l|} \tag{3-18}$$

$$\kappa = -\nabla \cdot \vec{n} \tag{3-19}$$

Typically, the surface tension coefficient of a metal is a function of temperature and generally decreases as the temperature increases. This relationship can be expressed by the following equation:

$$\sigma(T) = \sigma_{ref} + \frac{\partial \sigma}{\partial T}(T - T_{ref}) \tag{3-20}$$

Where $\sigma(T)$ is the the surface tension coefficient as a function of temperature, σ_{ref} is is the reference surface tension coefficient, T_{ref} is the reference temperature (generally taken at the solidus temperature). This equation introduces an additional tangential force source term into the momentum equation, known as the Marangoni force. This force drives the flow of molten metal within the melt pool from high-temperature regions with lower surface tension to low-temperature regions with higher surface tension, and it is expressed as a volumetric force:

$$\overrightarrow{f_M} = \frac{d\sigma}{dT}[\nabla T - (\vec{n} \cdot \nabla T)\vec{n}]|\nabla \alpha_m| \frac{2\rho}{\rho_m + \rho_g} \tag{3-21}$$

Where T is the temperature, $\frac{d\sigma}{dT}$ is the temperature coefficient of surface tension (typically negative, indicating reduced surface tension at higher temperatures).

Under high-power-density laser irradiation, when the melt pool's thermal field exceeds the alloy's threshold vaporization temperature (T_v), localized explosive vaporization occurs at the liquid-gas interface. This phase-transition process induces a vapor jet flux perpendicular to the free surface, generating a dynamic counterforce through momentum conservation in accordance with Newtonian reaction principles. To consistently integrate this recoil mechanism within multiphase flow simulations, the pressure discontinuity at the evaporating interface is converted into a volumetric source term via the continuum surface force (CSF) formalism, maintaining numerical consistency with Marangoni stress modeling approaches. And the recoil vapor pressure $\overrightarrow{P_r}$ is defined as

$$\overrightarrow{P_r} = 0.54P_{atm}exp\left[\frac{ML_v}{RT_v}\left(1 - \frac{T_v}{T}\right)\right]\vec{n}|\nabla \alpha_m| \frac{2\rho}{\rho_m + \rho_g} \tag{3-22}$$

L_v is the latent heat of vaporization.

(7) Energy source terms

In laser powder bed fusion (LPBF) additive manufacturing, the numerical modeling fidelity of laser energy deposition mechanisms critically determines the predictive accuracy of melt pool dynamics and defect evolution. Although conventional heat source models (e.g., Gaussian surface heat flux, double ellipsoid volumetric source) are widely adopted, their inherent limitations manifest in two aspects: (i) failure to account for energy absorption heterogeneity induced by multiscale powder bed architectures (particle size distribution, porosity gradients), particularly local light scattering and thermal flux distortion at interparticle contact points; (ii) inability to resolve laser multi-reflection absorption phenomena caused by dynamic keyhole-pool interface fluctuations, leading to significant deviations in spatial energy deposition profiles.

To address these challenges, this study employs a ray-tracing-based interface-adaptive heat source model. By discretizing the laser beam into statistical ray clusters via Monte Carlo methods, this model tracks the interaction process between each ray and the gas-liquid interface at each timestep. The energy deposition source term is formulated as:

$$q_{laser} = \left[I_0(r)(\overrightarrow{I_0} \cdot \overrightarrow{n_0})\alpha_{Fr}(\theta_0) + \sum_{M=1}^{N} I_M(r,z)(I_M \cdot n_M)\, \alpha_{Fr}(\theta_M) \right] \cdot |\nabla \alpha_m| \frac{2\overline{\rho C_p}}{\rho_m C_m + \rho_g C_g} \tag{3-23}$$

$$\eta_\theta = 1 - \frac{1}{2}\left[\frac{1 + (1 - \eta_0 cos\theta)^2}{1 + (1 + \eta_0 cos\theta)^2} + \frac{{\eta_0}^2 - 2\eta_0 cos\theta + 2cos^2\theta}{{\eta_0}^2 + 2\eta_0 cos\theta + 2cos^2\theta} \right] \tag{3-24}$$

$$I = \frac{2P}{\pi {r_b}^2} exp\left[-2\frac{(x + v_0 t - x_0)^2 + (y - y_0)^2}{{r_b}^2} \right] \tag{3-25}$$

The radiation source term is formulated as:

$$q_{rad} = -\sigma_s \varepsilon (T^4 - T_0^4)|\nabla \alpha_m| \frac{2\overline{\rho C_p}}{\rho_m C_m + \rho_g C_g} \tag{3-26}$$

The evaporation source term is formulated as:

$$q_{evp} = -\dot{m}_{lv} L_v \tag{3-27}$$

where $\dot{m}_{lv}$ is the source term of mass transfer rate from liquid melt to vapor due to vaporization.

3.3.3 Initial and Boundary conditions

The initial conditions for the simulation are established by defining the material properties and temperature distribution across the entire computational domain at the commencement of the LPBF process. Throughout the LPBF procedure, the temperature field *T* is transient and exhibits a spatiotemporal dependency, varying both in space and over time. At the initial time

t = 0, it is assumed that the powder bed possesses a uniform temperature distribution. This assumption allows the initial temperature condition to be mathematically formulated as:

$$T(x,y,z,t) = T_0 \tag{3-28}$$

In this expression, T_0 denotes the initial temperature of the powder bed as well as the surrounding environment, which is set to a standard ambient temperature of 293 K. This uniform initial temperature assumption serves as a baseline for analyzing the thermal behaviour and heat transfer mechanisms during the subsequent stages of the laser melting process.

In computational fluid dynamics (CFD) simulations, the imposition of well-defined boundary conditions at the domain boundaries is essential to ensure the uniqueness and physical validity of the solutions to the governing equations. In this model, the boundary conditions are categorized into two types: thermodynamic boundaries (associated with the substrate region) and flow boundaries (associated with the gas region), as illustrated in Fig. 3.2. The computational domain comprises two hexahedral cells of identical geometric dimensions. The gas domain, positioned above the substrate, is assigned a *Pressure Outlet* boundary condition, permitting the free diffusion of the vapor-argon gas mixture. In contrast, the bottom and four lateral faces of the substrate domain are subjected to *Robin boundary conditions* (third-type boundary conditions), where the heat flux is governed by a combination of Newton's law of cooling and the Stefan-Boltzmann law:

$$q = h(T_w - T_\infty) + \varepsilon\sigma(T_w^4 - T_\infty^4) \tag{3-29}$$

where T_∞ = 300 K represents the ambient gas temperature, h = 10 W/(m^2 · K) is the convective heat transfer coefficient [161][162], and ε = 0.3 denotes the surface emissivity [162].

3.3.4 Calculation time step

The selection of the time step is closely related to the mesh cell size, fluid velocity, and computational stability, as shown in the following equation :

$$\Delta t = C\frac{\Delta x}{v} \tag{3-30}$$

Where C is Courant number, v is the fluid velocity, and Δx is the mesh cell size.

The Courant number (CFL), a dimensionless parameter that quantifies the relationship between the spatial and temporal discretization, directly influences numerical stability and convergence behavior. Generally, a higher Courant number accelerates convergence but can also induce numerical oscillations or divergence, compromising solution stability. Therefore, in transient flow simulations, the Courant number must be appropriately controlled to ensure both solution stability and computational efficiency.

In ANSYS Fluent, the solver automatically terminates the computation if the local Courant number (CFL) exceeds 250, as excessive values may lead to significant numerical errors or solution instability. To achieve a balance between computational stability and efficiency, this study employs an adaptive time-stepping strategy, dynamically adjusting the time step within the range of $10^{-9}\sim10^{-7}$ s. At each time step, the CFL number is rigorously monitored to remain below 0.5 [163], thereby optimizing the balance between numerical accuracy and convergence speed while ensuring computational stability and efficiency.

3.4 Physical parameters

In order to accurately simulate the thermal-fluid behavior of the melt pool during the LPBF process, appropriate thermophysical properties and computational constants must be defined. The material system investigated in this study consists of 316L stainless steel powder and argon as the inert shielding gas. The relevant temperature-dependent thermophysical properties, including density, thermal conductivity, specific heat capacity, dynamic viscosity, surface tension, and latent heat of fusion, are summarized in Table 3.2[156]. These parameters are essential for solving the governing equations related to heat transfer, fluid flow, and phase change phenomena within the melt pool. Additionally, to ensure numerical stability and convergence of the CFD simulations, appropriate computational constants were selected and are listed in Table 3.3[157]. These include values such as the Marangoni coefficient, absorption coefficient, laser beam parameters, and other empirical or model-specific constants used to capture interfacial effects and laser-material interactions. The careful selection of these parameters ensures both physical realism and computational robustness in the multiphysics model.

Table 3.2. Thermophysical properties of stainless steel 316 L and argon gas[156]

Properties & units	Stainless Steel 316 L		Argon
	Solid	Liquid	
Density (kg m^{-3})	7650	6870	1.628
Melting temperature (K)	1658 (solidus)	1723 (liquidus)	
Melting latent heat (J kg^{-1})	2.7×10^{5}		-
Boiling temperature (K)	3090		
Boiling latent heat (J kg^{-1})	7.45×10^{6}		
Specific heat (J kg^{-1} K^{-1})	462 + 0.134 T	775	520
Thermal conductivity (W m^{-1} K^{-1})	9.248+0.01571T	12.41+0.003279T	0.017
Viscosity (Pa s)	-	0.006	2.26×10^{-5}
Surface tension (N m^{-1})	-	$1.6-8.0\times10^{-4}$ T	-
Molar mass (g mol^{-1})	55.93		39.95
Young’s Modulus (MPa)	2.2×10^{3}		
Poisson’s ratio	0.3		-
Damping ratio	0.5		

Table 3.3 Computational constants[157]

Properties & units	Value
Mushy zone number A_{mush} *(kg m*$^{-3}$ *s*$^{-1}$*)*	1×10^{7}
Ambient pressure $\mathbf{P_{atm}}$ (Pa)	101325
Ambient temperature $\mathbf{T_{\infty}}$ (K)	300
Universal gas constant **R** (J K^{-1} mol^{-1})	8.314
Stefan-Boltzmann constant $\boldsymbol{\sigma_s}$ (kg s^{-3} K^{-4})	5.67×10^{-8}
Radiation Emissivity ε	0.3

3.5 Conclusion

This chapter establishes the theoretical and computational foundation for simulating the LPBF process through a multiphysics numerical framework. First, the Discrete Element Method (DEM) is employed to model the powder spreading process, where the particle-particle and particle-substrate interactions are described using the Hertz-Mindlin with JKR contact model. This allows accurate representation of powder packing, adhesion, and mechanical behavior during recoating, forming a realistic initial condition for subsequent laser interaction.

Next, a comprehensive computational fluid dynamics (CFD) model is developed to capture the complex thermal-fluid behavior of the melt pool. The model incorporates a moving Gaussian volumetric heat source based on ray-tracing principles to simulate spatial laser energy absorption in 316L stainless steel[157]. Key physical phenomena-including Marangoni-driven convection, capillary flow, recoil pressure, and phase change-are integrated within a thermofluid-solid coupled framework to investigate melt pool evolution and stability.

Through this integrated modeling strategy, the interplay between energy input, heat transfer, fluid motion, and phase transformation is quantitatively characterized. The validated model forms the basis for in-depth analysis of defect formation mechanisms and spattering dynamics in the following chapters, enabling a deeper understanding of how process parameters influence LPBF part quality.

Chapter 4. Experimental Comparison and Numerical Model Validation

4.1 Introduction

In the previous chapter, three types of numerical models were established for multiscale physical processes: a powder-scale powder spreading kinetics model, a melt-pool-scale fluid dynamics and heat transfer model, and a multiphase flow model accounting for particle-airflow coupling effects. Rigorous experimental validation of numerical results is essential to ensure the reliability of model predictions. The validated models effectively analyze key characteristic parameters including powder packing density distribution, melt pool flow characteristics, evolution of melt pool surface morphology, and characteristics of particle spatter intensity and spatial distribution. This analysis reveals the underlying physical mechanisms such as heat transfer mechanisms, balling and lack of fusion (LOF) effects, particle spattering behavior, and denudation phenomena in the laser-material interaction process. Furthermore, it elucidates their causal relationships with manufacturing defects. This chapter conducts a systematic comparative analysis based on experimental data and simulation results across multiple scales to verify the physical accuracy, numerical convergence, and engineering applicability of the models, thereby providing theoretical support for process optimization.

4.2 Experimental methodology

The experimental methodology involves the use of 316L stainless steel as the study material, known for its excellent mechanical properties and extensive application in additive manufacturing. The LPBF experiments were carried out using a commercial machine Realizer SLM 50, which provides precise control over laser parameters such as power, scanning speed, and spot size. To capture and analyze the outcomes, a combination of advanced characterization tools was employed. High-resolution microscopy, including scanning electron microscopy (SEM) and optical microscopy, was used to examine track morphology, pore structures, and material surface properties. To monitor and analyze dynamic phenomena during the LPBF process, a high-speed camera was employed to record real-time melt pool behavior and spattering dynamics at high temporal resolution. Additionally, a digital camera was utilized for broader visual documentation of experimental conditions and results, providing complementary perspectives for analysis. The integration of these imaging techniques ensures a comprehensive observation of the process outcomes, which serve as the basis for validating numerical models.

4.2.1 The LPBF system

The Laser powder bed fusion (LPBF) experiments were conducted using the Realizer SLM50 shown in Fig. 4.1, a compact and versatile additive manufacturing system optimized for precision fabrication. The system offers a build platform with a diameter of 70 mm and a maximum construction height of 40 mm, making it suitable for small-scale experimental studies. It is equipped with a fiber laser, though due to a lack of recent maintenance and calibration in the ARL Lab, the operational power range has been constrained to 10 W to 100 W instead of its nominal capability. The machine operates on a stable power supply of 16 A at 230 V, with a power consumption of approximately 1.0 kW. An argon gas environment with a consumption rate of around 30 liters per hour is maintained in the chamber, ensuring reduced oxidation and consistent material quality throughout the process.

Physically compact (W 800 mm × D 700 mm × H 500 mm) and weighing approximately 120 kg, the SLM 50 is well-suited for laboratory environments. It is powered by the proprietary Realizer Control Software, enabling precise management of laser parameters, scanning strategies, and material processing conditions. The system supports a diverse range of materials, such as stainless steel, titanium, and aluminum, offering flexibility for various experimental applications. Despite current power constraints, the Realizer SLM 50 remains effective in facilitating detailed studies of melt pool dynamics, spattering, and track formation under varied laser parameters, contributing significantly to research in laser powder bed fusion processes.

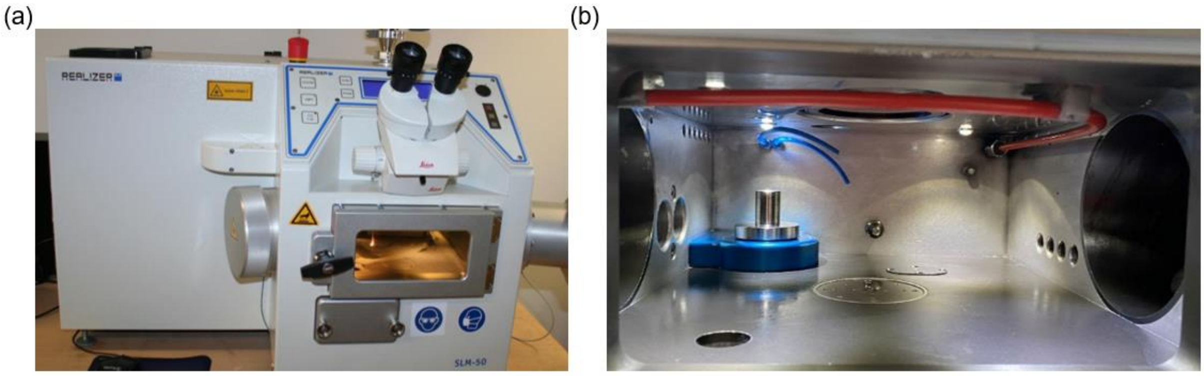

Fig. 4.1. SLM 50 equipment and internal structure.

To investigate melt pool dynamics and heat transfer mechanisms under higher laser power conditions, the XDM 250 Laser powder bed fusion (LPBF) system located at Yangzhou University was employed (as shown in Fig. 4.2), since the previously used SLM50 machine is limited to a maximum laser power of 100 W. The XDM 250 is equipped with a 500 W IPG fiber laser and supports layer thicknesses as low as 20 μm, enabling high-resolution process control. Its build volume ranges up to 250 mm × 250 mm × 410 mm, and it operates with a laser wavelength of 1070 nm. The system integrates proprietary software platforms (XDM IntelliProc™ and XDM IntelliMake™) for process planning and real-time monitoring. With a robust mechanical structure (approx. 2000 kg) and compatibility with a wide range of metallic powders-including tool steels, stainless steels, high-temperature alloys, titanium and aluminum alloys-the XDM 250 provides a versatile and stable platform for high-power laser–material interaction studies.

Fig. 4.2 The XDM 250 LPBF system used for high-power laser experiments.

4.2.2 The 316L powder and spreading process

Carpenter Additive (USA) PowderRange 316L F stainless steel powder was employed as the feedstock material in the LPBF process. The powder was produced using a nitrogen gas atomization process, ensuring spherical particle morphology and consistent quality. The particle size distribution of the powder, characterized in accordance with the ASTM B822 Standard Test Method for Particle Size Distribution by Light Scattering, exhibited a D10 of 15 μm, D50 of 30 μm, and D90 of 45 μm. This controlled particle size range ensures optimized packing density and flowability, both of which are critical for achieving high-quality layer deposition during the LPBF process. The narrow size distribution also supports stable laser absorption and uniform melt pool formation, contributing to the production of dense and defect-minimized parts. The chemical compositions supplied by the manufacturer are detailed in Table 4.1.

Table 4.1 The chemical compositions of 316L powder in the experiment.

Iron	Balance	**Chromium**	16.0–18.0 %	**Nickel**	10.0–14.0 %
Molybdenum	2.00–3.00 %	**Manganese**	2.00 %	**Silicon**	1.00 %
Nitrogen	0.10 %	**Oxygen**	0.10 %	**Phosphorus**	0.045 %
Carbon	0.030 %	**Sulfur**	0.030 %		

A manual powder spreading method was employed to prepare a uniform powder bed on a rectangular substrate with dimensions of 21 mm × 3 mm × 3 mm under tightly controlled environmental conditions (25°C ±0.5°C, RH <15%). To ensure precision, a four-sided film applicator was used as the spreading tool with a calibrated spreading velocity of 0.025 m/s , moving along the length of the substrate. The powder layer thickness was set to 50 μm, replicating typical LPBF process conditions. This approach provided controlled and consistent spreading, ensuring uniform layer deposition for subsequent experimental analysis.

4.2.3 High-Speed Camera Setup

As shown in Fig. 4.3, A HotShot 1700CC high-speed camera was employed to capture the dynamic behavior of spattering during the scanning process. The camera operates with a power supply of 12 VDC and a power consumption of 12 W. It was equipped with a SIGMA 105 mm f/2.8 EX DG MACRO lens, providing excellent optical clarity for close-up imaging. Positioned outside the chamber window of the SLM 50 system, the camera was set at an approximate 20° inclination from the horizontal axis to optimize the observation angle. The working distance between the lens and the laser melting area was approximately 135 mm, ensuring a clear field of view for capturing high-speed phenomena.

The HotShot 1700CC is capable of capturing up to 20,000 frames per second (fps) with a resolution of 224 × 206 pixels. However, in this study, a frame rate of 1,500 fps was utilized, paired with a higher resolution of 1,200 × 810 pixels to balance temporal and spatial detail. To enhance the camera’s ability to capture spatter dynamics, a powerful LED light source was employed to ensure sufficient illumination of the laser melting zone. This setup enabled the precise documentation of high-speed spattering events under controlled experimental conditions.

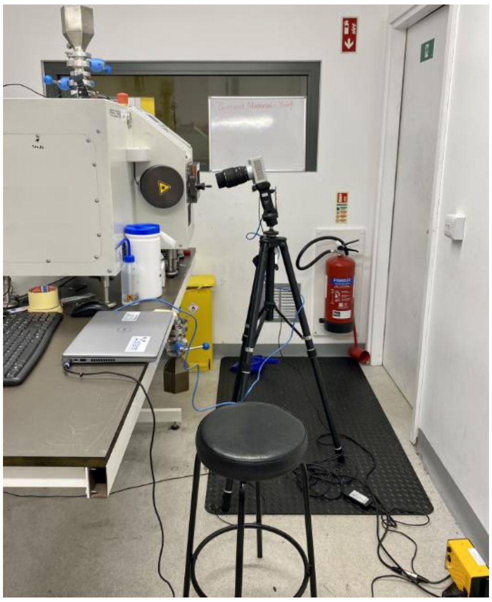

Fig. 4.3 High-speed camera setup for observing spattering during laser scanning.

4.2.4 Denudation Observation

To avoid disturbing the powder layer or risking sample damage during transportation, an Adonstar AD246S-M HDMI Digital Microscope was employed immediately after fabrication. This setup features a 7-inch LCD screen and 2160P UHD video recording, with an adjustable lens-to-object distance of 12 mm to 320 mm and a magnification range spanning from 4.5× to 180×. By positioning this device directly adjacent to the LPBF system, minimal handling was required, thereby preserving the integrity of the denudation zone and other fine details.

Under varying laser parameters, the microscope enabled high-resolution observation of the denudation phenomenon surrounding the melt tracks. Differences in laser power and scanning speed were systematically examined, allowing for precise visual documentation of particle displacement, powder thinning, and other surface characteristics. This immediate, in situ approach proved instrumental in correlating process conditions with localized changes in powder distribution, ultimately shedding light on the interplay between laser settings and material behavior in Laser powder bed fusion processes.

4.2.5 Microstructure Characterization

Following the documentation of the denudation zone using a digital camera post-LPBF fabrication, the samples were thoroughly rinsed with water to remove any residual surface powder particles. The cleaned specimens were then examined under a Leica DMLM optical microscope to observe and document the surface morphology and the quality of the printed tracks. This initial analysis provided essential data for evaluating the effects of different laser powers and scanning speeds on track formation. The detailed surface observations served as a critical reference point for correlating process parameters with surface characteristics, such as track uniformity, continuity, and defect distribution.

Subsequently, the samples were sectioned into multiple segments using an EDM wire-cutting machine, preparing them for cross-sectional analysis. Each segment was hot mounted in conductive resin to ensure stability during further preparation. The sample preparation process included a two-stage grinding and polishing procedure. During grinding, silicon carbide abrasive papers with grit sizes ranging from P320 to P4000 were employed to achieve a planar surface. The polishing stage further refined the samples using diamond suspensions of 6 μm and 1 μm particle sizes, followed by a mixture of 90 mL colloidal silica and 10 mL hydrogen peroxide for mirror-like polishing. A silica-based solution was applied for final polishing to enhance surface clarity.

To reveal microstructural features, the polished samples were etched using Kroll's reagent (6% nitric acid and 1% hydrofluoric acid) until melt pool boundaries and internal structures became visible. High-resolution observations of melt pool depth, width, and overall geometry were conducted using the Leica DMLM microscope. These observations, along with the recorded surface morphology data, enabled comprehensive analysis of the influence of laser parameters on track formation quality and melt pool behavior.

4.2.6 Powder Spatter Imaging Setup

To characterize the spatial distribution of powder spatters generated during the laser scanning process, an ex-situ imaging approach was employed following each single-track experiment. After laser processing, the build substrate was carefully removed from the laser powder bed fusion (LPBF) chamber and transferred to a clean, controlled environment to preserve the as-deposited spatter particles without disturbance.

The substrate was mounted on a height-adjustable tripod platform, allowing precise control over imaging height and alignment. A high-resolution Olympus PEN E-P5 mirrorless camera was securely affixed to a three-section aluminum tripod and positioned vertically above the substrate to enable orthogonal top-down imaging. This configuration minimized parallax distortion and ensured consistent image framing across all experimental conditions.

Key camera parameters—including aperture, exposure time, and ISO sensitivity—were manually optimized to maximize image clarity and contrast between the metallic substrate and fine powder deposits. Soft ambient lighting was employed to suppress glare and harsh shadows, enhancing the visibility of small particle features. The complete imaging setup is illustrated in Fig. 4.4.

Fig. 4.4. Experimental setup for post-scan powder spatter imaging.

4.3 Numerical Model Validation

4.3.1 Powder spreading model validation

The powder spreading process is a critical step in Laser powder bed fusion (LPBF), directly influencing the final part quality and the uniformity of the powder bed. During this process, powder is transported from the feed region to the build area and uniformly distributed into a thin layer by a recoating mechanism, such as a roller or a blade. This process involves the flow behavior, packing density, and interactions between the powder and the recoater, which can be affected by factors such as particle size distribution, morphology, and environmental conditions. The simulation depicted in Fig. 4.5 illustrates the process of distributing powder over the initial powder layer (1^{st} layer) and the already formed part, covering a region of 21 mm × 3 mm with a layer thickness of 50 μm. Initially, the first layer is deposited, and the powder intended for spreading accumulates along the recoating apparatus to form a mound. As the apparatus moves along the X-axis during spreading, the powder mound advances forward.

The recoating process is represented using a simplified kinematic model, which captures the essential features of powder spreading, including particle flow, accumulation, and layer formation. Initially, powder particles flow through the gap between the recoater and the previously spread powder layer, subsequently adhering to the surface of the solidified region. The process then continues across the remaining area of the first powder layer.

During this period, the size of the powder mound in front of the recoater gradually decreases, and the recoater comes to a stop once a uniform powder layer is formed. Although the recoater motion is simplified compared to that in practical LPBF systems, this representation is sufficient to reproduce the key characteristics of powder bed formation and provides a physically reasonable initial condition for subsequent thermo-fluid simulations.

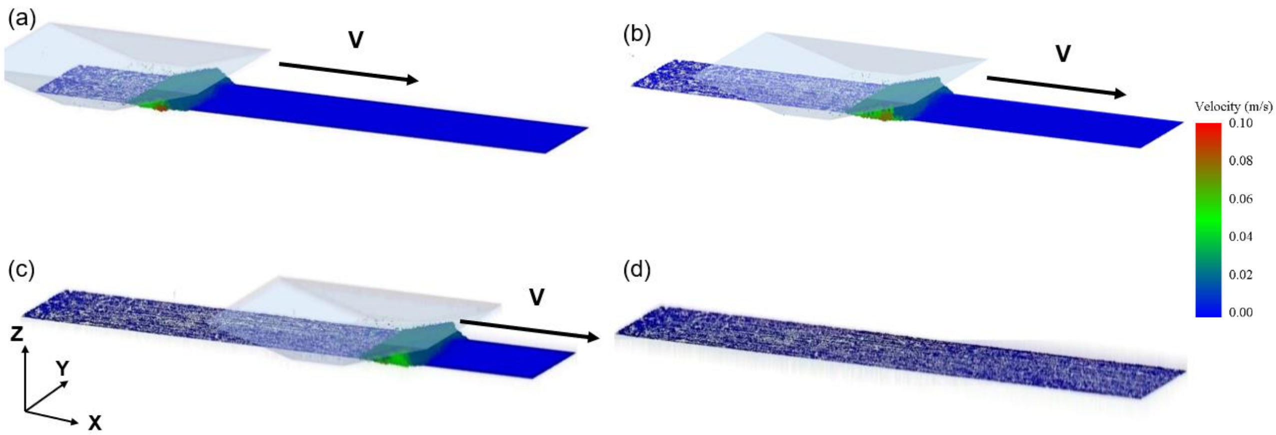

Fig. 4.5. DEM Simulation of powder spreading process.

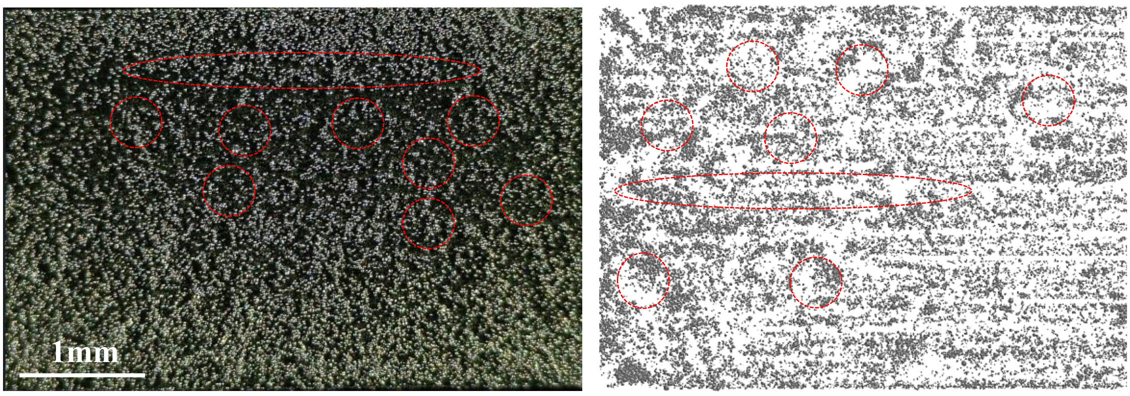

Fig. 4.6. Comparison between experimental observation and DEM simulation of powder particle distribution after powder spreading. Red circles indicate representative regions of particle accumulation and void formation in the powder bed. The packing densities obtained from experimental observation (analyzed with ImageJ) and DEM simulation are approximately 0.49 and 0.52, respectively, corresponding to a relative difference of about 6%.

The comparison between the DEM simulation results of the powder spreading model and the experimental observations is shown in Fig. 4.6. To quantitatively evaluate the agreement between simulation and experiment, the packing density of the powder bed was estimated using image analysis. Specifically, the experimental image and the DEM simulation image were processed using the open-source software ImageJ. The images were first converted to grayscale and then binarized using an automatic thresholding method to distinguish particles from void regions. The packing density was subsequently calculated as the ratio between the particle area and the total analyzed area. Based on this method, the packing densities obtained from the experimental observation and DEM simulation are approximately 0.49 and 0.52, respectively, corresponding to a relative difference of about 6%. This quantitative comparison indicates a reasonable agreement between the DEM simulation and the experimental observations in terms of powder particle distribution. Nevertheless, the powder bed still exhibits certain non-uniform characteristics, including localized particle accumulation and unfilled void regions (marked by red circles). These regions are highlighted as representative examples where the powder distribution deviates from the surrounding areas, indicating local variations in particle packing.

To further understand the formation mechanism of these non-uniform powder distributions, the motion behavior of powder particles during the spreading process was analyzed based on the particle velocity field obtained from the DEM simulation. Fig. 4.7 shows the instantaneous velocity vectors of powder particles during the spreading process. The results indicate that powder particles exhibit complex motion patterns when interacting with the recoating blade. Larger particles may displace surrounding smaller particles in multiple directions under the action of the blade, which may contribute to the formation of voids in the powder bed. Similar particle rearrangement behavior during powder spreading has also been reported in previous DEM studies of powder bed fusion processes[137][153]. These studies suggest that the interaction between the recoating blade and powder particles can induce particle displacement and rearrangement, which may influence the local packing structure of the powder layer.

Overall, the comparison between the experimental observations and DEM simulation results demonstrates that the proposed DEM model is capable of reasonably reproducing the powder spreading behavior and particle distribution characteristics observed in the experiment, providing a reliable basis for further analysis of powder spreading mechanisms.

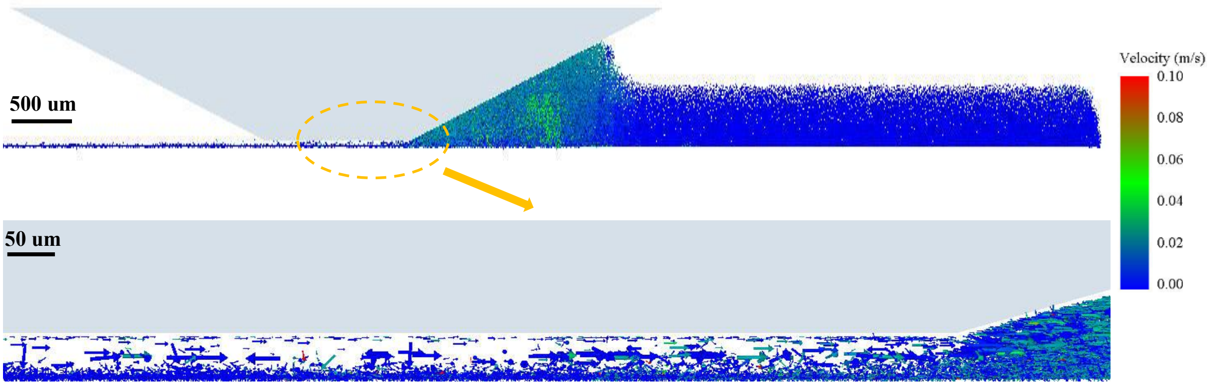

Fig. 4.7 Velocity vectors of powder particles during the spreading process obtained from the DEM simulation.

The arrows represent particle velocity vectors, while the dots indicate the particle positions.

4.3.2 Multiphysics thermal-fluid flow model validation

To rigorously validate the proposed multiphysics thermal-fluid flow model, a comprehensive comparison between simulation results and experimental observations under varying process parameters is essential. Among these parameters, the laser scanning speed plays a pivotal role in dictating the thermal gradients, melt pool dynamics, and the resulting morphology of the solidified track, thereby serving as a critical metric for assessing model accuracy.

The scanning speed directly influences the interaction time between the laser beam and the metal powder bed. Under constant laser power, a high scanning speed shortens this interaction time, leading to insufficient energy input. This results in incomplete melting, melt pool instability, and the occurrence of "balling"—a phenomenon where discrete, spherical droplets form along the scan path, severely compromising track continuity and mechanical integrity. Conversely, excessively low scanning speeds cause prolonged laser exposure, which can lead to excessive melting, increased thermal accumulation, and the formation of humps or even porosity due to keyholing or vaporization, all of which degrade part quality and reduce build efficiency. Hence, understanding the effect of scanning speed is crucial for optimizing process stability and ensuring consistent part quality.

Fig. 4.8.illustrates a direct comparison between simulated and experimentally observed single-track morphologies at three representative scanning speeds: 1.5 m/s, 1.0 m/s, and 0.5 m/s. The simulated surface profiles exhibit strong agreement with the corresponding scanning electron microscopy (SEM) images, thereby affirming the model's predictive capability.

- At a scanning speed of 1.5 m/s, the melt pool exhibits highly unstable behavior, characterized by severe balling. This is indicative of insufficient energy input per unit length, preventing full melting and causing droplet detachment due to surface tension instabilities.
- Reducing the speed to 1.0 m/s transitions the melt pool into a semi-stable regime. The

continuity of the melt track improves, although localized hump formation is still evident, suggesting intermittent instability due to marginal energy input.

- At 0.5 m/s, the melt pool achieves a steady-state condition. The energy input is sufficient to sustain a continuous and uniform melt track, reflecting stable wetting and solidification dynamics. However, it is notable that the track surface is decorated with numerous adhered satellite particles. These small, spherical particles likely originate from powder spattering and partial re-melting phenomena, driven by recoil pressure or vapor plume-induced entrainment. Their presence indicates that although macro-level melt pool stability is achieved, localized powder-gas-laser interactions are still active and may influence surface quality or subsequent layer bonding.

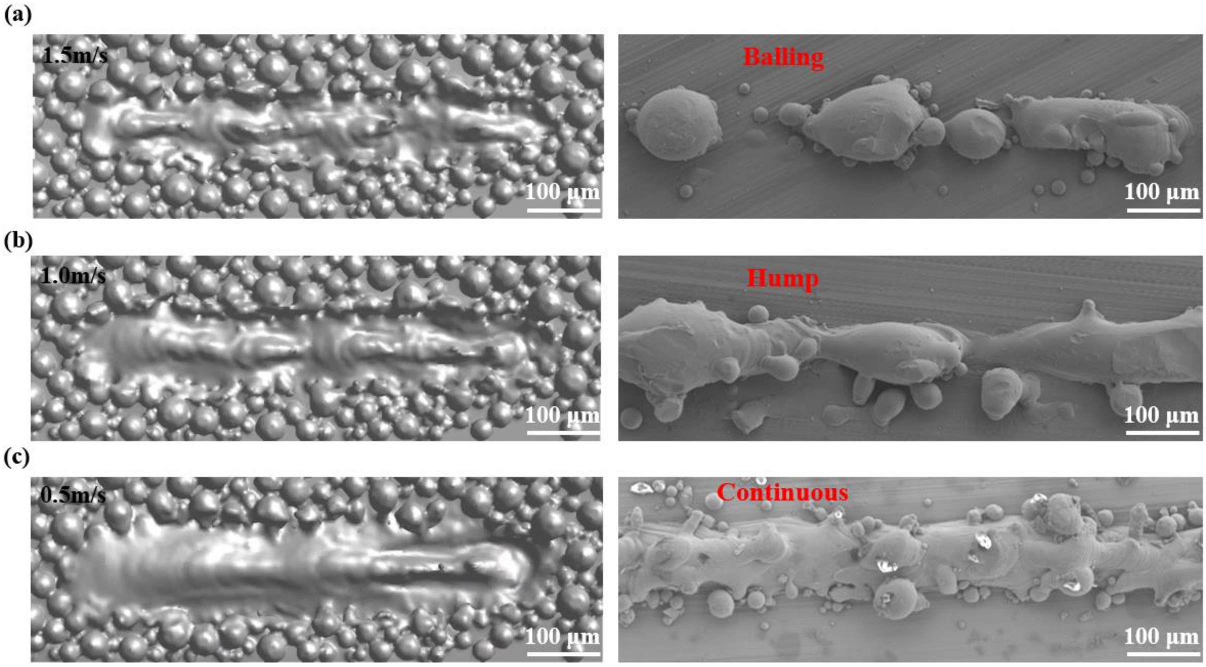

Fig. 4.8 Comparison between simulation and experimental single-track morphologies under varying laser scanning speeds. (a) 0.1 m/s, (b) 0.5 m/s, and (c) 1.0 m/s at a constant laser power. The corresponding regimes of balling, humping, and continuous tracks are indicated.

These observations support the classification of melt pool behavior into three distinct regimes: unstable (balling), transitional (humping), and stable (continuous tracks). As the scanning speed decreases under constant power, the laser energy density increases, enabling more controlled melt pool dynamics and improved track morphology—albeit with possible trade-offs in terms of surface cleanliness due to particle redeposition.

In conclusion, at constant laser power, the scanning speed is a dominant factor governing melt pool stability and surface morphology. While slower speeds can promote continuous track formation, attention must also be paid to associated phenomena such as powder spattering and particle adhesion, which may affect the final surface integrity. Therefore, careful optimization of scanning parameters is essential to balance track continuity, geometric precision, and surface quality in laser-based additive manufacturing processes.

4.4 Conclusion

This chapter presents an integrated experimental–numerical framework for investigating melt pool evolution and powder spattering behavior in the LPBF process. The combined experimental observations and numerical simulations provide several key findings.

First, high-speed imaging and post-process characterization reveal that melt pool dynamics strongly influence the generation and trajectory of powder spatters. The spatial distribution and deposition behavior of spatters are closely related to melt pool geometry and process parameters, highlighting the critical role of melt pool stability in controlling powder spattering.

Second, the DEM-based powder spreading model successfully reproduces the rolling, rearrangement, and packing behavior of powder particles during recoating. Quantitative analysis shows that the simulated packing density and spatial particle distribution are consistent with experimental observations, demonstrating that the DEM model can reasonably represent powder bed formation and provide reliable initial conditions for subsequent melt pool simulations.

Third, the developed thermal–fluid dynamics model captures the key physical phenomena governing melt pool evolution, including heat transfer, molten metal flow, and free surface deformation. The predicted melt track morphology shows good agreement with metallographic cross-sections and surface remelting features observed experimentally, confirming the model's accuracy in describing melt pool behavior.

Overall, the combined experimental–numerical approach provides a validated framework for quantitatively analyzing the coupled behavior of powder spreading, melt pool dynamics, and powder spattering in the LPBF process. The insights obtained in this chapter contribute to a deeper understanding of the underlying physical mechanisms and provide a foundation for future studies on process optimization and defect mitigation in laser-based additive manufacturing.

Chapter 5. Melt pool dynamics mechanism

5.1 Introduction

In LPBF, melt pool instabilities frequently give rise to process-induced defects such as porosity, hump formation, and balling, which severely compromise the mechanical performance and structural integrity of fabricated parts. Extensive research has been devoted to elucidating the fluid dynamic origins of these defects. Porosity is commonly attributed to unstable keyhole behavior, wherein fluctuations and collapse of vapor cavities trap gas within the solidifying melt pool, as revealed by in situ X-ray imaging studies [118]. Hump defects are generally explained as the result of melt pool flow oscillations and pressure imbalances, driven by recoil pressure and surface tension effects [165]. Balling, characterized by the formation of discontinuous spherical beads along the scan track, is widely linked to Plateau-Rayleigh instability and poor wetting, particularly at high scanning speeds [166].

Despite these insights, most existing studies have predominantly focused on hydrodynamic mechanisms-including Marangoni convection, capillary action, and recoil pressure-while comparatively less attention has been paid to the role of heat transfer in defect evolution. In fact, thermal transport governs not only the driving forces for melt pool flow but also directly influences melt pool geometry, solidification behaviour, and the onset of instabilities. Temperature gradients, along with melt pool shape and size, determine the rate and distribution of heat loss to the surrounding material. These thermal factors play a decisive role in triggering or suppressing different types of process defects, yet they are often oversimplified or treated as secondary in existing models.

This paper addresses the critical knowledge gap by integrating ray-tracing-based CFD simulations with experimental validation to construct a heat-transfer-centric framework for re-evaluating the formation mechanisms of porosity, hump, and balling in LPBF. Unlike previous simplistic interpretations that associate increased scanning speed merely with reduced total energy input, our findings uncover a deeper mechanism by coupling heat transfer with flow dynamics. We demonstrate that melt pool behavior is fundamentally governed by the rate of interfacial heat extraction at the solid-liquid boundary and by spatially localized thermal inhomogeneities. We further reveal that, under varying thermal transfer conditions and laser parameters, Marangoni convection plays a pivotal but distinct role in driving different defect types. Finally, we explore the impact of preheating on defect suppression, reinforcing the conclusion that dynamic thermal imbalance—rather than absolute energy input—is the dominant driver of defect formation in LPBF.

5.2 Time-resolved interfacial heat flux governs melt-pool morphology

Conventional interpretations typically attribute the occurrence of keyhole-induced porosity to excessive heat input, while hump and balling defects are commonly associated with insufficient energy delivery. Such simplified correlations, however, obscure the complex and dynamic nature of melt pool behavior and mask the critical role of transient thermal dissipation at the melt–substrate interface. To address this limitation, we evaluate the interfacial heat flux $q_{IA}(t)$, defined as the area-averaged conductive heat flux across the melt pool-substrate interface at a given time**:**

$$q_{IA} = \frac{\lambda}{A}\sum_{i} A_i |\nabla T|_i \tag{5-1}$$

where A is the total interfacial area, λ is the thermal conductivity, A_i is the area of the i-th discretized interface element, and $|\nabla T|_i$ is the temperature gradient normal to the interface at that element. This quantity represents the local intensity of heat extraction and provides a direct measure of interfacial thermal transport.

The temporal evolution of $q_{IA}(t)$ under laser powers of 100 W and 200 W is shown in Fig. 5.1(a). In most cases, $q_{IA}(t)$ exhibits pronounced temporal fluctuations rather than reaching a steady state, indicating that interfacial heat transfer is inherently dynamic and far from equilibrium. These fluctuations arise from the continuous redistribution of temperature gradients and melt flow within the evolving melt pool, as discussed in the following section.

Fig. 5.1(b) presents the average interfacial heat flux $\overline{q_{IA}}$ and its fluctuation intensity. It increases systematically with scan speed for both power levels, reflecting enhanced heat extraction at higher processing speeds. However, this monotonic trend does not directly correspond to the observed evolution of melt-track morphology (Fig. 5.1(d)), which instead exhibits a non-monotonic transition from smooth tracks to humping and eventually to balling. For example, the value of $\overline{q_{IA}}$ at 200 W and 1 m/s is higher than that at 100 W and 0.75 m/s, yet the former produces a smooth track while the latter exhibits hump formation. Similarly, although $\overline{q_{IA}}$ at 200 W and 2 m/s exceeds that at 100 W and 1.5 m/s, the former results in hump formation whereas the latter leads to balling. These discrepancies indicate that the average heat extraction alone is insufficient to characterize melt-pool stability.

To capture the effect of temporal variability, we define a normalized fluctuation intensity of interfacial heat flux as $\delta(q_{IA}) = \sigma(q_{IA})/q_{IA}$, where $\sigma(q_{IA})$ denotes the temporal standard deviation of $q_{IA}(t)$. Mapping all processing conditions into the $q_{IA} - \delta(q_{IA})$ space reveals a clear separation of morphological regimes (Fig. 5.1(c)). Combined with Fig. 5.1(a)-(c), both hump and balling are generally observed in regimes characterized by relatively large fluctuation intensity of q_{IA}, indicating that strong temporal variability in interfacial heat transfer is closely associated with melt-pool instability. However, an exception is observed at 100 W and 0.5 m/s, where the fluctuation intensity is comparable to that of unstable conditions, yet a stable melt track is obtained. This apparent inconsistency can be understood by considering the magnitude of $\overline{q_{IA}}$. Under this condition, the average interfacial heat flux is relatively low, corresponding to a reduced overall thermal driving force within the melt pool. As a result, melt flow remains moderate and the amplification of perturbations is suppressed, even in the presence of comparable fluctuation levels. In contrast, conditions such as 200 W at 1 m/s and 2 m/s, although exhibiting higher $\overline{q_{IA}}$, show relatively small fluctuation intensity and therefore maintain stable track formation.

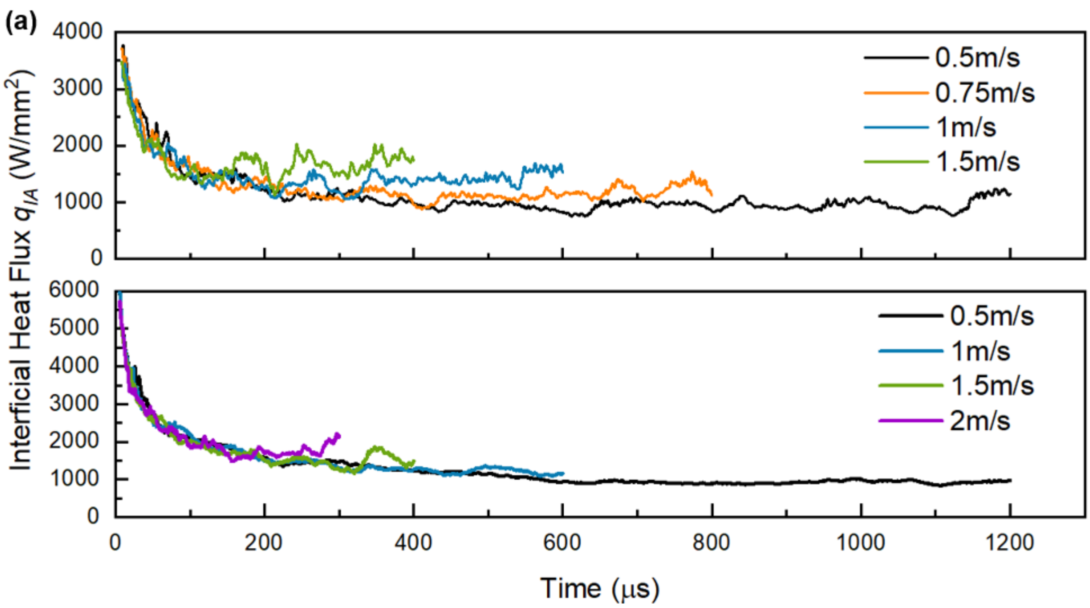

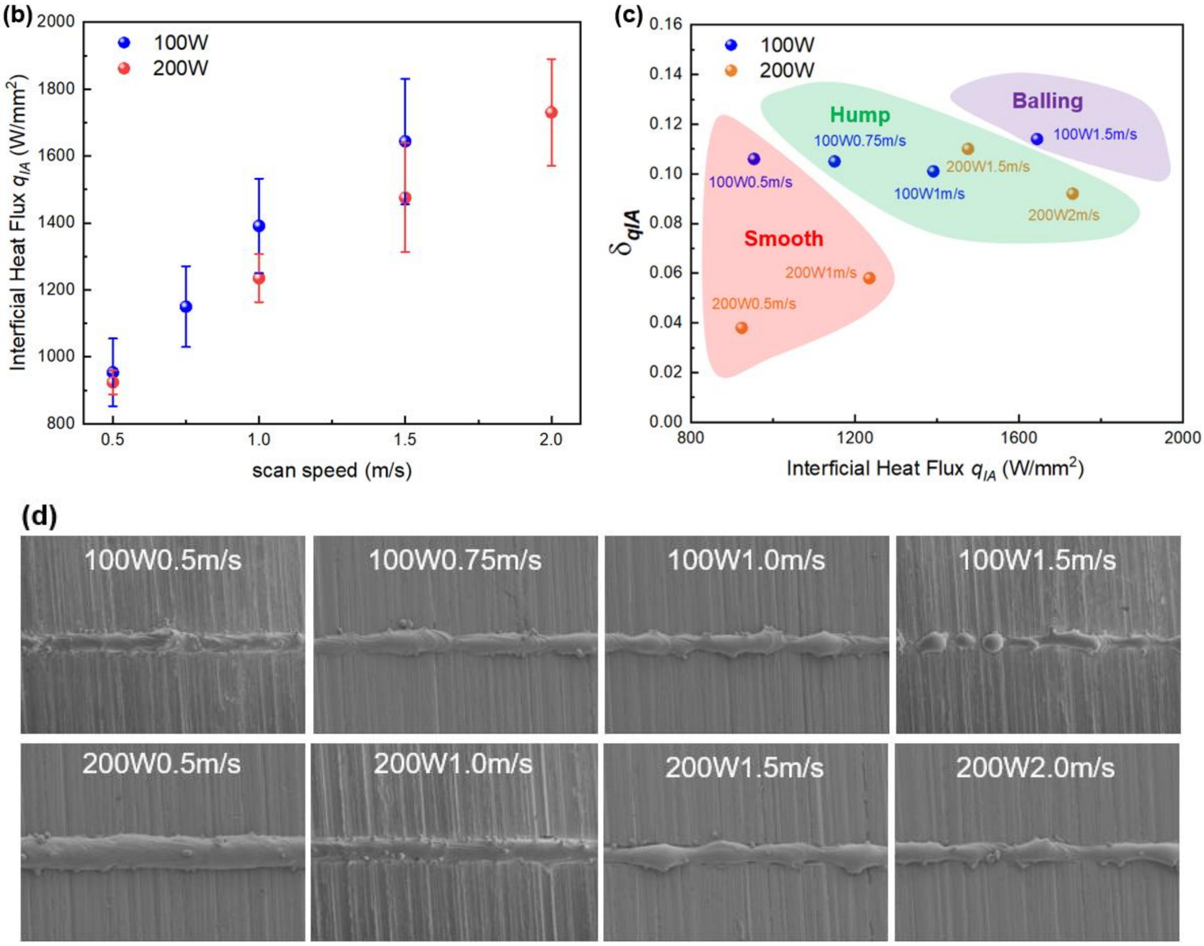

Fig. 5.1. Time-resolved interfacial heat flux as a governing parameter for melt-pool stability. (a) Temporal evolution of interfacial heat flux $q_{IA}(t)$ under varying scan speeds and laser powers, revealing intrinsic fluctuations associated with dynamic melt-pool behavior. (b) Averaged interfacial heat flux q_{IA} and normalized fluctuation intensity $\delta(q_{IA})$, highlighting that heat flux magnitude alone does not uniquely determine melt-track morphology. (c) Regime map in the $q_{IA} - \delta(q_{IA})$ space, demonstrating that the combined metrics of magnitude and fluctuation provide a unified criterion for distinguishing smooth, hump, and balling regimes. (d) Experimental melt-track morphologies corresponding to the mapped conditions.

The resulting $q_{IA} - \delta(q_{IA})$ map thus provides a compact representation of melt-track stability. Smooth tracks correspond to regimes with low heat extraction and limited temporal variability, whereas increasing both the magnitude and fluctuation of interfacial heat flux promotes the transition toward hump and balling defects. In this sense, q_{IA} can be interpreted as an effective thermal control parameter that encapsulates both the intensity and stability of heat extraction at the melt–substrate interface.

Taken together, these results reveal that melt-pool morphology is governed by time-resolved interfacial heat flux, rather than by energy input alone. The combined metrics of averaged heat flux and fluctuation intensity provide a physically grounded framework for predicting morphological transitions and defect formation, establishing a direct link between transient thermal transport and melt-pool stability.

5.3 Spatial Distribution of Temperature Gradient and Its Role in Interfacial Heat Transfer Stability

The interfacial heat flux q_{IA} can be represent by the area-weighted temperature gradient along the solid-liquid interface, indicating that it is primarily determined by the spatial distribution of local temperature gradients. To elucidate the physical origin of the q_{IA}-based stability framework, we examine how the spatial distribution of temperature gradients governs interfacial heat transfer within the melt pool.

At low scan speed (100 W, 0.5 m/s; Fig. 5.2a), a relatively uniform and low temperature gradient extends from the front to the rear of the melt pool. As the scan speed increases to 1.0 m/s (Fig. 5.2b), the overall temperature gradient increases, and the distribution becomes progressively localized near the front region, while the rear region exhibits reduced gradients. This indicates the emergence of spatially non-uniform heat extraction, where thermal transport becomes increasingly dominated by the leading edge. At higher scan speed (100 W, 1.5 m/s; Fig. 5.2c), the overall temperature gradient becomes significantly elevated, and the localization becomes more pronounced. The temperature gradient is strongly concentrated at the front and significantly depleted at the rear, leading to severe spatial inhomogeneity in interfacial heat flux. In Fig. 5.2(d)-(f), a similar trend is also observed under higher laser power (200 W) with increasing scan speed. This explains why q_{IA} increases monotonically with scan speed.

Regarding the fluctuation intensity $\delta(q_{IA})$, we infer that it is primarily related to Marangoni (Ma) circulation. When a well-developed Ma circulation exists, heat can be more uniformly redistributed throughout the melt pool, thereby maintaining melt pool stability. For example, although the q_{IA} at 200 W and 1 m/s is higher than that at 100 W and 0.75 m/s, the former condition, similar to 200 W and 0.5 m/s, exhibits a well-developed and nearly closed Ma circulation. As a result, $\delta(q_{IA})$ remains small, and the melt pool quality is good, leading to a smooth track morphology.

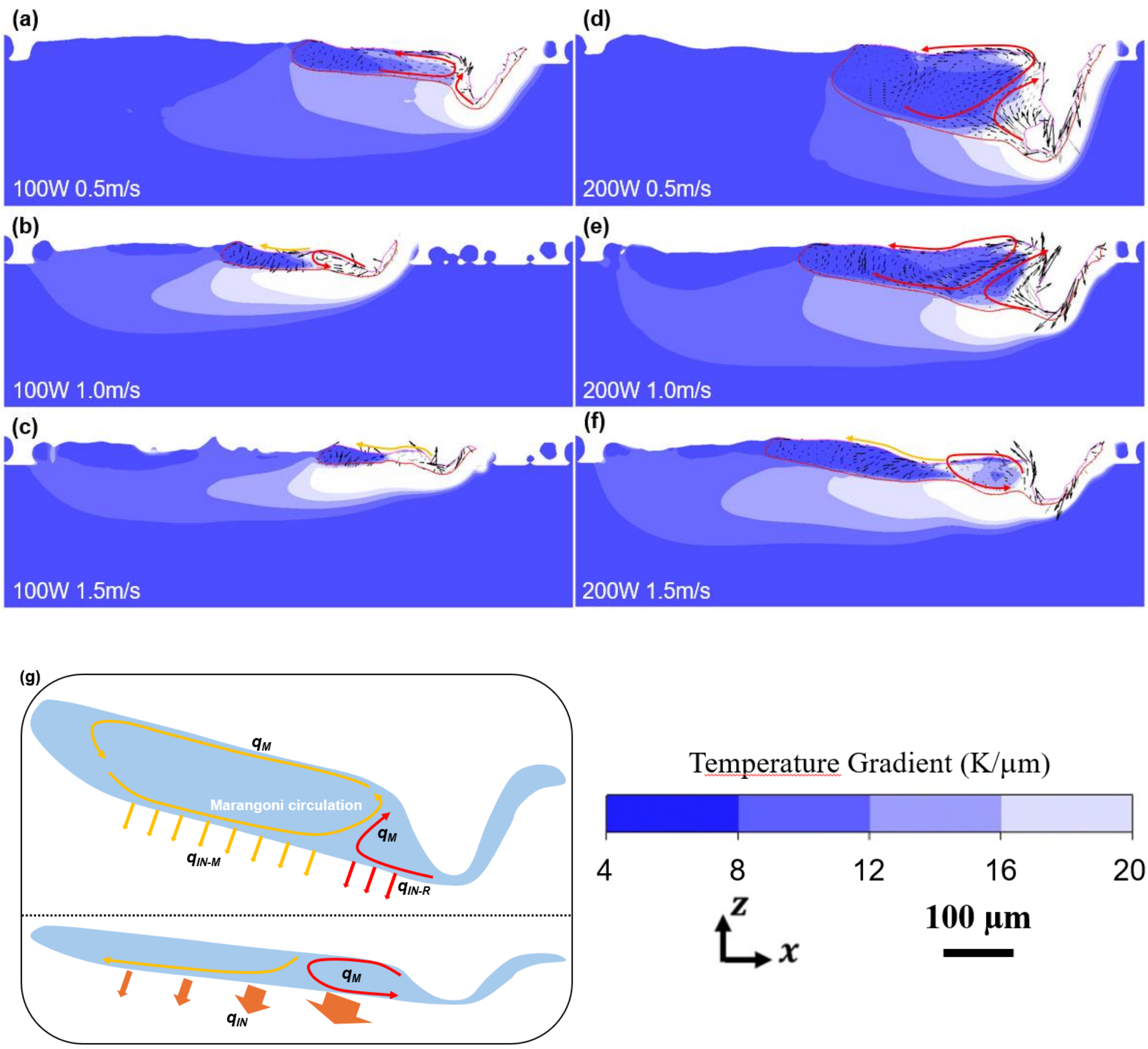

Fig. 5.2. Temperature gradient distribution and its impact on interfacial heat transfer and melt pool stability. (a–f) Evolution of temperature gradient distribution at 100 W and 200W with flow dynamics at different scan speeds. (g) Conceptual schematic illustrating the relationship between temperature gradient distribution, Marangoni-driven flow, and interfacial heat transfer stability. Stable melt pools are associated with either low gradient magnitude or effective heat redistribution via coherent circulation, whereas strong localization without recirculation leads to instability.

In contrast, the reason why 100 W and 0.5 m/s also exhibits a smooth track is fundamentally different from the above high-power cases. Under this condition, Ma circulation only exists locally in the front region where the temperature gradient is relatively high, and its spatial extent is limited. Therefore, the overall fluctuation intensity of the melt pool is not low. Instead, the stability is mainly maintained by the relatively low temperature gradient at the solid–liquid interface, corresponding to a low q_{IA}, which keeps the melt pool in a marginally stable smooth state. As the scan speed slightly increases to 0.75 m/s, the system transitions into the hump regime.

Typical contrasting cases to 100 W and 0.5 m s−1−1 are 100 W and 1 m s−1−1, as well as 200 W and 1.5 m/s. Although localized Ma circulation still exists near the high-temperature region close to the laser interaction zone under these conditions, and the values of $\delta(q_{IA})$ are relatively comparable, the spatial non-uniformity of the temperature gradient along the interface is significantly higher. In addition, the overall interfacial temperature gradient is large, resulting in a high q_{IA}. These factors promote rapid localized solidification, ultimately leading to the formation of hump defects.

A typical balling case is observed at 100 W and 1.5 m/s. In this regime, the temperature gradient across the entire solid–liquid interface becomes extremely high, resulting in a very large q_{IA}. Meanwhile, effective Ma circulation is largely absent, leading to a relatively large $\delta(q_{IA})$ and poor melt pool stability. Furthermore, a significant difference exists between the temperature gradients at the front and rear regions of the melt pool (as shown in Fig. 5.2), where the front region reaches approximately 20 K/μm, while the rear is around 4 K/μm. Under the action of this strong surface tension gradient, molten material flows from the front toward the rear, accumulates, and rapidly solidifies, ultimately forming balling defects.

A schematic illustration of thermal transport within the melt pool is shown in Fig. 5.2(g). When the overall interfacial temperature gradient is relatively low and Marangoni circulation exists only locally near the front region (e.g., 100 W, 0.5 m/s), heat redistribution across the melt pool remains limited. Under such conditions, the thermal field lacks global connectivity, and the melt pool operates in a marginally stable state primarily sustained by the low level of interfacial heat flux. As the temperature gradient increases, a strong and closed Marangoni circulation can be established (e.g., 200 W, 0.5 m/s and 1 m/s), enabling efficient and continuous heat transport from the front to the rear of the melt pool. This coherent flow structure promotes a more uniform thermal field, suppresses local thermal accumulation, and stabilizes interfacial heat transfer, thereby maintaining melt pool stability.

Taken together, these results demonstrate that melt pool stability is governed by the coupled effect of the magnitude and spatial organization of temperature gradients. While the magnitude of the interfacial temperature gradient determines the overall level of heat extraction q_{IA}, the presence and integrity of Marangoni circulation control the effectiveness of heat redistribution and thus the fluctuation intensity $\delta(q_{IA})$. A low but weakly connected thermal field leads to marginal stability, whereas a strong and coherent circulation stabilizes the melt pool despite higher heat flux. In contrast, when temperature gradients become highly localized without effective recirculation, thermal transport becomes imbalanced, ultimately triggering morphological instabilities such as hump and balling.

5.4 Thermal transport–flow coupling governs pore formation and evolution

As indicated in Fig. 5.1(a) and (b), at lower scanning speeds, the interfacial heat flux q_{IA} at the melt pool interface is significantly reduced, making the molten region more prone to overheating. This thermal accumulation increases the likelihood of frequent vaporization reactions at the liquid surface, leading to unstable keyhole oscillations and the formation of gas bubbles. Fig. 5.3 (a) presents the time-resolved evolution of average pressure on the keyhole interface during laser scanning. While many time points exhibit pronounced pressure fluctuations—including sharp rises and drops-only specific instances result in the actual formation of porosity defects. This indicates that a drop in keyhole surface pressure is not the decisive factor for pore formation; rather, it increases the likelihood of keyhole collapse and subsequent bubble entrapment.

To further investigate the underlying mechanism of pore formation from a heat transfer perspective, we analyzed the time evolution of net heat accumulation in the melt pool. Fig. 5.3(b) shows the variation of $\boldsymbol{q_{acc}}$, defined as the laser energy input minus the combined losses due to interfacial conduction and vaporization. The results reveal that pores are more likely to form when the net heat accumulation is minimal or even negative. This can be attributed to two key factors: first, the reduction in recoil pressure under low thermal accumulation conditions facilitates keyhole collapse, leading to bubble entrapment. Second, the solid-melt contact area dynamically adjusts in response to interfacial heat flux. When $\boldsymbol{q_{acc}}$ is low or negative, the temperature gradients across the melt pool are relatively small, requiring a larger area to recede during the solidification front adjustment. If a bubble is present along this receding interface, it increases the probability of pore formation due to bubble-interface contact.

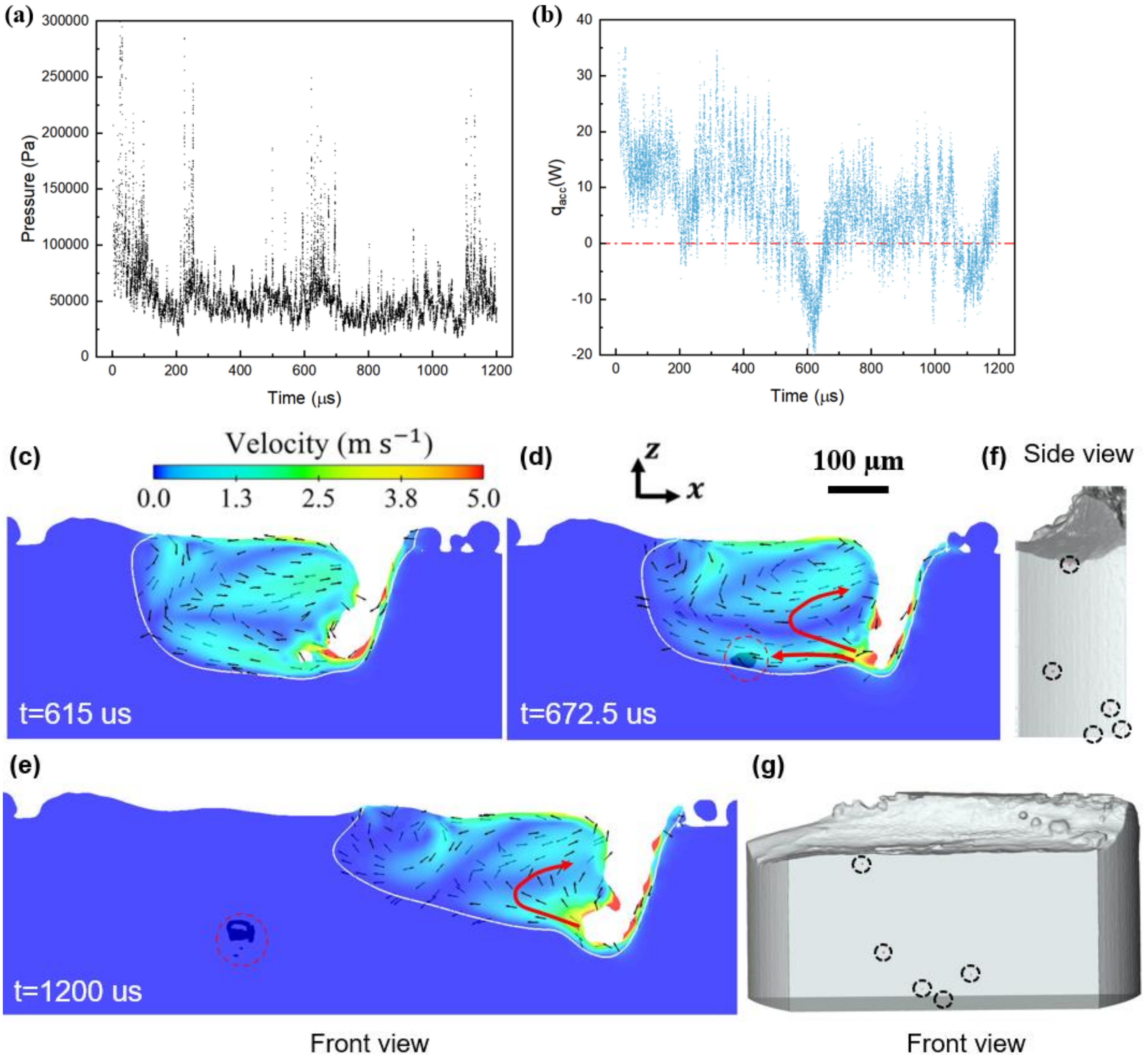

Fig. 5.3. Pore formation governed by sustained thermal depletion and melt-flow-driven bubble transport. (a) Temporal evolution of keyhole interfacial pressure, showing frequent fluctuations associated with vaporization dynamics. (b) Net heat accumulation q_{acc} as a function of time, where sustained negative values correspond to periods of thermal depletion. (c–e) CFD simulations showing the evolution of bubble formation and transport. At t=615μs (c), a bubble nucleates in the central region of the melt pool. At t=672.5μs (d), the bubble is transported away from the center toward the opposite side under a weakened and fragmented Marangoni flow field. At t=1200μs (e), the bubble becomes trapped within the solidifying region, forming a pore. (f–g) X-ray computed tomography (CT) results showing pore distribution. The side view (f) and front view (g) reveal pore localization away from the central axis, consistent with the lateral displacement predicted by the simulations.

Fig. 5.3(c) captures such an event at 615 µs, where negative q_{acc} leads to bubble generation and lateral displacement from the center, followed by its subsequent rearward movement at

672.5 μs (Fig. 5.3(d)), eventually resulting in pore entrapment. Moreover, since Marangoni convection bridges the thermal and flow fields, reduced net heat accumulation also diminishes the temperature difference between the front and rear surfaces of the melt pool, thereby weakening the surface tension-driven flow. As a result, the melt pool becomes more flattened and concave, with insufficient upward convection from the bottom. This favors the rearward transport of bubbles toward the melt pool boundary, increasing their likelihood of being trapped—an effect reflected in the disruption of Marangoni circulation, which leads to a bifurcated velocity field, weakened upward flow, and bubble transport following the bottom rearward flow (Fig. 5.3(c)). By contrast, at 1100 μs, although a transient negative $\boldsymbol{q_{acc}}$ is also observed, the magnitude and duration of heat loss are smaller. Marangoni convection remains sufficiently active to sustain upward circulation, as indicated by the uniform, upward-sloped thermal gradient layers. The bubble is thus redirected toward the keyhole region and ultimately reduce pore formation probability, as shown in Fig. 5.3(e).

The simulated pore behavior is further validated by experimental observations. The CT reconstruction shown in Fig. 5.3(f) (side view) and Fig. 5.3(g) (front view) reveals pore distributions located away from the central axis, consistent with the lateral displacement observed in the simulations. The agreement between CFD-predicted bubble transport paths and experimentally observed pore locations confirms that pore formation is governed by flow-driven transport under thermally weakened conditions.

Taken together, these results demonstrate that pore formation is governed by a coupled thermal-flow mechanism, in which net heat accumulation regulates Marangoni convection and thereby determines bubble transport and entrapment. Sustained thermal depletion reduces temperature gradients and weakens surface-tension-driven flow, disrupting global circulation and preventing bubble recirculation, so that bubbles are transported away from the keyhole and trapped at the solidification front. In contrast, when thermal depletion is transient, Marangoni circulation remains sufficiently strong to recirculate and reabsorb bubbles, suppressing pore formation. Thus, Marangoni convection serves as a critical bridge linking thermal transport and fluid motion, ultimately controlling defect evolution during keyhole-based additive manufacturing.

5.5 Effect of substrate preheating on thermal transport and defect formation

Based on the understanding of heat transfer mechanisms that govern the influence of process parameters on melt pool behavior, we further investigated the effect of substrate preheating. Although prior studies have explored the impact of preheating on melt pool evolution and resulting track morphology, they primarily focused on comparing different preheating temperatures without fully elucidating the underlying mechanisms by which preheating alters melt pool dynamics [167][168].

As shown in Fig. 5.4(a), preheating to 773 K leads to a clear reduction in the averaged interfacial heat flux q_{IA} at both scan speeds (0.5 m/s and 1.5 m/s). In contrast, the fluctuation intensity δ_{qIA} remains nearly unchanged. This indicates that preheating primarily lowers the overall level of interfacial heat transfer, while the relative fluctuation behavior of the melt pool is largely preserved. In other words, preheating modifies the thermal baseline of the system without fundamentally altering its intrinsic instability characteristics.

As indicated by Fig. 5.1(c), after preheating to 773 K, the processing point (200 W, 1.5 m/s) shifts from the humping regime to the smooth regime, resulting in the suppression of hump formation. This transition is confirmed by the experimental observations in Fig. 5.4(b), where the melt track exhibits significantly improved continuity and surface quality. This agreement further supports the predictive capability of the proposed $q_{IA} - \delta(q_{IA})$ framework. To gain deeper insight into the spatial redistribution of heat transfer, Fig. 5.4(c) presents the temperature gradient distributions along the melt pool surface and the solid-liquid interface at the centre cross-section under 200 W and 1.5 m/s. After preheating, the temperature gradients become more uniform and are significantly reduced along both boundaries. This improvement can be attributed to the elevated baseplate temperature, which decreases the thermal gradient between the melt pool and the substrate. The mechanism is similar to that observed under the condition of 100 W and 0.5 m/s, where a relatively uniform and low temperature gradient extends from the front to the rear of the melt pool.

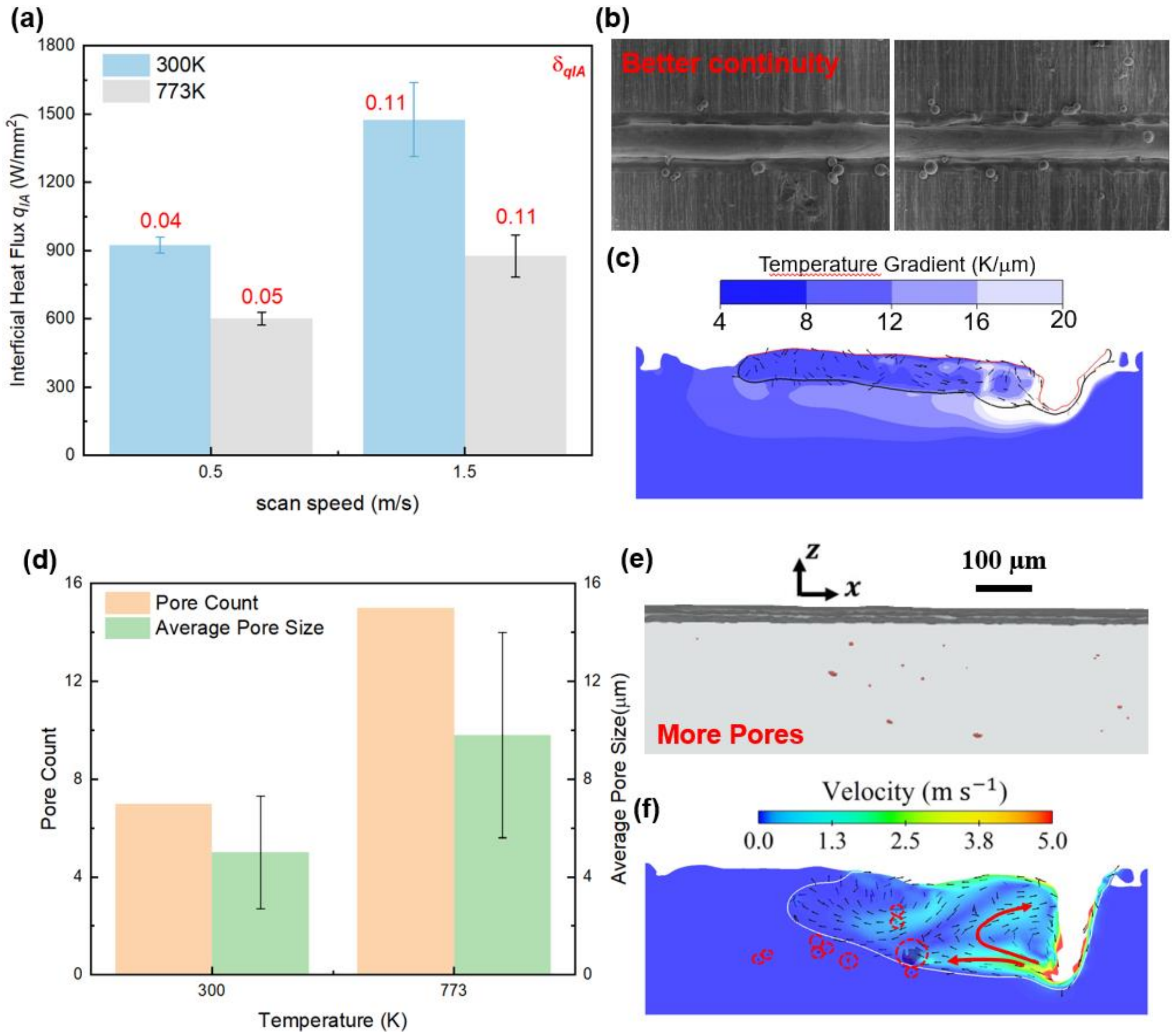

Fig. 5.4 Regime-dependent influence of substrate preheating on interfacial heat transfer, melt-pool stability, and pore formation. (a) Averaged interfacial heat flux q_{IA} and fluctuation intensity $\delta(q_{IA})$ at 200 W for scan speeds of 0.5 and 1.5 m/s under non-preheated (300 K) and preheated (773 K) conditions. Preheating reduces the magnitude of q_{IA}, while the relative fluctuation intensity remains nearly unchanged. (b) Surface morphology at 200 W and 1.5 m/s, showing improved track continuity and suppression of hump defects after preheating. (c) Temperature gradient distribution along the melt pool surface and solid–liquid interface at 200 W and 1.5 m/s, showing more uniform thermal distribution under preheated conditions. (d) Quantitative statistics of pore number and size distribution at 200 W and 0.5 m/s, showing increased pore frequency and enlarged pore size after preheating. (e) CT reconstruction at 200 W and 0.5 m/s, revealing a higher pore density under preheated conditions. (f) CFD results at 200 W and 0.5 m/s, showing weakened Marangoni-driven flow and reduced melt-pool recirculation under preheating, leading to bubble transport toward the rear and subsequent entrapment.

The effect of preheating on pore formation under low scan speed conditions is shown in Fig. 5.4(d), which quantifies the pore number and size distribution based on the CT results in Fig. 5.4(e) (200 W, 0.5 m/s). Under non-preheated conditions (300 K), 7 pores are observed with an average size of 5 μm. In contrast, preheating increases the pore number to 15 and enlarges the average size to 9.8 μm, accompanied by a broader size distribution. And a higher pore density is clearly observed after preheating, indicating that preheating promotes porosity formation in this regime. This also implies that an excessively low q_{IA} in the $q_{IA} - \delta(q_{IA})$ framework tends to promote pore formation. Based on the CFD results shown in Fig. 5.4(f)**,** the underlying mechanisms can be summarized as follows:

1. **Enhanced overheating**: Preheating raises the baseline temperature of the substrate and melt pool, making the molten metal more susceptible to frequent vaporization. This leads to unstable keyhole dynamics, where repeated collapse and recoil events increase the likelihood of bubble formation.

2. **Negative or minimal net heat accumulation**: Under preheated conditions, when net heat input $\boldsymbol{q_{acc}}$ is very small or even negative, recoil pressure weakens and the keyhole becomes more prone to collapse, entrapping gas bubbles. Additionally, the contact area between the melt pool and the solid substrate must adjust in response to interfacial heat flux. Since preheating reduces the overall temperature gradient, the interface must recede over a larger area to reestablish thermal equilibrium. This increases the probability of contact between the shrinking interface and any existing bubbles, thereby promoting pore formation.

3. **Weakened Marangoni convection**: Although total heat loss remains roughly unchanged, the enlarged melt pool volume under preheating results in reduced temperature gradients. When net heat accumulation becomes insufficient, Marangoni flow is significantly suppressed. The melt pool surface becomes more flattened and concave, and the bottom flow lacks the upward momentum needed to recirculate bubbles. As a result, bubbles are more likely to be dragged rearward and trapped at the solidification boundary. In contrast, under non-preheated conditions, stronger Marangoni flow can redirect bubbles back into the keyhole, reducing porosity.

These findings indicate that preheating is not suitable for low scan speed conditions, as it intensifies porosity formation. However, for high scan speeds that typically suffer from lack-of-fusion or humping defects under the same power condition, preheating effectively reduces thermal gradients, promotes more uniform heat redistribution, and improves melt pool stability, thereby suppressing hump formation.

5.6 Conclusion

This chapter establishes that melt-pool stability and defect formation in LPBF are governed by the dynamic and spatially non-uniform nature of heat transfer at the melt–substrate interface, rather than by global energy input alone. By introducing the area-averaged interfacial heat flux q_{IA} and its normalized fluctuation intensity $\delta(q_{IA})$, we show that the transition from smooth tracks to humping and balling defects is determined by the combined elevation of both the mean heat extraction level and its temporal variability. A key insight is that a well-developed, closed Marangoni circulation can maintain low $\delta(q_{IA})$ even under higher q_{IA}, thereby preserving melt-pool stability; conversely, when Marangoni flow is weak or spatially fragmented, even moderate q_{IA} can trigger instabilities.

Pore formation follows a distinct thermal-flow mechanism. It is promoted when net heat accumulation q_{acc} becomes minimal or negative, which reduces recoil pressure, flattens the melt pool, and disrupts the upward branch of Marangoni convection. Under such conditions, bubbles are transported rearward along the bottom and become trapped at the solidification front. Transient thermal depletion, if insufficient to break global circulation, allows bubbles to be recirculated back to the keyhole and reabsorbed, suppressing porosity.

Substrate preheating reduces q_{IA} without significantly altering $\delta(q_{IA})$. Its effect is regime-dependent: at high scan speeds, it lowers temperature gradients and suppresses humping; at low scan speeds, it exacerbates overheating, and weakens Marangoni flow, thereby increasing pore formation. These findings provide a unified, physically grounded framework—centered on interfacial heat flux, its fluctuations, and the integrity of Marangoni circulation—for predicting morphological transitions and guiding process optimization in LPBF.

Chapter 6. Spattering dynamics mechanism

6.1 Introduction

In the LPBF process, the interaction between the laser beam and the powder bed generates complex multiphase flow phenomena that significantly influence the quality, repeatability, and stability of the printed components. Among these, particle spattering-referring to the ejection of powder or molten material from the process zone-is a critical event that affects powder bed uniformity, melt track integrity, and defect formation. Despite extensive research on melt pool dynamics and laser-material interactions, the underlying mechanisms of spatter formation and evolution remain only partially understood due to their transient, stochastic, and multi-physics nature.

Spatter in LPBF is typically categorized into two main types: melt droplet spatter and powder particle spatter. Melt droplets are primarily driven by recoil pressure, Marangoni convection, and keyhole instabilities, whereas powder particles are ejected due to vapor plume entrainment and aerodynamic drag forces. These phenomena vary markedly with process parameters such as scanning speed, laser power, and powder characteristics, introducing significant complexity into spatter prediction and control.

This chapter presents a comprehensive mechanistic investigation of spattering behavior, combining high-speed in situ imaging, morphological analysis, and numerical modeling to elucidate the particle dynamics under varying processing conditions. Section 6.2 analyzes powder particle spattering induced by vapor recoil and entrainment, emphasizing the role of vapor flow directionality and transient heating. Section 6.3 explores how scan speed influences the angular distribution and deposition location of spattered particles, revealing a deterministic shift from forward to rearward ejection trajectories. Section 6.4 investigates the onset of particle mobility by examining frictional resistance at the particle-substrate interface, highlighting the criteria required for detachment initiation. In Section 6.5, attention shifts to detachment dynamics in both isolated and agglomerated particles, uncovering how cohesive forces and momentum exchange govern lifting thresholds. Section 6.6 further refines the framework by considering melt pool wettability, demonstrating that particle escape or incorporation is tightly linked to melt pool geometry and surface energy conditions. Finally, Section 6.7 synthesizes these findings and outlines the implications for process stability, powder reuse, and spatter suppression strategies.

By integrating experimental observations with theoretical model, this chapter establishes a multi-physics framework to understand and quantify spattering behavior. The insights gained here not only advance the fundamental understanding of powder dynamics in LPBF but also provide a basis for predictive control of defect formation and process optimization in future builds.

6.2 Powder particle spattering induced by vapor

Spatter in LPBF is broadly categorized into melt droplet spatter and powder particle spatter. As shown in Fig. 6.1(a), a schematic illustration differentiates between these two types based on their origin and ejection mechanism. While melt droplet spatter-resulting from melt pool instabilities such as recoil pressure and Marangoni-driven convection-is well known, a significant proportion of spatter events in LPBF processes involve unfused or partially heated powder particles [46]. These particles are primarily ejected due to entrainment by the recoil vapor jet, which is generated by rapid surface vaporization during laser irradiation. The high-velocity vapor jet induces a localized gas flow field that displaces surrounding powder particles before they can be incorporated into the melt pool. In most cases, these particles remain in the solid state and are carried away passively by the vapor-induced flow. However, at elevated energy densities or near the laser beam periphery, some powder particles may experience transient thermal exposure, leading to surface softening or partial melting. Such particles can be ejected with increased kinetic energy and appear as visible, spark-like trajectories in high-speed imaging, indicating thermally driven spatter behavior. Powder particle spatter induced by vapor jet entrainment is typically concentrated around scan track edges and overhanging features, reflecting a complex interplay among vapor dynamics, local temperature gradients, and particle–gas interactions.

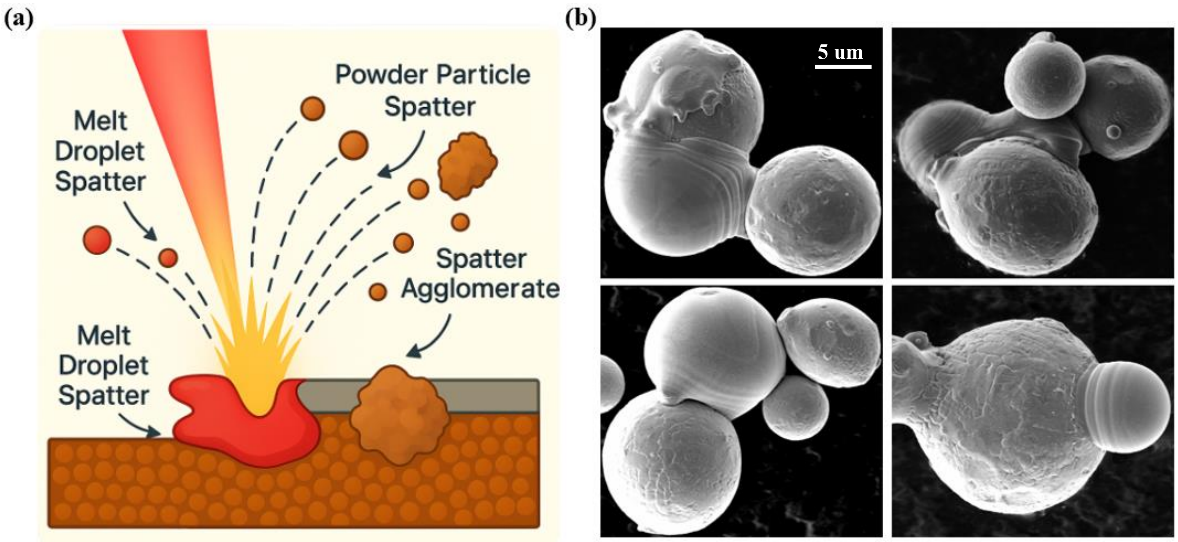

Fig. 6.1. Classification and morphological characteristics of spatter in LPBF. (a) Schematic illustration of melt droplet spatter and powder particle spatter based on ejection mechanisms (original). (b) SEM images showing the

morphologies of spatter particles collected from our experiments.

To further understand the physical characteristics of these ejected particles, Fig. 6.1(b) illustrates the morphologies of spatter particles were examined using scanning electron microscopy (SEM). As shown in Fig. 3.1(a), the virgin powder exhibits a predominantly spherical shape with smooth surfaces and minimal satellites, which is typical for gas-atomized powders designed for LPBF. This morphology ensures good powder flowability and packing density, which are essential for uniform layer deposition and consistent laser-material interaction. In contrast, the spatter particles generated during the LPBF process display a wide variety of irregular morphologies that deviate significantly from the original powder. Several distinct types were observed:

(i) Agglomerated particles, resulting from the partial or complete melting and subsequent coalescence of multiple particles in-flight, were frequently observed. These structures are typically larger and exhibit irregular, fused boundaries.

(ii) Partially melted and fused clusters with asymmetric solidification fronts and rough surfaces suggest rapid non-equilibrium solidification during ejection.

(iii) Satellite-like formations, where smaller particles adhere to larger ones via localized melting or physical impact, were evident in several cases.

(iv) Elongated or deformed particles with tail-like features were identified, likely formed by directional momentum during high-speed ejection followed by rapid cooling.

The formation of such spatter morphologies is attributed to complex thermofluid dynamics during the laser–powder interaction, including recoil pressure, vapor jet entrainment, and in-flight collision events. These non-spherical and thermally altered particles pose several risks to process stability: they may degrade powder bed uniformity, interfere with laser energy absorption, and remain partially unprocessed, leading to inclusion-type defects or porosity in the consolidated material. Furthermore, if recycled into the feedstock, these particles can accumulate and progressively deteriorate powder quality in subsequent builds.

Also, high-velocity spatter particles in LPBF are known to have detrimental effects on both process stability and part integrity. These particles can contaminate optical elements, disturb powder bed uniformity, and trigger secondary ejection events by impacting surrounding powder. Furthermore, high ejection velocities are often symptomatic of excessive vapor recoil pressure or melt pool instability, and thus serve as potential indicators for in-situ monitoring of process anomalies. In addition, they reduce powder recovery efficiency and increase the likelihood of inclusion defects in subsequent layers. Given their significant impact, understanding how spatter velocity and directionality evolve with varying scanning speeds is crucial for both process optimization and defect mitigation. Fig. 6.2 presents high-speed imaging of spatter behavior under a constant laser power of 100 W and varying scanning speeds of 0.1 m/s, 0.5 m/s, and 1.0 m/s. The laser scanning direction is from left to right, as indicated by the blue arrow in the figure. Spatter trajectories were tracked using consecutive high-speed frames, and particle velocities were estimated by measuring the displacement of visible particle streaks between frames and dividing by the known frame interval.

At a scanning speed of 0.1 m/s, the spatter exhibited a highly scattered ejection pattern, with visible particle trajectories oriented in both forward and lateral directions relative to the scanning direction. Measured spatter velocities ranged from 2.9 to 8.1 m/s, and many particles displayed bright, thick streaks—indicative of high thermal energy and relatively large particle sizes. The vapor plume was observed to tilt forward by approximately 15°, suggesting that at low scan speeds, the long laser–material interaction time induced excessive local vaporization and melt pool instability. Consequently, the recoil plume lacked directional confinement and spread preferentially toward the front and sides of the melt pool, entraining particles before full absorption into the melt.

When the scanning speed increased to 0.5 m/s, the plume direction shifted rearward, with particle ejection primarily aligned within 20°-30° behind the scan axis. This directional consolidation reflects the increased influence of laser head motion on vapor flow orientation. The measured spatter velocities reached up to 9.2 m/s, and the trajectories appeared more collimated compared to the low-speed case. These trends indicate that higher scan speeds promote a more stable melt pool and more consistent vapor jet structure, favoring entrainment and ejection of mid-sized particles with improved energy coupling efficiency.

At 1.0 m/s, spatter directions became increasingly rearward and vertically focused, while visible streaks were thinner and dimmer-implying smaller particle sizes and lower thermal excitation. Estimated ejection angles ranged from 30° to 40° behind the laser path, consistent with a highly collimated, backward-directed vapor jet. The relatively narrow range of spatter velocities (5.5-7.1 m/s) further suggests that particle entrainment was dominated by aerodynamic drag rather than thermal propulsion. The high scan speed reduces the interaction time between laser and powder, limiting energy transfer and resulting in predominantly cold-state particle ejection.

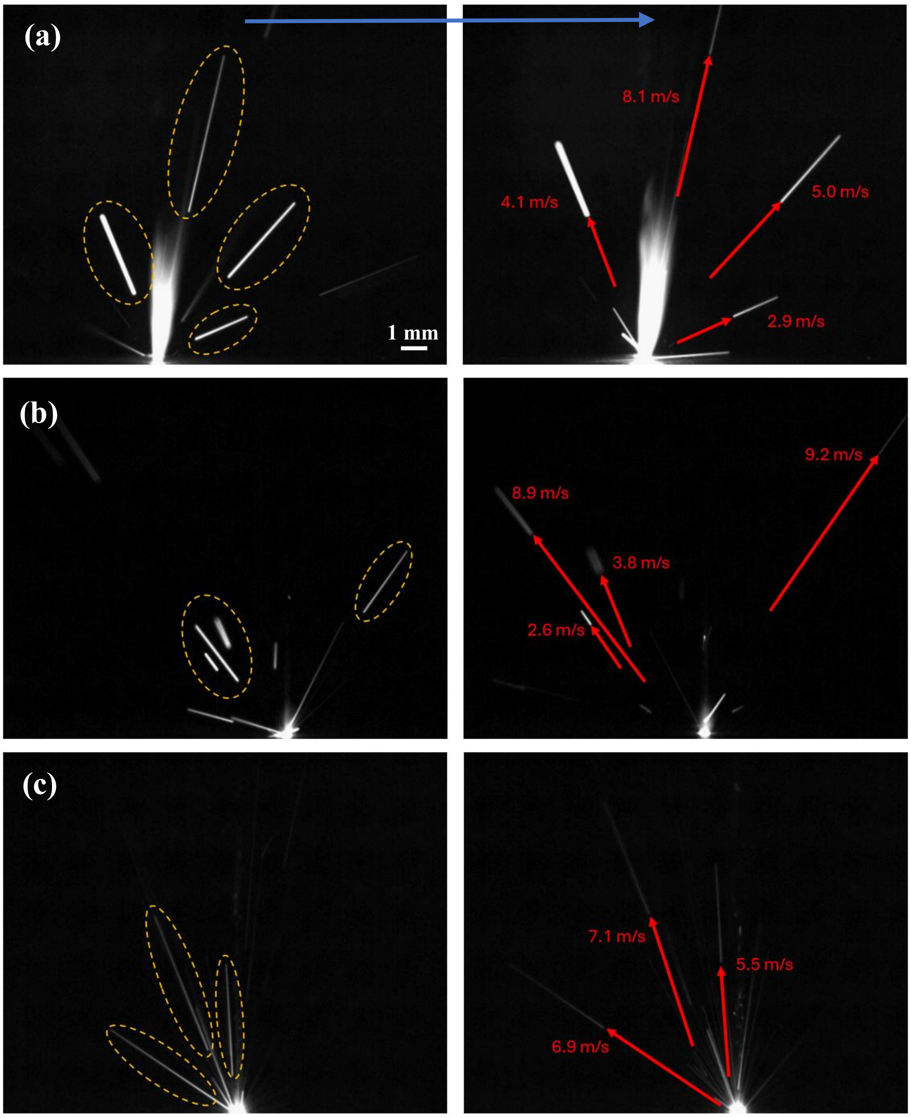

Fig. 6.2. High-speed imaging analysis of spatter behavior at a constant laser power of 100 W and different scanning speeds. The laser scanning direction is from left to right. (a) Spatter trajectories at 0.1 m/s. (b) Spatter trajectories at 0.5 m/s. (c) Spatter trajectories at 1.0 m/s. Red arrows indicate representative particle velocities estimated from frame-to-frame displacement.

Overall, the high-speed observations indicate that increasing scanning speed leads to a gradual shift in the dominant spatter direction from forward and lateral scattering toward a more rearward-oriented and collimated ejection pattern. This trend suggests that laser scanning speed influences the orientation and confinement of the vapor jet, thereby affecting spatter trajectories during the LPBF process.

6.3 Influence of scanning speed on spatial distribution of spatter

In LPBF, the spatial behavior of spatter plays a critical role in influencing part quality, powder bed uniformity, and defect formation across layers. Among the various process parameters, scan speed is known to affect melt pool thermodynamics and plume dynamics, yet its influence on the spatial landing distribution of spattered particles remains insufficiently characterized under controlled energy input conditions.

In this work, a systematic investigation was conducted to assess the impact of scan speed on spatter ejection and deposition under constant laser power (100 W). By integrating numerical simulation of melt pool thermofluidic fields with high-speed in situ imaging, we demonstrate that variations in scan speed induce systematic transitions in both melt pool morphology and recoil vapor flow direction, which in turn modulate the angular trajectory and final landing positions of spattered particles.

As illustrated in Fig. 6.3, increasing the scanning speed from 0.1 m/s to 1.0 m/s results in a progressive shift in spatter deposition from a forward-leaning to a rearward-leaning distribution. Fig. 6.3(a) shows the result from the first experiment, while Fig. 6.3(b) presents the result from a repeated trial, confirming the observed trend. At low scan speeds, spatter particles are predominantly ejected along steep, upward or forward-inclined trajectories and tend to deposit ahead of the laser scan path. As the scan speed increases, these trajectories gradually flatten and rotate backward, causing the spatter to accumulate near or even behind the trailing edge of the melt pool. This evolution reflects a systematic change in angular momentum transfer from the recoil plume to the ejected particles, ultimately altering the spatial footprint of spatter accumulation around the processing zone. This transition is primarily attributed to the gradual change in melt pool geometry from a deep, keyhole-like shape to a shallower, basin-like configuration, accompanied by a rearward shift in the peak temperature location, which in turn causes the recoil vapor jet direction to rotate backward, as illustrated in Fig. 6.4(a). At low scan speed (0.1 m/s), the melt pool exhibits a deeper and narrower profile with a leading-edge temperature maximum, giving rise to a predominantly forward-directed recoil plume. This configuration facilitates the ejection of particles toward the laser's approach direction. In contrast, higher scan speeds (e.g., 0.5-1.0 m/s) produce a more flattened melt pool with rearward-shifted thermal centroids, thereby redirecting the recoil flow toward the laser trailing edge. This rotation in recoil pressure orientation results in spatter trajectories that lean backward, evidencing a clear correlation between scan speed, melt pool asymmetry, and plume vector direction.

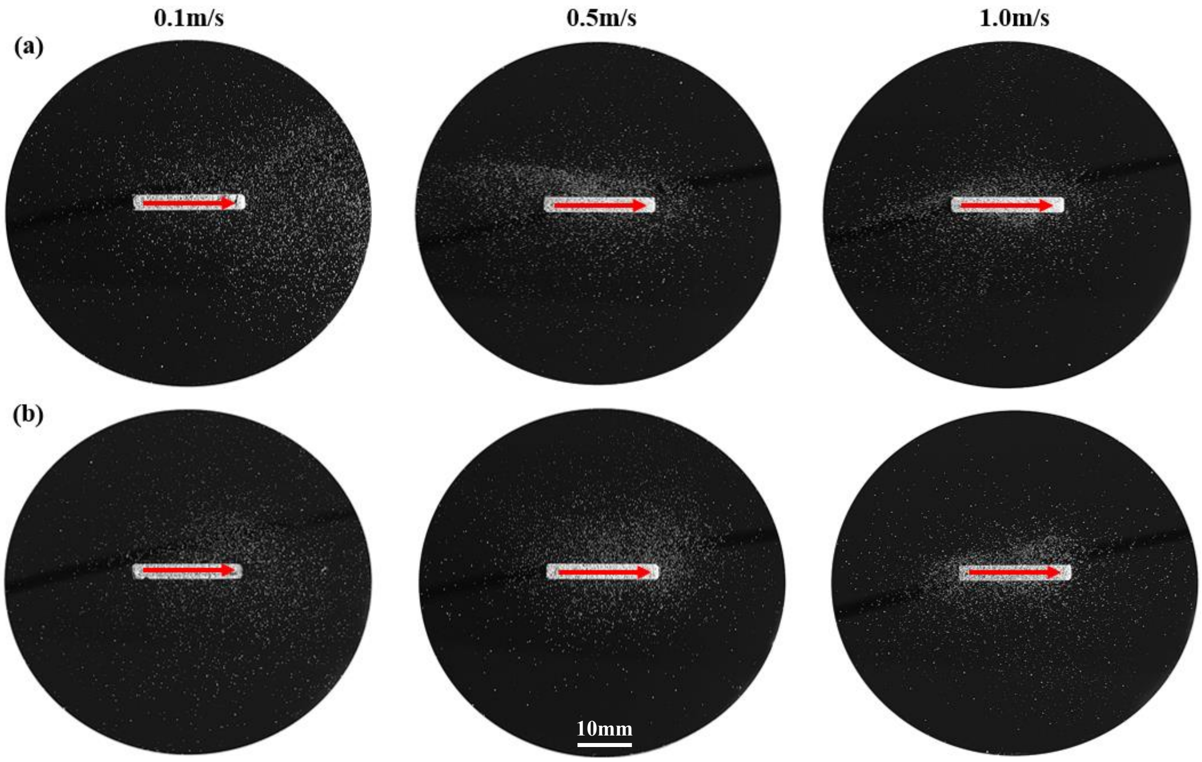

Fig. 6.3 Effect of scanning speed on the spatial distribution of spatter deposition under 100 W laser power. (a) First experiment. (b) Second experiment.

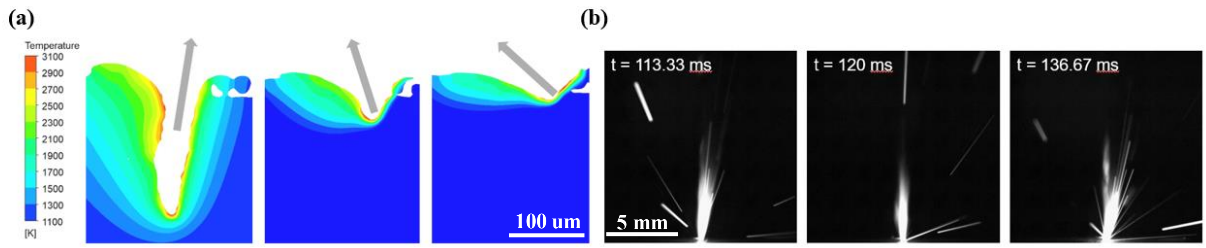

Fig. 6.4 Evolution of melt pool geometry and plume dynamics with varying processing conditions. (a) Schematic illustration of melt pool morphology at varying scan speeds (0.1, 0.5, and 1 m/s) under a constant laser power of 100 W, indicating the transition from keyhole-like to conduction-mode behavior.(b) Time-resolved high-speed

images of plume and spatter dynamics at a laser power of 100 W and a scan speed of 0.1 m/s, captured at different time instants (t = 113.33 ms, 120 ms, and 136.67 ms).

While these trends highlight a deterministic evolution of mean spatter angle with scan speed, deposition patterns remain highly stochastic and non-reproducible across repeated builds. This variability originates from two primary sources. First, heterogeneity in powder bed packing-induced by recoating inconsistencies, particle size variation, and local porosity-leads to differences in the local laser-powder interaction conditions. Second, the vapor plume itself is inherently unsteady due to rapid fluctuations in recoil pressure, localized vaporization bursts, and interfacial instability of the melt pool, often amplified by Marangoni-driven thermocapillary flow.

To substantiate the transient nature of plume dynamics, time-resolved high-speed imaging was performed under 100 W-0.1 m/s conditions over a 20 mm track length, as shown in Fig. 6.4(b). The captured image sequence (from t = 113.33 ms to t = 136.67 ms) reveals pronounced temporal variations in plume structure and ejection behavior. In the early frames, asymmetric and oblique spatter ejection directions are observed, indicating spatially non-uniform behavior. As time progresses, multiple spatter events with a broader angular dispersion are captured, suggesting increased variability in plume dynamics. These observations suggest that transient plume behavior may influence the non-uniform distribution of spatter during the process, although the underlying mechanisms cannot be directly resolved from the present imaging data.

Collectively, the results establish that scan speed exerts a twofold influence on spatter behaviour: it governs the melt pool geometry and vapor jet orientation, which control the mean deposition angle, and it also interacts with powder bed variability and plume turbulence, which jointly determine the statistical scatter and repeatability of spatter trajectories. Understanding this dual mechanism is essential for improving process robustness, optimizing scan strategies, and reducing defect precursors in LPBF-built components.

6.4 Onset of Particle Mobility: Overcoming Interfacial Friction and Initiating Denudation

Upon laser irradiation, the surface material undergoes rapid melting followed by intense evaporation, generating a strong upward-directed recoil vapor jet. This jet produces a localized low-pressure region via the Bernoulli effect—a fundamental fluid dynamics principle where an increase in fluid velocity is accompanied by a decrease in static pressure. The resulting pressure gradient draws surrounding shielding gas radially inward toward the melt pool, forming a converging flow field. Powder particles situated within this field are subjected to shear-induced drag forces arising from the relative motion between the particles and the surrounding gas. The magnitude of this aerodynamic force is strongly influenced by the velocity gradient of the vapor-driven flow, particle size, orientation, and proximity to the jet axis.

When the drag force surpasses the rolling resistance exerted by the substrate or neighboring particles, the powder begins to roll toward the melt pool. This marks the onset of both powder spattering and localized powder bed depletion, commonly referred to as denudation. Therefore, accurately determining the critical conditions for particle mobilization is a crucial first step in understanding the underlying mechanisms of spatter formation. Once the resisting interparticle or substrate friction is overcome, particles are free to migrate, initiating the dynamic redistribution of powder near the melt pool periphery.

Fig. 6.5 presents the experimentally observed denudation characteristics at a fixed laser power of 100 W with three different scanning speeds (0.1 m/s, 0.5 m/s, and 1.0 m/s). Along both sides of the scan track, the powder appears visibly depleted, with redistributed particles accumulating near the melt track boundary. The denudation width (WD) is consistently wider than the melt track width (WM), illustrating that the entrainment-driven disturbance extends well beyond the direct laser-melting zone.

Interestingly, the denudation width decreases with increasing scan speed, following the order: 0.1 m/s > 0.5 m/s > 1.0 m/s. This trend emphasizes that laser–material interaction time plays a dominant role in determining the extent of powder disturbance. At 0.1 m/s, the prolonged laser residence time induces significant melt pool expansion and intense vapor recoil, generating a strong and sustained entrainment flow that removes large quantities of surrounding powder. At 0.5 m/s, the interaction time is reduced, leading to a moderately sized melt pool and weaker entrainment effects, thereby lowering the denudation extent.

Although melt pool instability and plume fluctuations remain pronounced at 1.0 m/s, the high scanning speed limits powder removal through two coupled mechanisms. On one hand, the substantially shorter laser-powder interaction time reduces the momentum transferred to surrounding particles. On the other hand, the faster scanning speed leads to weaker evaporation, which in turn diminishes the vapor-driven spattering and denudation. As a result of this combined effect, gas entrainment is minimized, fewer powder particles are set into motion, and the smallest denudation width is observed. This indicates that, despite thermal and hydrodynamic instabilities, the reduction in both momentum transfer and evaporation intensity—both governed by interaction duration—is the critical factor controlling powder removal behavior under high scanning speeds.

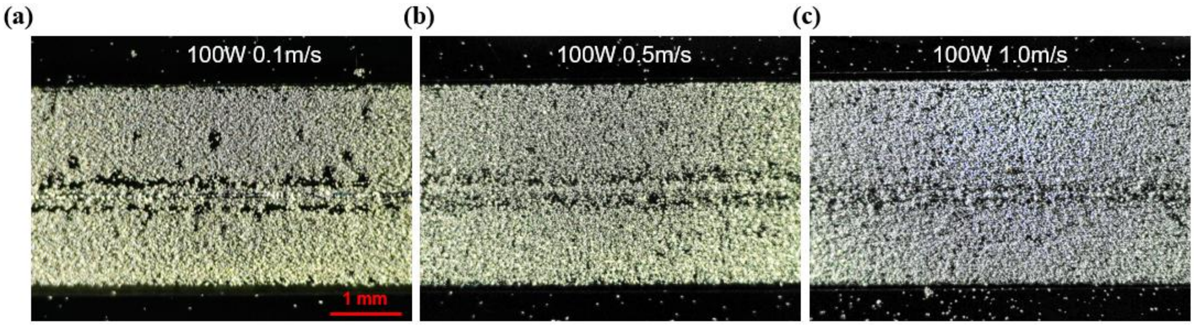

Fig. 6.5 Experimentally observed denudation characteristics at 100 W under different scanning speeds.(a) 0.1 m/s. (b) 0.5 m/s. (c) 1.0 m/s.

To establish a quantitative relationship between particle-scale dynamics and the formation of powder-depleted regions, we employed high-speed imaging in combination with ImageJ analysis to capture the motion of powder particles (approximately 50 μm in diameter) impacted by the vapor plume and subsequently falling onto the substrate, as shown in Fig. 6.6(a). By tracking particle deceleration, the rolling friction force was estimated for a representative

50 µm particle using Newton's second law, yielding $F_r = ma = 5.4\times10^{-9}$ N. This force can also be expressed as

$$F_r = \mu(F_{vdw} + mg) \tag{6-1}$$

where μ is the rolling friction coefficient taken as 0.085 [160], F_{vdw} is the van der Waals adhesion force and mg is the gravitational force.

Table 6.1 Comparison of gravity and van der Waals force for particles of different diameters.

Diameter (um)	10	20	30	40	50
mg (N)	4.0×10^{-11}	3.2×10^{-10}	1.1×10^{-9}	2.6×10^{-9}	5.0×10^{-9}
F_{vdW} (N)	1.3×10^{-8}	2.5×10^{-8}	3.7×10^{-8}	4.8×10^{-8}	5.9×10^{-8}

As shown in Table 6.1, within the typical LPBF particle size range (10-50 µm), F_{vdW} is generally on the order of 10^{-8} N, which is one to two orders of magnitude larger than the gravitational force mg (approximately 10^{-11} to 10^{-9} N). Hence, gravitational effects can be reasonably neglected in the calculation of frictional resistance. Furthermore, since F_{vdW} scales linearly with particle diameter, the rolling friction force F_r also exhibits a linear dependence on particle size. This proportionality implies that particles of different sizes share a common critical entrainment velocity, as the ratio of aerodynamic drag to rolling resistance remains constant within the examined size range.

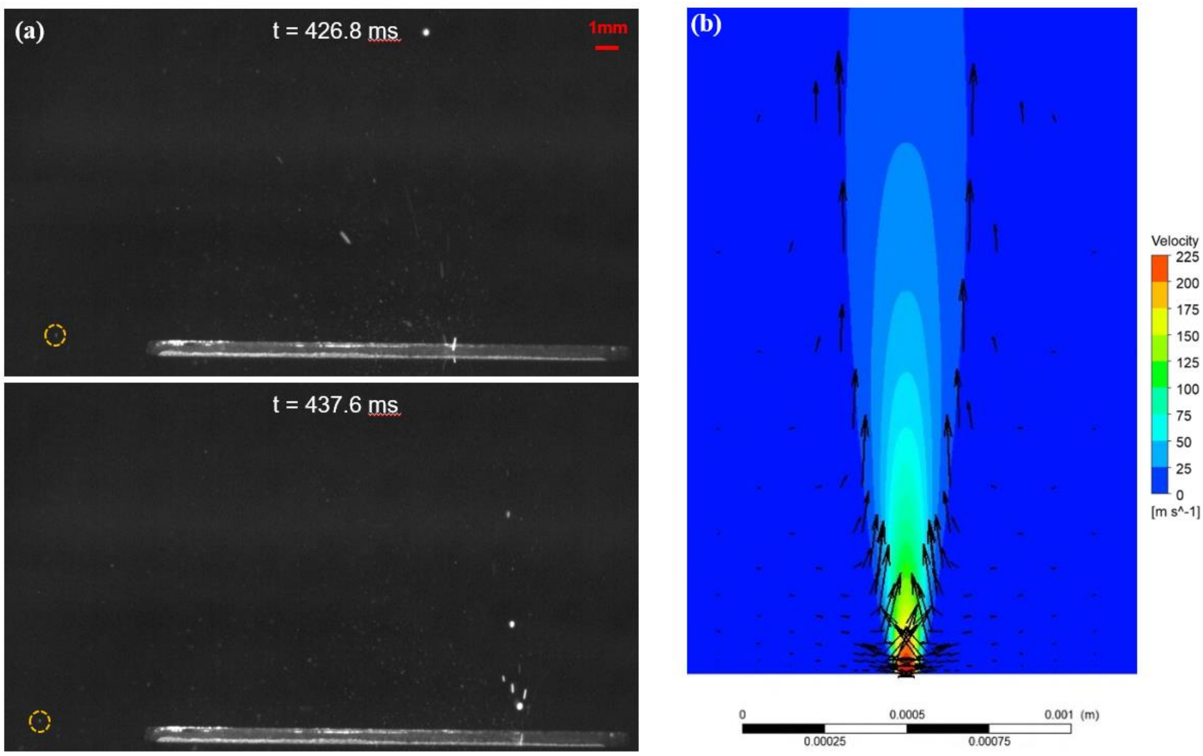

Fig. 6.6. Particle entrainment dynamics and surrounding gas flow field induced by laser-generated vapor plume. (a) High-speed imaging of powder particle trajectories during interaction with the vapor plume. (b) Simulated gas velocity field around the vapor plume at 100 W laser power, illustrating the entrainment and recirculation effects that underlie the experimentally observed particle motion.

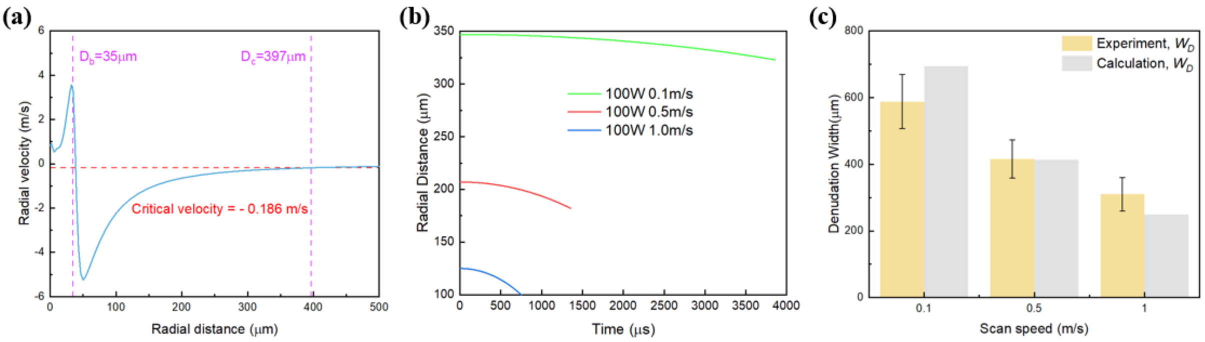

Fig. 6.7. CFD-based analysis of gas flow field and particle displacement under 100 W laser power. (a) Radial gas velocity field at z = 25 μm with critical velocities for different particle sizes. (b) Calculated displacement-time curves for 50 μm particles under various scanning speeds. (c) Comparison of predicted particle departure positions with experimentally observed depletion zones.

To elucidate the kinematic correlation between particle movement and the vapor plume-induced airflow dynamics, computational fluid dynamics (CFD) simulations were conducted to determine the gas velocity field surrounding the vapor plume at a laser power of 100 W, as illustrated in Fig. 6.6(b). The simulation results clearly demonstrate that the high-speed vapor jet induces a pronounced entrainment effect, drawing ambient air inward towards the plume centerline, as indicated by the black velocity vectors. From the obtained gas flow field, we extracted the radial velocity distribution at a cross-sectional plane positioned at a height of z = 25 μm above the substrate surface (Fig. 6.7a). At greater radial distances from the plume centerline, the radial gas velocity is positive, signifying that powder particles located in this region experience an inward entrainment force towards the vapor plume. This inward radial velocity progressively increases as particles approach the plume. However, at close proximity to the plume center, the radial velocity reverses, becoming negative due to the strong outward-directed expansion recoil force from the vapor jet, resulting in the ejection of particles away from the plume center. Additionally, within the entrainment region, the radial gas velocity magnitude exhibits an approximately inverse proportionality to the radial distance.

Considering the aerodynamic drag force acting on particles with laminar assumption away from vapor plume center, the classical Stokes drag relationship is expressed as

$$F_{drag} = 6\pi\eta_g r_p(v_g - v_p) \tag{6-2}$$

where F_{drag} is the drag force, η_g is the dynamic viscosity of the gas, r_p is the particle radius, v_g is the gas velocity, and v_p is the particle velocity. Then the critical radial positions corresponding to the onset of mobility for particles of different sizes were identified, as annotated in Fig. 6.7(a). Based on these critical conditions, a quantitative relationship between the radial gas velocity magnitude and radial distance was established via curve fitting.

To further quantify particle motion, the particle acceleration was computed based on the gas flow field obtained from CFD simulations, governed by the balance between aerodynamic drag and rolling resistance:

$$a = (F_{drag} - F_r)/m \tag{6-3}$$

where F_r is the rolling resistance acting on the particle.

A numerical time-integration scheme was employed to resolve the particle motion. The particle velocity and displacement were updated iteratively using:

$$v_p^{t+\Delta t} = v_p^t + a\Delta t \tag{6-4}$$

$$s^{t+\Delta t} = s^t + \frac{v_p^{t+\Delta t} + v_p^t}{2}\Delta t \tag{6-5}$$

The initial conditions were set as v_p^0 = 0 and s^0 = 0, corresponding to particles initially at rest on the powder bed. At each time step, the local gas velocity and corresponding drag force were updated based on the instantaneous particle position. This procedure was repeated until the particle reached the melt pool boundary or the interaction time was exceeded. A sufficiently small-time step (Δt = 0.01 μs) was adopted to ensure numerical stability and accurately capture the rapid acceleration of particles under the vapor plume. Although the model adopts simplified assumptions (e.g., laminar drag formulation), it captures the dominant physics governing particle entrainment and displacement near the melt pool region.

The resulting particle trajectories in Fig. 6.7(b) provide displacement–time relationships for particles approaching the melt pool under different scanning speeds. As particles migrate from their initial positions, powder-depleted regions, commonly referred to as denudation zones, are formed adjacent to the melt track. To quantitatively determine the denudation boundary, a displacement-based criterion was introduced. Specifically, the radial position at which the particle displacement exceeds the average powder particle diameter ($\Delta r \geq 30$ μm) was defined as the onset of effective powder removal. This criterion reflects the condition under which particles are displaced sufficiently far from their original packing positions and cannot be immediately replenished by neighboring particles. Using this definition, the denudation width was calculated as the radial distance from the melt track centerline to the critical position satisfying Δr=30μm. The predicted denudation widths were then compared with experimentally observed powder-depleted regions extracted from high-speed imaging, as shown in Fig. 6.7(c). The results show good quantitative agreement, with minor discrepancies attributable to inherent process complexities.

Overall, this approach establishes a direct link between vapor-plume-induced gas flow, particle-scale dynamics, and the macroscopic formation of denudation zones. Specifically, at a low scanning speed (0.1 m/s), the larger observed denudation width is due to prolonged laser-material interaction time, allowing peripheral particles (approximately 347-397 μm from the center) to be progressively entrained inward, filling voids post laser interaction due to inertial effects. Conversely, at a higher scanning speed (1.0 m/s), a smaller calculated denudation width was observed compared to the experimental results. This discrepancy likely arises primarily due to melt pool instability manifesting as hump defects and amplified turbulent oscillations of the gas flow, enlarging the effective entrainment area.

Moreover, the potential influence of the external shielding gas flow should also be considered in practical LPBF processes. In the present study, the CFD model focuses primarily on the gas flow induced by the vapor plume in the immediate vicinity of the melt pool, which governs the initial entrainment and motion of powder particles. The shielding gas flow was not explicitly included in the simulation because its characteristic velocity in the build chamber is typically much lower than that of the vapor jet generated during laser–material interaction. Consequently, near the melt pool region where particle entrainment occurs, the vapor-plume-driven flow dominates the local gas dynamics.

Nevertheless, shielding gas flow can influence the longer-range transport of spatter particles and may contribute to additional powder redistribution across the powder bed. Excessively high shielding gas velocities may further enhance particle mobilization by increasing aerodynamic drag, thereby intensifying powder loss and widening the denudation region. Therefore, careful optimization of both scanning parameters and shielding gas flow conditions is important to mitigate denudation and maintain powder bed uniformity during the LPBF process.

6.5 Detachment Dynamics: Lifting Beyond Adhesion in Single and Clustered Particles

While particle mobilization marks the initial condition for the formation of spatter in LPBF, it does not guarantee complete detachment or ejection from the powder bed. In practice, a significant number of mobilized particles remain accumulated near the melt track without being successfully lifted. For a particle to become a true spatter, it must not only overcome the resistance to rolling or sliding but also be lifted away from the substrate surface by the aerodynamic forces associated with the vapor plume and surrounding gas flows.

In this micro-scale regime, where gravitational forces are negligible compared to surface forces, van der Waals (vdW) adhesion plays a critical role in resisting vertical detachment. Analogous to how macroscopic objects must overcome gravitational force to achieve lift-off, micron-sized powder particles must overcome interfacial adhesion to escape the substrate or neighboring particles. Therefore, a quantitative understanding of the van der Waals interaction is essential for accurately modeling the onset of detachment.

The vdW force represents a short-range attractive interaction arising from fluctuating dipole–dipole effects. It is especially dominant in fine particulate systems, particularly at particle sizes below ~100 μm. For two spherical particles with radii R_1 and R_2, separated by a gap h, the vdW force can be estimated using the classical Hamaker approach as:

$$F = -\frac{A}{6} \cdot \frac{R_1 R_2}{(R_1 + R_2)h^2} \tag{6-6}$$

where A is the Hamaker constant, typically on the order of 10^{-20} to 10^{-19} J depending on the material and surrounding medium [169][170]. For identical particles ($R_1 = R_2 = R$), this expression simplifies to

$$F = -\frac{AR}{12h^2} \tag{6-7}$$

When a spherical particle is adjacent to a planar substrate, the interaction force becomes

$$F = -\frac{AR}{6h^2} \tag{6-8}$$

which is approximately twice the magnitude of the sphere–sphere interaction [171]. This difference arises because the planar substrate can be treated as a body with an effectively infinite radius of curvature under the Derjaguin approximation, leading to a stronger interaction compared with the symmetric sphere–sphere configuration.

In a more complex but common configuration where a particle is supported by three identical spherical particles beneath it-forming a typical close-packed contact geometry, as illustrated schematically in Fig. 6.8 [164]. The total vertical vdW force on the upper particle can be obtained by projecting each particle–particle force onto the vertical axis. Given the angular arrangement of the contact points (with a contact angle of approximately 55°), the resulting vertical force sums to

$$F = -\frac{AR}{6.93h^2} \tag{6-9}$$

This value lies between the sphere–sphere and sphere–plane interaction limits and provides a reasonable approximation for adhesion under powder-bed conditions.

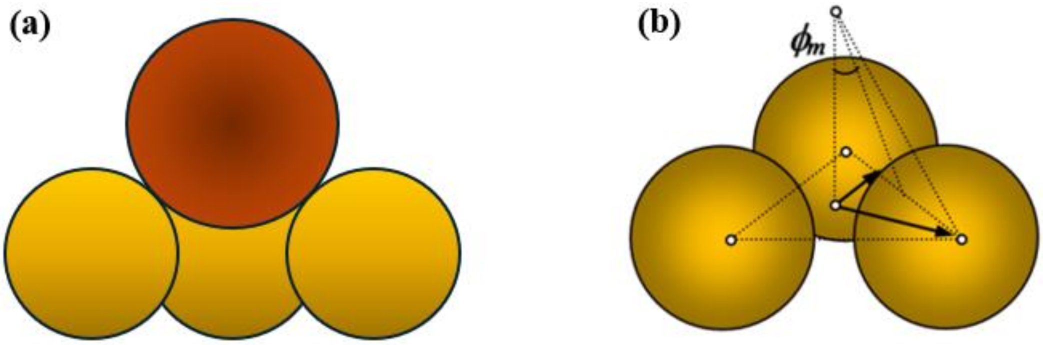

Fig. 6.8. Particle arrangement and pivoting angle in the powder bed. (a) Three-dimensional configuration of bed particles; (b) Schematic definition of the average pivoting angle.

To simplify calculations and to reasonably approximate the maximum adhesive force likely to occur in contact-dominated scenarios, the sphere–plane model (6-8) is adopted in this study as a representative formulation for estimating the van der Waals force acting on powder particles in contact with their surroundings.

Subsequent to mobilization, the second critical step for powder particles to become spatter involves overcoming the adhesion forces between the particle and the substrate or neighboring particles. Successful detachment requires that the aerodynamic drag and lift forces exerted by the vapor plume-induced airflow surpass the cohesive van der Waals adhesion force. However, the dynamics of particle detachment significantly differ between single-particle and multi-particle systems, as depicted in Fig. 6.9. For single-particle systems, the dynamic behavior under the influence of entrainment flow fields has been extensively studied, as shown in Fig. 6.9(a). Typically, a single particle initially moves toward the melt pool region due to the inward-directed drag force. When the aerodynamic forces exceed the adhesion threshold, the particle is lifted vertically into the airflow and continues its trajectory toward the melt pool and vapor plume region. In contrast, the multi-particle systems display a more complex behavior. When an upper particle within a particle cluster experiences a drag force applied at an offset position relative to the cluster's center of mass, a resultant torque develops about the adhesion point, causing the particle to rotate and accumulate angular momentum. With increasing rotational velocity, the required centripetal force for maintaining stable rotation increases nonlinearly. Once the combined centripetal component of the aerodynamic drag and cohesive van der Waals forces become insufficient to sustain rotation, mechanical instability occurs, resulting in particle detachment and subsequent entry into free-flight toward the melt pool and vapor plume, as shown in Fig. 6.9(b). For particles located at the bottom of a cluster, particularly in systems consisting of multiple layers, detachment is significantly hindered by the considerably enhanced static friction and cohesive interactions. Unless positioned very close to the melt pool, where the vapor plume-induced drag forces are exceptionally strong, these bottom-layer particles typically remain stationary and resist entrainment. An exceptional scenario occurs when particles—either single or multi-layered clusters—are situated in immediate proximity to the melt pool and vapor plume, where the intense direct momentum transfer from the vapor plume rapidly induces detachment, bypassing intermediate transitional stages and directly ejecting particles into the airflow as spatter.

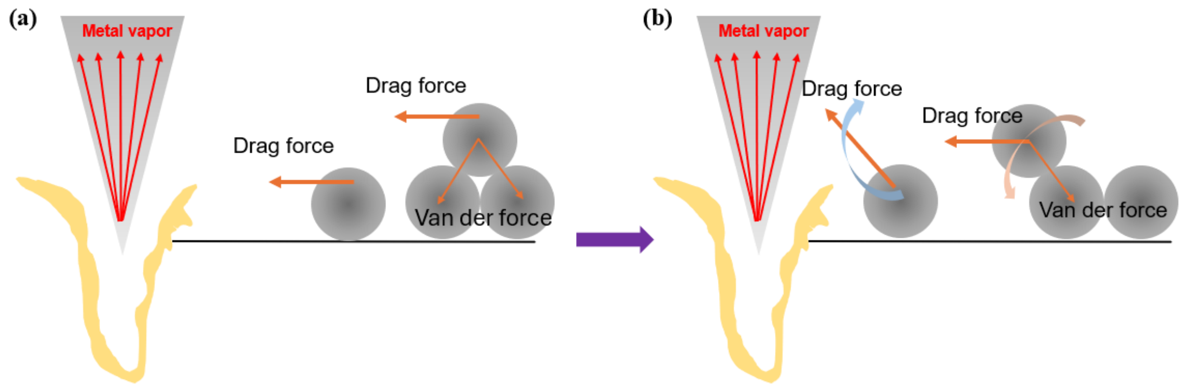

Fig. 6.9. Aerodynamic behavior of powder particles under vapor plume influence. (a) Single-particle response. (b) Multi-particle (clustered) response.

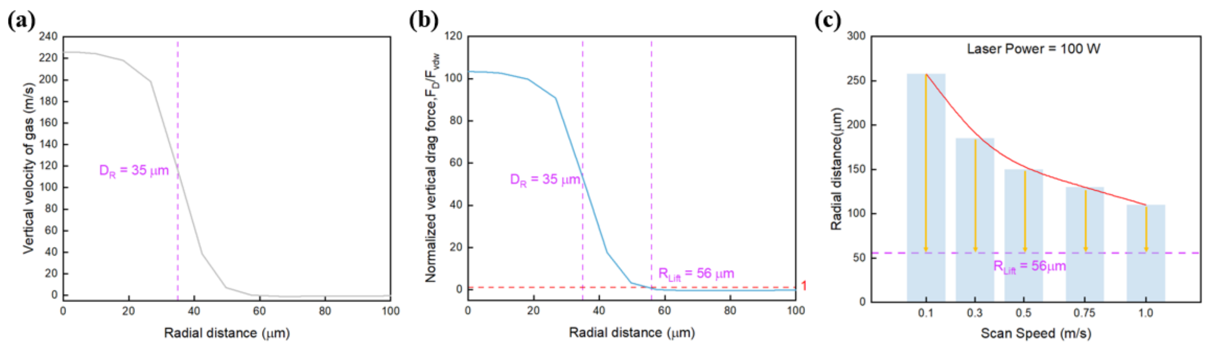

Fig. 6.10 CFD-based analysis of particle lift-off conditions at 100 W laser power. (a) Radial distribution of vertical gas velocity. (b) Normalized vertical drag force (F_{drag}/F_{vdw}) as a function of radial distance from the plume center. (c) Radial range R_{Lift} of particles susceptible to lift-off under varying scanning speeds.

To quantitatively determine the critical aerodynamic conditions required for powder particle lift-off, CFD simulations were performed to characterize the radial distribution of vertical gas velocities at a laser power of 100 W, as depicted in Fig. 6.10(a). The vertical component of gas velocity is oriented upwards, exhibiting its maximum magnitude at the centerline of the vapor jet and rapidly diminishing to zero along the radial direction. Based on the established relationship between aerodynamic drag forces and the airflow field, Fig. 6.10(b) presents the normalized ratio of vertical drag force (F_D) to the adhesion force (F_{vdW}) as a function of radial distance. A critical radial threshold (R_{Lift} = 56 μm) was identified at which the aerodynamic drag surpasses the adhesion forces, initiating vertical lift-off of powder particles from the substrate surface. This threshold clearly delineates the boundary beyond which particle entrainment into the airflow is achievable. Fig. 6.10(c) summarizes the radial range within which powder particles can reach this critical lift-off threshold (R_{Lift}) under various scanning speeds at a constant laser power of 100 W. With increasing scanning speed and correspondingly reduced laser dwell time, the radial range of powder particles capable of moving toward and subsequently being lifted into the melt pool decreases significantly. However, this reduction is not linearly proportional to the scanning speed, suggesting complex interactions between particle motion, gas flow dynamics, and transient thermal fields.

Further analysis indicates that at lower scanning speeds, extended laser-material interaction times result in sustained vapor jet momentum, creating broader aerodynamic entrainment zones. This broader influence facilitates mobilization and lift-off of particles initially located farther from the plume center. Conversely, at higher scanning speeds, shorter dwell times constrain the vapor jet's momentum, limiting the extent and strength of the aerodynamic field, thus markedly decreasing the population of particles that can achieve the lift-off condition. Additionally, turbulent fluctuations and transient instabilities at high scanning speeds could also modulate particle dynamics, occasionally permitting sporadic lift-off events outside the typical aerodynamic threshold. These insights underline the necessity for precise tuning of process parameters to optimize aerodynamic entrainment, mitigate undesired powder depletion (denudation), and enhance process stability and repeatability.

6.6 Escape verus Incorporation: The Role of Melt Pool Wetting in Final Spatter

Previous empirical approaches have attempted to predict spatter quantity; however, they have proven insufficient across varying process parameters and material conditions[172]. In this section, a quantitative relationship between particle dynamics and spatter formation is established by integrating high-speed imaging analysis with theoretical modeling. Experimental spatter counts, obtained from high-speed images (Fig. 6.3) at a constant laser power of 100 W and varying scanning speeds, were quantified using ImageJ, as summarized in Fig. 6.12(a). A general decreasing trend in spatter quantity with increasing scanning speed is observed. However, a distinct local maximum appears at approximately 0.75 m/s, followed by a rapid decrease at 1.0 m/s. This non-monotonic behavior indicates that spatter generation cannot be described solely by linear energy density (LED). Instead, it arises from the coupled effects of melt pool stability, wettability, laser–material interaction time, and vapor–particle dynamics. Consequently, relying solely on LED oversimplifies the underlying physics by neglecting critical factors such as melt pool morphology evolution, surface tension effects, recoil pressure fluctuations, and vapor plume-induced flow.

To establish a quantitative link between particle dynamics and spatter formation, a theoretical model was developed based on particle entrainment and lift-off behavior. Fig. 6.11(a) schematically illustrates the particle motion following the stage shown in Fig. 6.9: upon entering the R_{Lift} region, particles are driven upward toward the melt pool by the strong entrainment gas flow. It is assumed that once particles enter the lift-off region R_{Lift} and their vertical displacement h_p exceeds $e_p\sigma_t$ = 25 μm (where $e_p \approx 0.5$ is the powder bed packing density from Fig. 4.6 and σ_t = 50 μm is the layer thickness), the particle is considered unable to be re-incorporated into the melt pool due to insufficient wettability, and thus contributes to spatter formation. To quantitatively determine whether this condition is met, h_p is calculated from the equation as follows:

$$\frac{dh_p}{dt} = v_{p,vertical} = v_{g,vertical}\left(1 - e^{-\frac{t}{\tau}}\right);\ \tau = \frac{2\rho_p r_p^2}{9\eta_g} \tag{6-10}$$

$$h_p = \int_0^t v_{p,vertical}\, dt = v_{g,vertical}\left(t - \tau + \tau e^{-\frac{t}{\tau}}\right) \tag{6-11}$$

where $v_{p,vertical}$ and $v_{g,vertical}$ denote the vertical components of particle velocity and gas velocity, respectively. The gas velocity is approximated as the average velocity between σ_b and R_{Lift} (Fig. 6.10a). The residence time t of a particle within the lift-off region depends on its radial velocity upon entering the region; particles farther from R_{Lift} exhibit higher radial velocities, resulting in shorter residence times. Using the critical velocity with the denudation analysis (Section 6.4)-which defines the farthest position a particle can reach-the maximum radial velocity $v_{p,radial}^{max}$ for particles of different sizes was obtained, and the corresponding minimum residence time t_{min} along the particle trajectory was estimated. Over the t_{min}, the calculated h_p for all particle sizes exceeds the critical threshold of 25 µm, indicating that particles entering this region are likely to escape rather than be reabsorbed, as shown in Fig. 6.11(b).

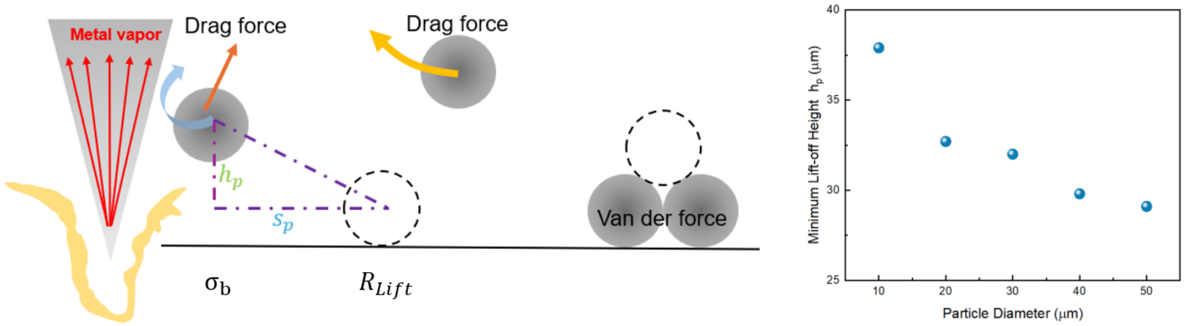

Fig. 6.11 Schematic of particle lift-off and spatter formation. (a) Particle motion driven by gas flow; escape occurs if $hp>e_p\sigma_t$=25um. (b) Calculated hp exceeds 25 µm for all particle sizes, indicating likely spatter.

As a first-order approximation neglecting melt pool capture effects, the radial escape boundary R_{es} —defined as the distance within which particles can escape the melt pool—was approximated by the laser beam radius. Accordingly, the spatter width L_{sp} was defined as:

$$L_{sp} = 2(R_f - R_{es}) \tag{6-12}$$

from which the spatter volume V_{sp} was derived:

$$V_{sp} = e_p \cdot L_{laser} \cdot L_{sp} \cdot \sigma_t \tag{6-13}$$

Where L_{laser} is the total length of the laser scan path, which is 21 mm. The mean particle volume $E(V_p)$ was calculated based on the particle size distribution:

$$E(V_p) = E(\frac{4\pi R_p^3}{3}) = \frac{4\pi}{3}[R_p^3 + 3E(R_p) \cdot \sigma(R_p)^2] \tag{6-14}$$

Thus, the total spatter quantity N_{sp} can be expressed as:

$$N_{sp} = V_{sp}/E(V_p) \tag{6-15}$$

The comparison between theoretical predictions and experimental data (Fig. 6.12 (a)) shows good agreement in both trend and magnitude. However, discrepancies arise due to the neglect of melt pool wettability and particle capture capability. At low scanning speeds, the melt pool exhibits excellent wettability, allowing most entrained particles to be reabsorbed, resulting in an overestimation of spatter by the model. Conversely, at higher scanning speeds, reduced wettability and insufficient melting promote particle escape, leading to underestimation.

Fig. 6.12 (b) and (c) highlight the critical role of melt pool wettability in governing particle behavior. Good wettability (contact angle $\beta < 90°$) promotes particle incorporation, whereas poor wettability ($\beta > 90°$) leads to repulsive behavior and particle rejection. The capillary retention force acting on particles is given by:

$$F_s = \pi\sqrt{h(r_p - h)}\gamma\cos\beta \tag{6-16}$$

where h is the wetting height , γ is the surface tension. When $\beta > 90°$, $\cos\beta < 0$, indicating a net repulsive force exerted by the melt pool on the particles.

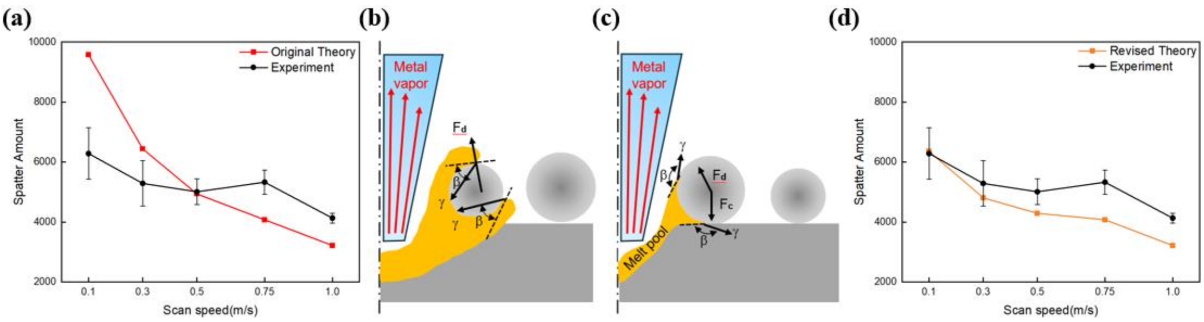

Fig. 6.12 Correlation between particle dynamics and spatter quantity under varying process conditions. (a) Experimental counts of spatter deposition sites on the substrate at 100 W under different scanning speeds. (b) Schematic of melt pool with good wettability promoting stable powder deposition. (c) Schematic of melt pool with poor wettability leading to increased powder spatter. (d) Theoretical predictions of spatter quantity considering wettability effects, compared with experimental data.

To incorporate wettability effects, the escape boundary R_{es} was revised. For low scanning speeds (≤ 0.5 m/s), R_{es} was taken as the melt track half-width (110 μm, 73 μm, and 50 μm for scanning speeds of 0.1, 0.3, and 0.5 m/s, respectively), reflecting strong particle absorption. For higher scanning speeds (> 0.5 m/s), R_{es} was approximated as the laser spot radius, accounting for reduced melting and wettability. The updated predictions (Fig. 6.12 (d)) show significantly improved agreement with experimental results. This improvement demonstrates that incorporating wettability effects is essential for accurately capturing spatter behavior. At low scanning speeds, prolonged laser-material interaction enhances vaporization and particle entrainment. However, due to good wettability, a large fraction of entrained particles is reabsorbed into the melt pool, reducing the final spatter count. At intermediate scanning speeds (~0.75 m/s), melt pool stability deteriorates and wettability decreases, reducing particle capture efficiency. As a result, more particles escape than are absorbed, leading to a local maximum in spatter quantity. At higher scanning speeds (1.0 m/s), reduced interaction time weakens vaporization and entrainment, resulting in an overall decrease in spatter despite poorer wettability. These findings indicate that spatter formation is governed by the competition between particle entrainment and melt pool capture, and spatter quantity should be understood as a non-monotonic outcome of coupled thermofluid and interfacial phenomena, rather than a simple function of energy input.

Nonetheless, spatter counts at 0.75 m/s and 1.0 m/s remain slightly underestimated. This discrepancy arises partly from an overestimation of R_{es} due to lack-of-fusion (LOF) defects, and partly from the theoretical model neglecting the effects of gas flow oscillations and turbulence. In addition to melt pool morphology and wettability, gas-phase drag forces play a critical role in powder entrainment, particularly under conditions where the vapor plume exhibits oscillatory behavior and induces localized turbulence. As a result, powder particles displaced near the melt front are subjected to significant aerodynamic drag from the shielding gas flow. Furthermore, when the gas stream undergoes continuous swaying and oscillation, the velocity of the flow above the powder bed increases, resulting in a pressure drop according to Bernoulli's principle. This pressure differential-where the pressure beneath the particle exceeds that above-can generate a turbulence-induced lift force (F_{LT}), expressed as:

$$F_{LT} = \frac{\pi}{4} d_p^3 \left(\frac{\partial \overline{p_{rz}}}{\partial z}\right)\bigg|_{d_p} \tag{6-17}$$

where d_p is the particle diameter, and $\overline{p_{rz}}$ denotes the pressure in the axial (z) direction at radial position r.

In addition to F_{LT}, the drag force imparted by the gas flow itself includes an upward-directed lift component, which further enhances the total lift acting on the particle. This increased lift facilitates the transition of entrained powder particles into spatter, particularly under conditions of strong vapor plume oscillation. This mechanism is vividly illustrated in the balling melt pool sequence depicted in Fig. 6.13[173]. In this scenario, the melt pool disintegrates into discrete, globular segments, interrupting continuous track formation and initiating lateral oscillations in the vapor plume. These oscillations result in rapid fluctuations in the radial vapor velocity v_r, transiently increasing the drag force F_D to magnitudes comparable to or even exceeding the gravitational force acting on the particles. Consequently, powder particles can be temporarily lifted, reheated, and re-ejected, aligning with the observed formation of thermally altered, cluster-like spatter.

This turbulent and thermodynamically dynamic environment is particularly conducive to the formation of secondary spatters. In contrast to primary spatters, which are directly ejected from the melt pool, secondary spatters originate from particles that were initially repelled due to poor wetting or entrained by turbulence. These particles may undergo reheating, partial melting, or agglomeration before being re-ejected from the process zone.

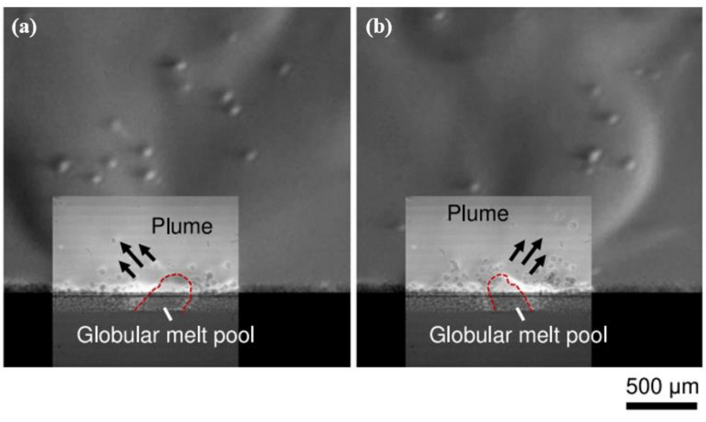

Fig. 6.13 Visualization of powder spatter promotion under melt pool balling conditions [173].

Altogether, spatter generation in LPBF results from a coupled mechanism involving melt pool instability, reduced wettability, unsteady plume dynamics, and turbulent powder entrainment. Importantly, poor wetting is not unique to any single regime, but manifests in different forms depending on power and speed-whether through hump formation at high speeds or balling at low energy input. When such conditions align with sufficient exposure time and turbulent lift, the likelihood of secondary powder spattering increases markedly, exacerbating particle irregularity, increasing total spatter yield, and potentially impairing powder bed quality in subsequent layers.

6.7 Conclusion

This chapter presents a comprehensive investigation into the powder spattering dynamics during the LPBF process through experimental characterization, high-speed imaging, theoretical modeling, and mechanistic analysis. The main findings are summarized as follows:

1. **Vapor-induced entrainment plays a primary role in governing powder particle spattering in LPBF.** Under laser irradiation, recoil pressure generates a high-velocity vapor jet that induces localized gas flow, entraining surrounding powder particles near the scan track edges. These particles are ejected in either solid or partially melted states, and exhibit irregular morphologies such as agglomeration, partial melting, and satellite attachment, which may adversely affect powder bed uniformity and subsequent energy absorption.
2. **Scanning speed critically influences both the quantity and directional characteristics of spatter.** As scanning speed increases, spatter behavior transitions from forward- and laterally dispersed ejection to a more rearward-directed and collimated pattern. This evolution reflects the combined effects of plume reorientation, melt pool stabilization, and reduced laser–material interaction time.
3. **While vapor-induced flow provides the primary driving force for particle motion, the actual detachment of particles is governed by the balance between aerodynamic drag, interfacial friction, and capillary adhesion.** At low scanning speeds, adhesion and friction dominate and hinder detachment. At higher scanning speeds, increased pressure gradients associated with vapor recoil enhance drag forces and promote particle lift-off. In addition, particle clusters exhibit delayed detachment due to larger contact areas and stronger cohesive interactions.
4. **The particle detachment process proceeds in two distinct stages: surface rolling followed by vertical lift-off.** Under recoil jet and shear flow influence, particles initially undergo micro-scale displacement—rolling, sliding, or tilting—along the powder bed surface. Only when the net force acquired during this motion surpasses both adhesion and frictional resistance can complete detachment and upward

acceleration occur. This mechanism expands the spatial range of spatter generation and increases the escape probability of particles near the scan path boundaries.

5. **Melt pool wettability plays a decisive role in determining whether entrained particles are captured or escape as spatter.** At low scanning speeds, good wettability promotes particle incorporation into the melt pool, reducing the final spatter count despite strong entrainment. At intermediate scanning speeds, reduced wettability decreases capture efficiency, leading to increased spatter generation. At higher scanning speeds, weakened entrainment due to shorter interaction time results in a reduction in spatter. Incorporating wettability into the theoretical model significantly improves the agreement between predicted and experimental spatter quantities.

In summary, spatter formation in LPBF is governed by vapor-plume-induced entrainment, constrained by interfacial force balance, realized through a two-stage detachment process, and ultimately regulated by melt pool wettability. The integrated mechanistic framework proposed in this chapter provides both theoretical insights for defect mitigation and foundational guidance for the development of high-fidelity numerical simulations and real-time process monitoring strategies.

Chapter 7. Conclusions and Future Work

7.1 Conclusions

This study presents a comprehensive multi-physics investigation into the thermofluidic and particulate dynamics governing defect formation in LPBF. By integrating high-fidelity simulations with systematic experimental validation, the underlying mechanisms driving melt pool instability and powder spattering were elucidated. The key conclusions are summarized as follows:

1. **Time-resolved interfacial heat flux as a quantitative descriptor of melt pool stability:**
   This study establishes that melt pool morphology is governed by the time-resolved interfacial heat flux at the solid–liquid interface. By introducing the area-averaged interfacial heat flux q_{IA} and its normalized fluctuation intensity $\delta(q_{IA})$, a quantitative framework is developed to characterize melt track stability. While q_{IA} increases monotonically with scan speed, the transition from smooth to hump and balling regimes is controlled by the combined effect of heat flux magnitude and fluctuation intensity. In particular, both hump and balling defects are generally associated with relatively large $\delta(q_{IA})$, whereas smooth tracks can be maintained either under low q_{IA} or under conditions with suppressed fluctuations. This framework provides a unified criterion linking transient heat transfer to melt pool morphology.
2. **Spatial temperature gradient distribution and Marangoni circulation as the physical origin of heat flux fluctuation:**
   The fluctuation behavior of interfacial heat flux is governed by the spatial organization of temperature gradients and the associated Marangoni convection. Increasing scan speed leads to higher and more localized temperature gradients, resulting in spatially non-uniform heat extraction. When Marangoni circulation is weak or spatially limited (e.g., 100 W, 0.5 m/s), heat redistribution is incomplete, leading to relatively large fluctuation intensity despite low q_{IA}. In contrast, a well-developed and closed Marangoni circulation (e.g., 200 W, 0.5-1 m/s) enables efficient heat redistribution,

stabilizing the thermal field and suppressing fluctuations. When temperature gradients become highly localized and circulation weakens or disappears, thermal transport becomes imbalanced, leading to instability. These results demonstrate that the coherence of thermal transport, rather than heat flux magnitude alone, governs fluctuation intensity.

3. **Coupled thermal–flow mechanism governing pore formation and evolution:**
   Pore formation is controlled by the coupled evolution of thermal accumulation and melt pool flow. The net heat accumulation q_{acc} determines the stability of the keyhole and the likelihood of collapse. Sustained or pronounced negative q_{acc} reduces recoil pressure and promotes keyhole collapse, leading to bubble generation. At the same time, weakened Marangoni convection under such conditions suppresses upward recirculation, causing bubbles to migrate rearward along the melt flow and become trapped at the solidification front. In contrast, when negative q_{acc} is transient and Marangoni circulation remains active, bubbles can be redirected toward the keyhole and reabsorbed, reducing porosity. These results reveal that pore formation is not solely governed by instantaneous pressure fluctuations, but by the coupled dynamics of heat transfer and flow field evolution.
4. **Dual effect of substrate preheating on defect formation through modification of heat transfer and flow behavior:**
   Substrate preheating modifies melt pool behavior by altering both the magnitude and spatial distribution of heat transfer. Quantitative results show that preheating reduces the averaged interfacial heat flux q_{IA} while having limited influence on its normalized fluctuation intensity $\delta(q_{IA})$. At high scan speeds, this leads to more uniform temperature gradients and enhanced melt pool stability, effectively suppressing hump defects. However, under low scan speed conditions, preheating increases pore number (from 7 to 15) and enlarges average pore size (from ~5 μm to ~9.8 μm), indicating aggravated porosity. This deterioration is attributed to enhanced overheating, reduced net heat accumulation, and weakened Marangoni convection, which together promote bubble generation and entrapment. These findings highlight the process-dependent nature of preheating and emphasize the need for optimized parameter selection.

5. **Vapor-driven spatter dynamics and its quantitative characteristics:**

   Vapor-induced entrainment is identified as the dominant mechanism governing powder particle spattering in SLM. High-speed imaging and particle collection experiments reveal a clear transition in spatter behavior with increasing scanning speed, from thermally driven to momentum-dominated regimes. Quantitatively, the spatial distribution of spatter exhibits strong directionality, with the dominant ejection direction shifting from forward to rearward as scanning speed increases. Meanwhile, the total spatter amount decreases significantly from approximately 6500-7000 particles at 0.1 m/s to ~4000 particles at 1.0 m/s (100 W), reflecting the reduced laser-material interaction time and modified recoil gas flow dynamics. These results demonstrate that spatter behavior is governed by the combined effects of vapor plume dynamics, interaction time, and flow instability.

6. **Force-based particle detachment mechanism with deterministic criteria:**

   A force-balance-based theoretical framework is established to describe particle motion and detachment from the powder bed. It is shown that particle removal follows a sequential rolling-lift-off mechanism, governed by the competition between aerodynamic drag, van der Waals adhesion, and friction forces. The onset of particle motion is defined by a drag-friction criterion, leading to a critical radial position of approximately 397 μm and a unified critical velocity of ~0.18 m/s for particle mobilization. Furthermore, particle escape is determined by a lift-off condition, where particles exceeding a critical lift-off height (half thickness of powder bed) cannot be recaptured by the laser. Quantitative analysis confirms that particles entering the lift-off region always possess velocities below the capture threshold, indicating that bottom particles inevitably escape and contribute to spatter formation. This establishes a deterministic, location-dependent criterion for spatter generation.

7. **Quantitative prediction of spatter amount incorporating wettability effects:**

   To bridge microscale particle dynamics with macroscopic spatter behavior, a predictive model is developed by incorporating melt-pool wettability into the entrainment framework. The model introduces a wettability-modified entrainment length, linking particle incorporation and escape to melt-pool geometry and surface interaction.

Without considering wettability, the predicted spatter quantity shows significant deviation from experimental results. After incorporating wettability effects, the model accurately captures both the trend and magnitude of spatter quantity across different scanning speeds, achieving a maximum deviation within 25%. These findings demonstrate that wettability plays a critical role in governing the balance between particle incorporation and escape, enabling quantitative prediction of spatter generation.

Taken together, this work establishes that defect formation in LPBF is governed by the coupled interplay among heat loss distribution, melt pool dynamics, particle-gas interactions, and plume behavior. It emphasizes the necessity of integrated thermal-fluid-particulate modeling to support the design of defect-mitigating strategies and real-time process control solutions.

7.2 Future work

Although this work has systematically revealed the physical mechanisms underlying spatter generation and melt pool instability in the LPBF process through a combined experimental-numerical approach, several open questions and research opportunities remain. Future studies may focus on the following directions to further improve the process stability, defect suppression, and prediction capability of LPBF systems:

(1) Dynamic Process Parameter Control Based on Melt Pool State Feedback

Current LPBF systems typically operate under fixed process parameters throughout the build. However, this static approach cannot adapt to real-time variations in melt pool morphology, thermal fluctuations, or spatter intensity. Future work should focus on implementing closed-loop control schemes capable of dynamically adjusting laser power, scan speed, or spot size in response to in-situ melt pool signals. By integrating real-time sensing (e.g., pyrometry, photodiodes, high-speed cameras) with control logic (e.g., PID or AI-based controllers [39]), the system could proactively suppress spatter when melt pool overheating, instability, or vapor plume intensification is detected. This adaptive strategy could significantly enhance build consistency and spatter mitigation across varying geometries and material conditions.

(2) Integrated Melt Pool-Spatter Coupled Simulation Framework

Although this work separates melt pool CFD modeling and powder spatter dynamics, in reality, the melt pool and spattering are tightly coupled phenomena. Spatter formation perturbs the powder bed and vapor flow, which in turn alters melt pool shape, temperature distribution, and even absorption efficiency. Therefore, future research should develop a fully coupled, high-fidelity CFD-DEM framework that simulates:

- Laser energy deposition and recoil pressure generation;
- Melt pool thermocapillary flow and phase change;
- Gas-particle interactions including drag, lift, entrainment, and turbulence;
- Multi-body particle-particle collisions and secondary ejections.

Such a simulation would capture two-way coupling between vapor plume behaviour and particle dynamics, enabling more realistic predictions of spatter trajectories, melt pool disturbance, and powder bed erosion. In addition, shockwave propagation, acoustic emissions, and transient recoil fluctuations could be included to simulate spattering under keyhole collapse or Marangoni instability.

(3) Development of Spatter Suppression and Removal Strategies

Spattering not only reduces material utilization and causes porosity, but also leads to optical contamination, powder bed heterogeneity, and build interruptions. Therefore, two complementary research tracks should be pursued:

(a) Spatter Suppression by Process Optimization

New spatter-suppression strategies should be explored through:

- Pre-sintering of powder to stabilize loose particles;
- Use of low energy density combined with large laser spot sizes;
- Application of high ambient pressure or pulsed lasers to reduce vapor recoil intensity;
- Incorporation of nanoparticles or additives to control surface tension-driven

instabilities and coalescence behavior [174].

These approaches can improve powder bed integrity, minimize recoil jet-induced ejection, and suppress secondary spattering caused by molten splash or impact.

(b) Spatter Removal through Flow Field Optimization

Since spatter accumulation is often localized near the melt pool periphery due to weak shielding gas velocity, improving gas flow design is another crucial direction. Future studies should:

- Redesign inlet-outlet configurations to enhance flow homogeneity [175];
- Use CFD-DPM simulations to identify dead zones and optimize flow pathways [176];
- Incorporate critical velocity thresholds to selectively remove ejected particles without disturbing raw powder;
- Explore localized suction or gas-knife mechanisms to physically isolate and remove spatters during printing.

This work lays a solid foundation for advancing defect control in LPBF by promoting a unified perspective that bridges thermal, fluid, and particle-scale mechanisms. The proposed future research directions aim to further enhance process reliability, component performance, and model-informed additive manufacturing innovation.

References

[1] Do, D. K., & Li, P. (2016). The effect of laser energy input on the microstructure, physical and mechanical properties of Ti-6Al-4V alloys by selective laser melting. *Virtual and Physical Prototyping*, *11*(1), 41-47.

[2] Tepylo, N., Huang, X., & Patnaik, P. C. (2019). Laser-based additive manufacturing technologies for aerospace applications. *Advanced Engineering Materials*, *21*(11), 1900617.

[3] Wang, D., Qian, Z. Y., Dou, W. H., Yang, Y. Q., Li, S., Bai, Y. C., & Xiao, Z. F. (2018). Research progress on selective laser melting of nickel based superalloy. *Addit. Manuf. Technol.*, *61*(10), 49.

[4] Tang, C., Tan, J. L., & Wong, C. H. (2018). A numerical investigation on the physical mechanisms of single track defects in selective laser melting. *International Journal of Heat and Mass Transfer*, *126*, 957-968.

[5] Hague, R., Dickens, P., & Hopkinson, N. (Eds.). (2006). *Rapid manufacturing: an industrial revolution for the digital age*. John Wiley & Sons.

[6] Matthews, M. J., Guss, G., Khairallah, S. A., Rubenchik, A. M., Depond, P. J., & King, W. E. (2016). Denudation of metal powder layers in laser powder bed fusion processes. *Acta Materialia*, *114*, 33-42.

[7] Gong, H., Rafi, K., Gu, H., Starr, T., & Stucker, B. (2014). Analysis of defect generation in Ti-6Al-4V parts made using powder bed fusion additive manufacturing processes. *Additive Manufacturing*, *1*, 87-98.

[8] King, W. E., Barth, H. D., Castillo, V. M., Gallegos, G. F., Gibbs, J. W., Hahn, D. E., ... & Rubenchik, A. M. (2014). Observation of keyhole-mode laser melting in laser powder-bed fusion additive manufacturing. *Journal of Materials Processing Technology*, *214*(12), 2915-2925.

[9] Aboulkhair, N. T., Everitt, N. M., Ashcroft, I., & Tuck, C. (2014). Reducing porosity in AlSi10Mg parts processed by selective laser melting. *Additive manufacturing*, *1*, 77-86.

[10] Parry, L., Ashcroft, I. A., & Wildman, R. D. (2016). Understanding the effect of laser scan strategy on residual stress in selective laser melting through thermo-mechanical simulation. *Additive Manufacturing*, *12*, 1-15.

[11] Wilhelm, M., Wissenbach, K. D., & Gasser, A. D. (1996). Shaped body especially prototype or replacement part production. *Patent DE19649865C1*, *2*.

[12] Liu, Y., Yang, Y., Mai, S., Wang, D., & Song, C. (2015). Investigation into spatter behavior during selective laser melting of AISI 316L stainless steel powder. *Materials & Design*, *87*, 797-806.

[13] Kurzynowski, T., Chlebus, E., Kuźnicka, B., & Reiner, J. (2012, February). Parameters in selective laser melting for processing metallic powders. In *High power laser materials processing: lasers, beam delivery, diagnostics, and applications* (Vol. 8239, pp. 317-322). SPIE.

[14] Calignano, F., Manfredi, D., Ambrosio, E. P., Biamino, S., Lombardi, M., Atzeni, E., ... & Fino, P. (2017). Overview on additive manufacturing technologies. *Proceedings of the IEEE*, *105*(4), 593-612.

[15] Lu, L., Fuh, J. Y. H., Chen, Z. D., Leong, C. C., & Wong, Y. S. (2000). In situ formation of TiC composite using selective laser melting. *Materials Research Bulletin*, *35*(9), 1555-1561.

[16] Over, C., Meiners, W., Wissenbach, K., Hutfless, J., & Lindemann, M. (2003, June). Rapid manufacturing of metal parts and tools using laser melting. In *Proceedings of the 2nd International WLT-Conference on Lasers in Manufacturing* (Vol. 2, pp. 265-269).

[17] Kruth, J. P., Froyen, L., Van Vaerenbergh, J., Mercelis, P., Rombouts, M., & Lauwers, B. (2004). Selective laser melting of iron-based powder. *Journal of materials processing technology*, *149*(1-3), 616-622.

[18] Yadroitsev, I., & Smurov, I. (2010). Selective laser melting technology: from the single laser melted track stability to 3D parts of complex shape. *Physics Procedia*, *5*, 551-560.

[19] Wehmöller, M., Warnke, P. H., Zilian, C., & Eufinger, H. (2005, May). Implant design and production—a new approach by selective laser melting.

In *International Congress Series* (Vol. 1281, pp. 690-695). Elsevier.

[20] Zhang, L. C., Klemm, D., Eckert, J., Hao, Y. L., & Sercombe, T. B. (2011). Manufacture by selective laser melting and mechanical behavior of a biomedical Ti–24Nb–4Zr–8Sn alloy. *Scripta Materialia*, *65*(1), 21-24.

[21] de Wild, M., Schumacher, R., Mayer, K., Schkommodau, E., Thoma, D., Bredell, M., ... & Weber, F. E. (2013). Bone regeneration by the osteoconductivity of porous titanium implants manufactured by selective laser melting: a histological and micro computed tomography study in the rabbit. *Tissue Engineering Part A*, *19*(23-24), 2645-2654.

[22] Demir, A. G., & Previtali, B. (2017). Additive manufacturing of cardiovascular CoCr stents by selective laser melting. *Materials & Design*, *119*, 338-350.

[23] Limmahakhun, S., Oloyede, A., Chantarapanich, N., Jiamwatthanachai, P., Sitthiseripratip, K., Xiao, Y., & Yan, C. (2017). Alternative designs of load−sharing cobalt chromium graded femoral stems. *Materials Today Communications*, *12*, 1-10.

[24] Vandenbroucke, B., & Kruth, J. P. (2007). Selective laser melting of biocompatible metals for rapid manufacturing of medical parts. *Rapid Prototyping Journal*.

[25] Metal Powder Report. (2015). *3D printed copper rocket engine part on way to Mars*. *Metal Powder Report*, 70(4), 196-197. https://www.sciencedirect.com/science/article/abs/pii/S0026065715003604

[26] Monash University. (2018). *Melbourne's 3D jet engine technology flies into production in France*. Monash University News. https://www.monash.edu/news/articles/melbournes-3d-jet-engine-technology-flies-into-production-in-france

[27] Sotov, A. V., Agapovichev, A. V., Smelov, V. G., Kokareva, V. V., Dmitrieva, M. O., Melnikov, A. A., ... & Anurov, Y. M. (2020). Investigation of the IN-738 superalloy microstructure and mechanical properties for the manufacturing of gas turbine engine nozzle guide vane by selective laser melting. *The International Journal of Advanced Manufacturing Technology*, *107*(5), 2525-

2535.

[28] Cellcore, S., Rocket Engine, https://www.etmm-online.com/3d-printing-arocket-engine-a-886960/ (accessed Feb. 02, 2021).

[29] Guanghui, S. H. I., Chengqi, G. U. A. N., Dongliang, Q. U. A. N., Dongtao, W. U., Lei, T. A. N. G., & Tong, G. A. O. (2020). An aerospace bracket designed by thermo-elastic topology optimization and manufactured by additive manufacturing. *Chinese Journal of Aeronautics*, *33*(4), 1252-1259.

[30] Beal, V. E., Erasenthiran, P., Ahrens, C. H., & Dickens, P. (2007). Evaluating the use of functionally graded materials inserts produced by selective laser melting on the injection moulding of plastics parts. *Proceedings of the Institution of Mechanical Engineers, Part B: Journal of Engineering Manufacture*, *221*(6), 945-954.

[31] Wang, L., Wei, Q. S., Xue, P. J., & Shi, Y. S. (2012). Fabricate mould insert with conformal cooling channel using selective laser melting. In *Advanced Materials Research* (Vol. 502, pp. 67-71). Trans Tech Publications Ltd.

[32] Armillotta, A., Baraggi, R., & Fasoli, S. (2014). SLM tooling for die casting with conformal cooling channels. *The International Journal of Advanced Manufacturing Technology*, *71*(1), 573-583.

[33] Holzweissig, M. J., Taube, A., Brenne, F., Schaper, M., & Niendorf, T. (2015). Microstructural characterization and mechanical performance of hot work tool steel processed by selective laser melting. *Metallurgical and Materials Transactions B*, *46*(2), 545-549.

[34] Sander, J., Hufenbach, J., Giebeler, L., Wendrock, H., Kühn, U., & Eckert, J. (2016). Microstructure and properties of FeCrMoVC tool steel produced by selective laser melting. *Materials & Design*, *89*, 335-341.

[35] Zhang, G., Wang, J., Li, J., Zhou, X., & Zhou, Y. (2024). Research on Key Technologies of Jewelry Design and Manufacturing Based on 3D Printing Technology. *Coatings*, *14*(6), 701.

[36] Grasso, M., & Colosimo, B. M. (2017). Process defects and in situ monitoring methods in metal powder bed fusion: a review. *Measurement Science and*

Technology, *28*(4), 044005.

[37] Malekipour, E., & El-Mounayri, H. (2018). Common defects and contributing parameters in powder bed fusion AM process and their classification for online monitoring and control: a review. *The International Journal of Advanced Manufacturing Technology*, *95*(1), 527-550.

[38] Wei, H. L., Mukherjee, T., Zhang, W., Zuback, J. S., Knapp, G. L., De, A., & DebRoy, T. (2021). Mechanistic models for additive manufacturing of metallic components. *Progress in Materials Science*, *116*, 100703.

[39] Khairallah, S. A., Martin, A. A., Lee, J. R., Guss, G., Calta, N. P., Hammons, J. A., ... & King, W. E. (2020). Controlling interdependent meso-nanosecond dynamics and defect generation in metal 3D printing. *Science*, *368*(6491), 660-665.

[40] Gunenthiram, V., Peyre, P., Schneider, M., Dal, M., Coste, F., Koutiri, I., & Fabbro, R. (2018). Experimental analysis of spatter generation and melt-pool behavior during the powder bed laser beam melting process. *Journal of Materials Processing Technology*, *251*, 376-386.

[41] Bidare, P., Bitharas, I., Ward, R. M., Attallah, M. M., & Moore, A. J. (2018). Fluid and particle dynamics in laser powder bed fusion. *Acta Materialia*, *142*, 107-120.

[42] Basu, S., & DebRoy, T. (1992). Liquid metal expulsion during laser irradiation. *Journal of applied physics*, *72*(8), 3317-3322.

[43] Rai, R., Elmer, J. W., Palmer, T. A., & DebRoy, T. (2007). Heat transfer and fluid flow during keyhole mode laser welding of tantalum, Ti–6Al–4V, 304L stainless steel and vanadium. *Journal of physics D: Applied physics*, *40*(18), 5753.

[44] Kawahito, Y., Matsumoto, N., Abe, Y., & Katayama, S. (2011). Relationship of laser absorption to keyhole behavior in high power fiber laser welding of stainless steel and aluminum alloy. *Journal of Materials Processing Technology*, *211*(10), 1563-1568.

[45] He, X., Norris, J. T., Fuerschbach, P. W., & DebRoy, T. (2006). Liquid metal

expulsion during laser spot welding of 304 stainless steel. *Journal of Physics D: Applied Physics*, *39*(3), 525.

[46] Ly, S., Rubenchik, A. M., Khairallah, S. A., Guss, G., & Matthews, M. J. (2017). Metal vapor micro-jet controls material redistribution in laser powder bed fusion additive manufacturing. *Scientific reports*, *7*(1), 1-12.

[47] Wang, D., Wu, S., Fu, F., Mai, S., Yang, Y., Liu, Y., & Song, C. (2017). Mechanisms and characteristics of spatter generation in SLM processing and its effect on the properties. *Materials & Design*, *117*, 121-130.

[48] Simonelli, M., Tuck, C., Aboulkhair, N. T., Maskery, I., Ashcroft, I., Wildman, R. D., & Hague, R. (2015). A study on the laser spatter and the oxidation reactions during selective laser melting of 316L stainless steel, Al-Si10-Mg, and Ti-6Al-4V. *Metallurgical and Materials Transactions A*, *46*(9), 3842-3851.

[49] Leung, C. L. A., Marussi, S., Atwood, R. C., Towrie, M., Withers, P. J., & Lee, P. D. (2018). In situ X-ray imaging of defect and molten pool dynamics in laser additive manufacturing. *Nature communications*, *9*(1), 1-9.

[50] Guo, Q., Zhao, C., Escano, L. I., Young, Z., Xiong, L., Fezzaa, K., ... & Chen, L. (2018). Transient dynamics of powder spattering in laser powder bed fusion additive manufacturing process revealed by in-situ high-speed high-energy x-ray imaging. *Acta Materialia*, *151*, 169-180.

[51] Liu, Q. C., Elambasseril, J., Sun, S. J., Leary, M., Brandt, M., & Sharp, P. K. (2014). The effect of manufacturing defects on the fatigue behaviour of Ti-6Al-4V specimens fabricated using selective laser melting. In *Advanced Materials Research* (Vol. 891, pp. 1519-1524). Trans Tech Publications Ltd.

[52] Vilaro, T., Colin, C., & Bartout, J. D. (2011). As-fabricated and heat-treated microstructures of the Ti-6Al-4V alloy processed by selective laser melting. *Metallurgical and materials transactions A*, *42*(10), 3190-3199.

[53] Qiu, C., Panwisawas, C., Ward, M., Basoalto, H. C., Brooks, J. W., & Attallah, M. M. (2015). On the role of melt flow into the surface structure and porosity development during selective laser melting. *Acta Materialia*, *96*, 72-79.

[54] Zhou, X., Wang, D., Liu, X., Zhang, D., Qu, S., Ma, J., ... & Liu, W. (2015).

3D-imaging of selective laser melting defects in a Co–Cr–Mo alloy by synchrotron radiation micro-CT. *Acta Materialia*, *98*, 1-16.

[55] Kempen, K., Thijs, L., Van Humbeeck, J., & Kruth, J. P. (2015). Processing AlSi10Mg by selective laser melting: parameter optimisation and material characterisation. *Materials Science and Technology*, *31*(8), 917-923.

[56] Read, N., Wang, W., Essa, K., & Attallah, M. M. (2015). Selective laser melting of AlSi10Mg alloy: Process optimisation and mechanical properties development. *Materials & Design (1980-2015)*, *65*, 417-424.

[57] Cunningham, R., Zhao, C., Parab, N., Kantzos, C., Pauza, J., Fezzaa, K., ... & Rollett, A. D. (2019). Keyhole threshold and morphology in laser melting revealed by ultrahigh-speed x-ray imaging. *Science*, *363*(6429), 849-852.

[58] Zhao, H., & DebRoy, T. (2003). Macroporosity free aluminum alloy weldments through numerical simulation of keyhole mode laser welding. *Journal of Applied Physics*, *93*(12), 10089-10096.

[59] Blecher, J. J., Palmer, T. A., & Debroy, T. (2016). Porosity in thick section alloy 690 welds–experiments, modeling, mechanism, and remedy. *Weld. J*, *95*(1), 17s-26s.

[60] Zhao, C., Parab, N. D., Li, X., Fezzaa, K., Tan, W., Rollett, A. D., & Sun, T. (2020). Critical instability at moving keyhole tip generates porosity in laser melting. *Science*, *370*(6520), 1080-1086.

[61] Cunningham, R., Narra, S. P., Ozturk, T., Beuth, J., & Rollett, A. D. (2016). Evaluating the effect of processing parameters on porosity in electron beam melted Ti-6Al-4V via synchrotron X-ray microtomography. *Jom*, *68*(3), 765-771.

[62] Attallah, M. M., Jennings, R., Wang, X., & Carter, L. N. (2016). Additive manufacturing of Ni-based superalloys: The outstanding issues. *MRS bulletin*, *41*(10), 758-764.

[63] Kasperovich, G., Haubrich, J., Gussone, J., & Requena, G. (2016). Correlation between porosity and processing parameters in TiAl6V4 produced by selective laser melting. *Materials & Design*, *105*, 160-170.

[64] Tammas-Williams, S., Zhao, H., Léonard, F., Derguti, F., Todd, I., & Prangnell, P. B. (2015). XCT analysis of the influence of melt strategies on defect population in Ti–6Al–4V components manufactured by Selective Electron Beam Melting. *Materials Characterization*, *102*, 47-61.

[65] Carlson, K. D., Lin, Z., & Beckermann, C. (2007). Modeling the effect of finite-rate hydrogen diffusion on porosity formation in aluminum alloys. *Metallurgical and Materials Transactions B*, *38*(4), 541-555.

[66] Rappaz, M. (2016). Modeling and characterization of grain structures and defects in solidification. *Current Opinion in Solid State and Materials Science*, *20*(1), 37-45.

[67] Martin, J. H., Yahata, B. D., Hundley, J. M., Mayer, J. A., Schaedler, T. A., & Pollock, T. M. (2017). 3D printing of high-strength aluminium alloys. *Nature*, *549*(7672), 365-369.

[68] Carter, L. N., Martin, C., Withers, P. J., & Attallah, M. M. (2014). The influence of the laser scan strategy on grain structure and cracking behaviour in SLM powder-bed fabricated nickel superalloy. *Journal of Alloys and Compounds*, *615*, 338-347.

[69] Kumar, S., & Bhaduri, S. C. (1995). Theoretical investigation of penetration characteristics in gas metal-arc welding using finite element method. *Metallurgical and Materials Transactions B*, *26*(3), 611-624.

[70] Uddin, S. Z., Murr, L. E., Terrazas, C. A., Morton, P., Roberson, D. A., & Wicker, R. B. (2018). Processing and characterization of crack-free aluminum 6061 using high-temperature heating in laser powder bed fusion additive manufacturing. *Additive Manufacturing*, *22*, 405-415.

[71] Gu, D., Hagedorn, Y. C., Meiners, W., Meng, G., Batista, R. J. S., Wissenbach, K., & Poprawe, R. (2012). Densification behavior, microstructure evolution, and wear performance of selective laser melting processed commercially pure titanium. *Acta Materialia*, *60*(9), 3849-3860.

[72] Garibaldi, M., Ashcroft, I., Simonelli, M., & Hague, R. (2016). Metallurgy of high-silicon steel parts produced using Selective Laser Melting. *Acta*

Materialia, *110*, 207-216.

[73] Kou, S. (2003). Welding metallurgy. *New Jersey, USA*, *431*(446), 223-225.

[74] Chen, Y., Lu, F., Zhang, K., Nie, P., Hosseini, S. R. E., Feng, K., & Li, Z. (2016). Dendritic microstructure and hot cracking of laser additive manufactured Inconel 718 under improved base cooling. *Journal of Alloys and Compounds*, *670*, 312-321.

[75] Ghasemi-Tabasi, H., de Formanoir, C., Van Petegem, S., Jhabvala, J., Hocine, S., Boillat, E., ... & Logé, R. E. (2022). Direct observation of crack formation mechanisms with operando Laser Powder Bed Fusion X-ray imaging. *Additive Manufacturing*, 102619.

[76] Chen, Y., Zhang, K., Huang, J., Hosseini, S. R. E., & Li, Z. (2016). Characterization of heat affected zone liquation cracking in laser additive manufacturing of Inconel 718. *Materials & Design*, *90*, 586-594.

[77] Ramirez, A. J., & Lippold, J. C. (2004). High temperature behavior of Ni-base weld metal: Part I. Ductility and microstructural characterization. *Materials Science and Engineering: A*, *380*(1-2), 259-271.

[78] Noecker, F. F., & DuPont, J. N. (2009). Metallurgical investigation into ductility dip cracking in Ni-based alloys: Part II. *Weld. J*, *88*(3), 62s-77s.

[79] Young, G. A., Capobianco, T. E., Penik, M. A., Morris, B. W., & McGee, J. J. (2008). The mechanism of ductility dip cracking in nickel-chromium alloys. *WELDING JOURNAL-NEW YORK-*, *87*(2), 31.

[80] Nissley, N. E., & Lippold, J. C. (2008). Ductility-dip cracking susceptibility of nickel-based weld metals part 1: strain-to-fracture testing. *Welding journal*, *87*(10), 257s-264s.

[81] Xia, M., Gu, D., Yu, G., Dai, D., Chen, H., & Shi, Q. (2017). Porosity evolution and its thermodynamic mechanism of randomly packed powder-bed during selective laser melting of Inconel 718 alloy. *International Journal of Machine Tools and Manufacture*, *116*, 96-106.

[82] Yan, W., Ge, W., Qian, Y., Lin, S., Zhou, B., Liu, W. K., ... & Wagner, G. J. (2017). Multi-physics modeling of single/multiple-track defect mechanisms in

electron beam selective melting. *Acta Materialia*, *134*, 324-333.

[83] Khairallah, S. A., Anderson, A. T., Rubenchik, A., & King, W. E. (2016). Laser powder-bed fusion additive manufacturing: Physics of complex melt flow and formation mechanisms of pores, spatter, and denudation zones. *Acta Materialia*, *108*, 36-45.

[84] Shrestha, S., & Chou, K. (2017). A build surface study of Powder-Bed Electron Beam Additive Manufacturing by 3D thermo-fluid simulation and white-light interferometry. *International Journal of Machine Tools and Manufacture*, *121*, 37-49.

[85] Boschetto, A., Bottini, L., & Veniali, F. (2017). Roughness modeling of AlSi10Mg parts fabricated by selective laser melting. *Journal of Materials Processing Technology*, *241*, 154-163.

[86] DebRoy, T., Wei, H. L., Zuback, J. S., Mukherjee, T., Elmer, J. W., Milewski, J. O., ... & Zhang, W. (2018). Additive manufacturing of metallic components–process, structure and properties. *Progress in Materials Science*, *92*, 112-224.

[87] Gunenthiram, V., Peyre, P., Schneider, M., Dal, M., Coste, F., & Fabbro, R. (2017). Analysis of laser–melt pool–powder bed interaction during the selective laser melting of a stainless steel. *Journal of Laser Applications*, *29*(2), 022303.

[88] Thijs, L., Verhaeghe, F., Craeghs, T., Van Humbeeck, J., & Kruth, J. P. (2010). A study of the microstructural evolution during selective laser melting of Ti–6Al–4V. *Acta materialia*, *58*(9), 3303-3312.

[89] Carter, L. N., Wang, X., Read, N., Khan, R., Aristizabal, M., Essa, K., & Attallah, M. M. (2016). Process optimization of selective laser melting using energy density model for nickel based superalloys. *Materials Science and Technology*, *32*(7), 657-661.

[90] Yadroitsev, I., Bertrand, P., & Smurov, I. (2007). Parametric analysis of the selective laser melting process. *Applied surface science*, *253*(19), 8064-8069.

[91] Xu, W., Brandt, M., Sun, S., Elambasseril, J., Liu, Q., Latham, K., ... & Qian, M. (2015). Additive manufacturing of strong and ductile Ti–6Al–4V by selective laser melting via in situ martensite decomposition. *Acta Materialia*, *85*,

74-84.

[92] Wei, H. L., Cao, Y., Liao, W. H., & Liu, T. T. (2020). Mechanisms on inter-track void formation and phase transformation during laser powder bed fusion of Ti-6Al-4V. *Additive Manufacturing*, *34*, 101221.

[93] Mukherjee, T., Wei, H. L., De, A., & DebRoy, T. (2018). Heat and fluid flow in additive manufacturing–Part II: Powder bed fusion of stainless steel, and titanium, nickel and aluminum base alloys. *Computational Materials Science*, *150*, 369-380.

[94] Martin, A. A., Calta, N. P., Khairallah, S. A., Wang, J., Depond, P. J., Fong, A. Y., ... & Matthews, M. J. (2019). Dynamics of pore formation during laser powder bed fusion additive manufacturing. *Nature communications*, *10*(1), 1-10.

[95] Ren, G., Zhao, Z., Li, J., Hou, Y., Li, H., Dong, Z., & Zhang, L. (2025). Influence of Laser Energy Input on the Microstructure and Properties of 8620 Low-Alloy Steel Fabricated by Laser Powder Bed Fusion. *Journal of Materials Engineering and Performance*, 1-14.

[96] Thijs, L., Kempen, K., Kruth, J. P., & Van Humbeeck, J. (2013). Fine-structured aluminium products with controllable texture by selective laser melting of pre-alloyed AlSi10Mg powder. *Acta Materialia*, *61*(5), 1809-1819.

[97] Kempen, K., Thijs, L., Van Humbeeck, J., & Kruth, J. P. (2012). Mechanical properties of AlSi10Mg produced by selective laser melting. *Physics Procedia*, *39*, 439-446.

[98] Maskery, I., Aboulkhair, N. T., Corfield, M. R., Tuck, C., Clare, A. T., Leach, R. K., ... & Hague, R. J. (2016). Quantification and characterisation of porosity in selectively laser melted Al–Si10–Mg using X-ray computed tomography. *Materials Characterization*, *111*, 193-204.

[99] Bauereiß, A., Scharowsky, T., & Körner, C. (2014). Defect generation and propagation mechanism during additive manufacturing by selective beam melting. *Journal of Materials Processing Technology*, *214*(11), 2522-2528.

[100] Huang, W. D. Y. Y. Q., & Wei-hui, Y. L. W. (2010). Density improvement

of metal parts directly fabricated via selective laser melting. *Journal of South China University of Technology (Natural Science Edition)*.

[101] Yang, Y. Q., Song, C. H., & Wang, D. (2014). Selective laser melting and its application on personalized medical parts. *Journal of Mechanical Engineering*, *21*, 140-151.

[102] Wu, J., Li, L., Dai, L., Zhang, W., Huang, L., Meng, X., ... & Zhou, J. (2024). Influence of scanning strategies on microstructure and mechanical properties of laser powder bed fusion 2195 Al-Li alloy. *Journal of Alloys and Compounds*, *1004*, 175841.

[103] Chen, H., Gu, D., Dai, D., Ma, C., & Xia, M. (2017). Microstructure and composition homogeneity, tensile property, and underlying thermal physical mechanism of selective laser melting tool steel parts. *Materials Science and Engineering: A*, *682*, 279-289.

[104] Vastola, G., Zhang, G., Pei, Q. X., & Zhang, Y. W. (2016). Modeling the microstructure evolution during additive manufacturing of Ti6Al4V: A comparison between electron beam melting and selective laser melting. *Jom*, *68*(5), 1370-1375.

[105] Cook, P. S., & Murphy, A. B. (2020). Simulation of melt pool behaviour during additive manufacturing: Underlying physics and progress. *Additive Manufacturing*, *31*, 100909.

[106] Zhirnov, I., Yadroitsava, I., & Yadroitsev, I. (2015). Optical monitoring and numerical simulation of temperature distribution at selective laser melting of Ti6Al4V alloy. In *Materials Science Forum* (Vol. 828, pp. 474-481). Trans Tech Publications Ltd.

[107] Dunbar, A. J., Denlinger, E. R., Gouge, M. F., Simpson, T. W., & Michaleris, P. (2017). Comparisons of laser powder bed fusion additive manufacturing builds through experimental in situ distortion and temperature measurements. *Additive Manufacturing*, *15*, 57-65.

[108] Roberts, I. A., Wang, C. J., Esterlein, R., Stanford, M., & Mynors, D. J. (2009). A three-dimensional finite element analysis of the temperature field

during laser melting of metal powders in additive layer manufacturing. *International Journal of Machine Tools and Manufacture*, *49*(12-13), 916-923.

[109] Gusarov, A. V., Yadroitsev, I., Bertrand, P., & Smurov, I. (2007). Heat transfer modelling and stability analysis of selective laser melting. *Applied Surface Science*, *254*(4), 975-979.

[110] Gusarov, A. V., & Smurov, I. (2010). Modeling the interaction of laser radiation with powder bed at selective laser melting. *Physics Procedia*, *5*, 381-394.

[111] Gusarov, A. V., & Smurov, I. (2009). Two-dimensional numerical modelling of radiation transfer in powder beds at selective laser melting. *Applied Surface Science*, *255*(10), 5595-5599.

[112] Hooper, P. A. (2018). Melt pool temperature and cooling rates in laser powder bed fusion. *Additive Manufacturing*, *22*, 548-559.

[113] Dai, K., & Shaw, L. (2002). Distortion minimization of laser-processed components through control of laser scanning patterns. *Rapid Prototyping Journal*.

[114] Devesse, W., De Baere, D., Hinderdael, M., & Guillaume, P. (2016). Hardware-in-the-loop control of additive manufacturing processes using temperature feedback. *Journal of Laser Applications*, *28*(2), 022302.

[115] Craeghs, T., Clijsters, S., Yasa, E., Bechmann, F., Berumen, S., & Kruth, J. P. (2011). Determination of geometrical factors in Layerwise Laser Melting using optical process monitoring. *Optics and Lasers in Engineering*, *49*(12), 1440-1446.

[116] Miyagi, M., Tsukamoto, T., & Kawanaka, H. (2014). Adaptive shape control of laser-deposited metal structures by adjusting weld pool size. *Journal of Laser Applications*, *26*(3), 032003.

[117] Li, X., Li, H., Chen, X., Shen, S., Zhang, G., Wei, H., ... & Dai, L. (2025). In-situ multi-eye monitoring of melt pool temperature field in laser additive manufacturing by light field camera. *Additive Manufacturing*, *102*, 104747.

[118] Huang, Y., Fleming, T. G., Clark, S. J., Marussi, S., Fezzaa, K., Thiyagalingam, J., ... & Lee, P. D. (2022). Keyhole fluctuation and pore formation mechanisms during laser powder bed fusion additive manufacturing. *Nature communications*, *13*(1), 1-11.

[119] Wang, L., Zhang, Y., Chia, H. Y., & Yan, W. (2022). Mechanism of keyhole pore formation in metal additive manufacturing. *npj Computational Materials*, *8*(1), 1-11.

[120] Leung, C. L. A., Marussi, S., Towrie, M., Atwood, R. C., Withers, P. J., & Lee, P. D. (2019). The effect of powder oxidation on defect formation in laser additive manufacturing. *Acta Materialia*, *166*, 294-305.

[121] Hojjatzadeh, S. M. H., Parab, N. D., Yan, W., Guo, Q., Xiong, L., Zhao, C., ... & Chen, L. (2019). Pore elimination mechanisms during 3D printing of metals. *Nature communications*, *10*(1), 1-8.

[122] Fan, X., Fleming, T. G., Clark, S. J., Fezzaa, K., Getley, A. C., Marussi, S., ... & Lee, P. D. (2025). Magnetic modulation of keyhole instability during laser welding and additive manufacturing. *Science*, *387*(6736), 864-869.

[123] Chen, H., & Yan, W. (2020). Spattering and denudation in laser powder bed fusion process: Multiphase flow modelling. *Acta Materialia*, *196*, 154-167.

[124] Li, X., Guo, Q., Chen, L., & Tan, W. (2021). Quantitative investigation of gas flow, powder-gas interaction, and powder behavior under different ambient pressure levels in laser powder bed fusion. *International Journal of Machine Tools and Manufacture*, *170*, 103797.

[125] Yuan, W., Chen, H., Ruan, S., Lupoi, R., Qin, S., Guo, E., ... & Yin, S. (2025). Oscillatory nature in melt-gas-powder interactions during laser powder bed fusion process revealed by CFD-DEM coupled modelling. *Virtual and Physical Prototyping*, *20*(1), e2446619.

[126] Zhang, Y., Wu, S., Guo, Z., Peng, G., Wang, L., & Yan, W. (2025). Defects caused by powder spattering and entrainment in laser powder bed fusion process: High-fidelity modeling of gas, melt pool and powder dynamics. *Acta Materialia*, *288*, 120816.

[127] Guo, Q., Qu, M., Escano, L. I., Hojjatzadeh, S. M. H., Young, Z., Fezzaa, K., & Chen, L. (2022). Revealing melt flow instabilities in laser powder bed fusion additive manufacturing of aluminum alloy via in-situ high-speed X-ray imaging. *International Journal of Machine Tools and Manufacture*, *175*, 103861.

[128] Coniglio, N., & Cross, C. E. (2013). Initiation and growth mechanisms for weld solidification cracking. *International materials reviews*, *58*(7), 375-397.

[129] Fedina, T., Sundqvist, J., & Kaplan, A. F. (2021). Spattering and oxidation phenomena during recycling of low alloy steel powder in Laser Powder Bed Fusion. *Materials Today Communications*, *27*, 102241.

[130] Abu-warda, N., Bedmar, J., García-Rodriguez, S., Torres, B., Utrilla, M. V., & Rams, J. (2024). Effect of post-processing heat treatments on the high-temperature oxidation of additively manufactured 316L stainless steel. *Journal of Materials Research and Technology*, *29*, 3465-3476.

[131] Qiu, Y., Ren, P., Wen, C., Cheng, D., Wang, C., Lu, Y., ... & Zhou, S. (2024). High-temperature oxidation behavior of Cu-Fe-based immiscible alloy produced by laser powder bed fusion. *Corrosion Science*, *226*, 111637.

[132] Guo, C., Li, Y., Li, Y., Li, G., Lu, X., Li, Z., ... & Lu, J. (2024). High-temperature oxidation behaviour of a Co-based superalloy fabricated through laser powder bed fusion. *Corrosion Science*, *227*, 111703.

[133] Wang, L., Guo, Z., Peng, G., Wu, S., Zhang, Y., & Yan, W. (2024). Evaporation-Induced Composition Evolution in Metal Additive Manufacturing. *Advanced Functional Materials*, 2412071.

[134] Ren, P., Ouyang, Y., Mu, J., Luo, S., Tang, Z., Wu, Y., ... & Wang, H. (2025). Metal powder atomization preparation, modification, and reuse for additive manufacturing: A review. *Progress in Materials Science*, 101449.

[135] Shi, G., Zhang, R., Cao, Y., & Yang, G. (2024). A Review of the Vaporization Behavior of Some Metal Elements in the LPBF Process. *Micromachines*, *15*(7), 846.

[136] Chen, H., Wei, Q., Wen, S., Li, Z., & Shi, Y. (2017). Flow behavior of

powder particles in layering process of selective laser melting: Numerical modeling and experimental verification based on discrete element method. *International Journal of Machine Tools and Manufacture*, *123*, 146-159.

[137] Liu, Q., Zhou, Q., Gao, Y., Liu, Z., Chu, X., Zhang, Z., & Chen, Y. (2025). Investigation into particle flow patterns during powder spreading in SLM process. *Powder Technology*, *449*, 120429.

[138] Liu, M., Yang, X., Liu, Z., & Li, B. (2025). Effect of spreader and particle properties on powder bed generation with discrete element method in additive manufacturing. *Powder Technology*, *449*, 120420.

[139] Cundall, P. A., & Strack, O. D. (1979). A discrete numerical model for granular assemblies. *geotechnique*, *29*(1), 47-65.

[140] Parteli, E. J., & Pöschel, T. (2016). Particle-based simulation of powder application in additive manufacturing. *Powder Technology*, *288*, 96-102.

[141] Lee, Y. S., & Zhang, W. (2016). Modeling of heat transfer, fluid flow and solidification microstructure of nickel-base superalloy fabricated by laser powder bed fusion. *Additive Manufacturing*, *12*, 178-188.

[142] Wang, S., & Shen, Y. (2025). A new model framework of laser powder bed fusion by integrating a powder-scale model with a thermodynamic database. *Chemical Engineering Science*, *302*, 120788.

[143] Ma, H., Zhou, L., Liu, Z., Chen, M., Xia, X., & Zhao, Y. (2022). A review of recent development for the CFD-DEM investigations of non-spherical particles. *Powder Technology*, *412*, 117972.

[144] Weissbach, R., Praegla, P. M., Wall, W. A., Hart, A. J., & Meier, C. (2024). Exploration of improved, roller-based spreading strategies for cohesive powders in additive manufacturing via coupled DEM-FEM simulations. *Powder Technology*, *443*, 119956.

[145] Kumar, S., & Das, P. (2024). Multiphysics Modelling of Laser Powder Bed Fusion Based Additive Manufacturing of Single-Track Build of Ti6Al4V Alloy. *Transactions of the Indian Institute of Metals*, *77*(10), 2985-2994.

[146] Cao, S., Qiu, Y., Wei, X. F., & Zhang, H. H. (2015). Experimental and theoretical investigation on ultra-thin powder layering in three dimensional printing (3DP) by a novel double-smoothing mechanism. *Journal of materials processing technology*, *220*, 231-242.

[147] Marchelli, G., Prabhakar, R., Storti, D., & Ganter, M. (2011). The guide to glass 3D printing: developments, methods, diagnostics and results. *Rapid Prototyping Journal*, *17*(3), 187-194.

[148] Langston, P. A., Al-Awamleh, M. A., Fraige, F. Y., & Asmar, B. N. (2004). Distinct element modelling of non-spherical frictionless particle flow. *Chemical Engineering Science*, *59*(2), 425-435.

[149] Zhang, L. C., Attar, H., Calin, M., & Eckert, J. (2016). Review on manufacture by selective laser melting and properties of titanium based materials for biomedical applications. *Materials Technology*, *31*(2), 66-76.

[150] Khairallah, S. A., & Anderson, A. (2014). Mesoscopic simulation model of selective laser melting of stainless steel powder. *Journal of Materials Processing Technology*, *214*(11), 2627-2636.

[151] Yang, R. Y., Zou, R. P., & Yu, A. B. (2000). Computer simulation of the packing of fine particles. *Physical review E*, *62*(3), 3900.

[152] Zhou, Y. C., Xu, B. H., Yu, A. B., & Zulli, P. (2002). An experimental and numerical study of the angle of repose of coarse spheres. *Powder technology*, *125*(1), 45-54.

[153] Yao, D., An, X., Fu, H., Zhang, H., Yang, X., Zou, Q., & Dong, K. (2021). Dynamic investigation on the powder spreading during selective laser melting additive manufacturing. *Additive Manufacturing*, *37*, 101707.

[154] Nan, W., Pasha, M., & Ghadiri, M. (2020). Numerical simulation of particle flow and segregation during roller spreading process in additive manufacturing. *Powder Technology*, *364*, 811-821.

[155] Cleary, P. W. (2015). A multiscale method for including fine particle effects in DEM models of grinding mills. *Minerals Engineering*, *84*, 88-99.

[156] Cao, L. (2019). Numerical simulation of the impact of laying powder on

selective laser melting single-pass formation. *International Journal of Heat and Mass Transfer*, *141*, 1036-1048.

[157] Gan, Z., Kafka, O. L., Parab, N., Zhao, C., Fang, L., Heinonen, O., ... & Liu, W. K. (2021). Universal scaling laws of keyhole stability and porosity in 3D printing of metals. *Nature communications*, *12*(1), 2379.

[158] O'Sullivan, C., & Bray, J. D. (2004). Selecting a suitable time step for discrete element simulations that use the central difference time integration scheme. *Engineering Computations*, *21*(2/3/4), 278-303.

[159] Qiu, Y., Yang, T., Zhu, H., Han, W., Sugioka, K., & Kong, L. (2025). Dynamic behavior and defect control in LPBF of quartz glass: Insights from VOF model simulations. *Powder Technology*, *451*, 120450.

[160] Yao, D., Liu, X., Wang, J., Fan, W., Li, M., Fu, H., ... & An, X. (2021). Numerical insights on the spreading of practical 316 L stainless steel powder in SLM additive manufacturing. *Powder Technology*, *390*, 197-208.

[161] Cox, B., Ghayoor, M., Doyle, R. P., Pasebani, S., & Gess, J. (2022). Numerical model of heat transfer during laser powder bed fusion of 316L stainless steel. *The International Journal of Advanced Manufacturing Technology*, 1-11.

[162] Xiang, Z., Yin, M., Dong, G., Mei, X., & Yin, G. (2018). Modeling of the thermal physical process and study on the reliability of linear energy density for selective laser melting. *Results in Physics*, *9*, 939-946.

[163] Aggarwal, A., Shin, Y. C., & Kumar, A. (2023). Investigation of the transient coupling between the dynamic laser beam absorptance and the melt pool-vapor depression morphology in laser powder bed fusion process. *International Journal of Heat and Mass Transfer*, *201*, 123663.

[164] Dey, S., & Ali, S. Z. (2018). Advances in modeling of bed particle entrainment sheared by turbulent flow. *Physics of Fluids*, *30*(6).

[165] Tang, C., Le, K. Q., & Wong, C. H. (2020). Physics of humping formation in laser powder bed fusion. *International Journal of Heat and Mass Transfer*, *149*, 119172.

[166] Li, L., Li, J. Q., & Fan, T. H. (2021). Phase-field modeling of wetting and balling dynamics in powder bed fusion process. *Physics of Fluids*, *33*(4).

[167] Chen, Q., Zhao, Y., Strayer, S., Zhao, Y., Aoyagi, K., Koizumi, Y., ... & To, A. C. (2021). Elucidating the effect of preheating temperature on melt pool morphology variation in Inconel 718 laser powder bed fusion via simulation and experiment. *Additive Manufacturing*, *37*, 101642.

[168] Peng, J., Liu, J., Yang, X., Ge, J., Han, P., Wang, X., ... & Wang, Y. (2022). Numerical simulation of preheating temperature on molten pool dynamics in laser deep-penetration welding. *Coatings*, *12*(9), 1280.

[169] Hamaker, H. C. (1937). The London-van der Waals attraction between spherical particles. *Physica*, *4*(10), 1058-1072.

[170] Israelachvili, J. N. (2011). Intermolecular and Surface Forces (3rd ed.). Academic Press.

[171] Visser, J. (1989). Van der Waals and other cohesive forces affecting powder fluidization. *Powder Technology*, *58*(1), 1-10.

[172] Guo, D., Lambert-Garcia, R., Hocine, S., Fan, X., Greenhalgh, H., Shahani, R., ... & Leung, C. L. A. (2024). Correlative spatter and vapour depression dynamics during laser powder bed fusion of an Al-Fe-Zr alloy. *International Journal of Extreme Manufacturing*, *6*(5), 055601.

[173] Bitharas, I., Parab, N., Zhao, C., Sun, T., Rollett, A. D., & Moore, A. J. (2022). The interplay between vapour, liquid, and solid phases in laser powder bed fusion. *Nature Communications*, *13*(1), 2959.

[174] Qu, M., Guo, Q., Escano, L. I., Nabaa, A., Hojjatzadeh, S. M. H., Young, Z. A., & Chen, L. (2022). Controlling process instability for defect lean metal additive manufacturing. *Nature communications*, *13*(1), 1-8.

[175] Philo, A. M., Sutcliffe, C. J., Sillars, S., Sienz, J., Brown, S. G. R., & Lavery, N. P. (2017). A Study into the Effects of Gas Flow Inlet Design of the Renishaw AM250 Laser Powder Bed Fusion Machine Using Computational Modeling. In *2017 International Solid Freeform Fabrication Symposium*. University of Texas at Austin.

[176] Zhang, X., Cheng, B., & Tuffile, C. (2020). Simulation study of the spatter removal process and optimization design of gas flow system in laser powder bed fusion. *Additive Manufacturing*, *32*, 101049.